UNIVERSITY OF SOUTHAMPTON

FACULTY OF ENGINEERING, SCIENCE AND MATHEMATICS

School of Chemistry

Solid-State Nuclear Magnetic Resonance of Rhodopsin and its Photointermediates

by

Maria Concistré

Thesis for the degree of Doctor of Philosophy

JANUARY 2010

Ai miei carissimi genitori,
a Brigida, a Giovanni...

...a Peppe

ABSTRACT

Photoisomerization of the membrane-bound light receptor protein rhodopsin leads to a highly energetic species called bathorhodopsin, which is stable at temperatures below 125 K. Bathorhodopsin stores about 2/3 of the absorbed photon energy but the mechanisms with which this energy is stored is not completely understood. A new insight into these mechanisms by means of low-temperature solid-state NMR is both subject and aim of this Ph.D. thesis. The issue of the energy storage has been investigated by a solid state magic angle spinning technique which combines modern symmetry-based recoupling techniques with in situ cooling of the sample. Production of bathorhodopsin is also done in situ in a customized NMR probe. Three kind of experiments are discussed: chemical shift, distance and torsional angle measurements. The first kind of experiments led to carbon chemical shifts values for almost all the carbons along the retinylidene chain of the retinal chromophore of bathorhodopsin. Our measurements show a significant perturbations of the ^{13}C chemical shifts in bathorhodopsin which is interpreted in terms of charge delocalization along the chain and therefore indicates a participation of an electrostatic mechanism to the energy storage. This is at variance with an earlier solid state NMR study where only minor perturbations of the electronic structure in the isomerized retinylidene chain were observed. We believe that these data incorrectly refer to bathorhodopsin because of the incorrect conditions of temperature and illumination applied. To sample for other local mechanisms that may contribute to the energy storage, the C-C distance of the last two carbons of the retinylidene chain, at the link with the protein opsin, was also measured but no significant differences with rhodopsin have been found. Finally, the H-C=C-H torsional angle at the double bound where the isomerization takes place was measured in a double-quantum heteronuclear local field spectroscopy (2Q-HLF) experiment. Results indicate a deviation from planarity of at least 40° about this double bond in bathorhodopsin suggesting an unquantified amount of torsional strain acting as a further energy storage mechanism. In addition to these very interesting results, this thesis reports methods, equipment and procedures ready to be used for the study of other similar light-triggered processes.

CONTENTS

LIST OF FIGURES

LIST OF TABLES

DECLARATION OF AUTHORSHIP

This thesis is the result of work done wholly while I was in registered candidature for a Ph.D. degree at this University. The material presented herein is based on work mostly done by myself. Where the work was carried out jointly with others, a substantial part is my own original work and co-workers and their roles have been, clearly, indicated. The material contained herein has not been submitted by the author for a degree at any other institution.

Date: 29 February 2010

Signed:

LIST OF PAPERS

The following thesis discusses the work published in the following papers:

1. “**Analytical theory of gamma-encoded double-quantum recoupling sequences in solid-state nuclear magnetic resonance**”,

   Pileio G., Concistré M., McLean N., Gansmüller A., Brown R. C. D., Levitt M. H., *J. Magn. Phys.*, **186**, (2007), 65.

2. “**Double quantum ^{13}C nuclear magnetic resonance of bathorhodopsin, the first photointermediate in mammalian vision**”,

   Concistré M., Gansmüller A., McLean N., Johannessen O. G., Marín-Montesinos I., Bovee-Geurts P. H., Verdegem P., Lugtenburg J., Brown R. C. D., DeGrip W. J., Levitt M. H., *J. Am. Chem. Soc.*, **130**, (2008), 10490.

3. “**Supercycled homonuclear dipolar decoupling sequences in solid-state NMR**”,

   Paul S., Thakur R. S., Goswami M., Sauerwein A. C., Mamone S., Concistré M., Förster H., Levitt M. H., Madhu P. K., *J. Magn. Reson.*, **197**, (2009), 14.

4. “**Towards an interpretation of ^{13}C chemical shifts in bathorhodopsin, a functional intermediate of a G-protein coupled receptor**”,

   Gansmüller A., Concistré M., McLean N., Johannessen O. G., Marín-Montesinos I., Bovee-Geurts P. H., Verdegem P., Lugtenburg J., Brown R. C., Degrip W. J., Levitt M. H., *Biochim. Biophys. Acta*, **1788**, (2009), 1350.

5. “**Light penetration and photoisomerization in rhodopsin studied by numerical simulations and double-quantum solid-state NMR spectroscopy**”,

Concistré M., Gansmüller A., McLean N., Johannessen O. G., Marín-Montesinos I., Bovee-Geurts P. H., Brown R. C. D., DeGrip W. J., Levitt M. H., *J. Am. Chem. Soc.*, **131**, (2009), 6133.

ACKNOWLEDGEMENTS

At the end of this “journey” it is a pleasure to thank the people who made this thesis possible and the people who made this time a pleasant time.

First and foremost I would like to thank my supervisor Malcolm Levitt for the encouragement, trust and supervision and for being a continuous source of scientific curiosity. Throughout my PhD period he provided me sound advices, good teachings, lots of good ideas and patient support always with his friendly attitude. A shining example of a supervisor!

I have had a great deal of support from people in Malcolm’s group with who I have enjoyed working. We had a really good time together! Thanks to the old and the newer members of the group: Axel, Ole, Marina, Ilde, Giancarlo, Salvo, Andrea, Sergey, Michael, Pierre and Giulia. Thanks to all of you for the warm and supportive atmosphere during the working hours. A special thought goes to Salvo for being such a dear friend.

I am very grateful to Axel for his help, for our useful discussion and for being a guide in this project at the beginning of my PhD. Thanks for sharing the day-to-day and night-to-night running of rhodopsin experiments.

For the important role in this project, I wish to thank Ole for his technical support during the experiments and for the building and the set up of the experimental equipment.

Thanks to Ole and Marina for their friendship, their kindness and for the nice evenings spent together.

The experimental work here described would not have been possible without the synthesis and preparation of samples by our collaborators. Thanks to Neville McLean and Dr. Richard C. D. Brown for the synthesis of the labelled retinals and thanks to Willem J. DeGrip and Petra H. M. Bovee-Geurts for the incorporation of the chromophore into the protein.

A thought to all the friends were sharing with me this new and very nice experience. All of you will hold a piece of my memory.

Grazie ai miei genitori, a Brigida e a Giovanni per il loro continuo e incondizionato aiuto, tacito o esplicito, per il loro incrollabile supporto in ogni mia scelta e per la loro costante presenza in ogni momento della mia vita. A loro dedico questa mia tesi e quanto di piu' bello e importante saro' in grado di realizzare nella mia vita.

Penso...anzi...sono sicura che quest'esperienza non sarebbe stata la stessa senza la presenza di una persona con cui ho diviso e condiviso fin dal primo giorno ogni difficolta', ogni stato d'animo, ogni dubbio, ogni delusione, ogni soddisfazione, ogni piccolo successo. Grazie Rosa che con il tuo affetto, con i tuoi slanci di ottimismo e il tuo modo di essere mi hai fatto un grande dono: la consapevolezza di non essere sola in quest'avventura e in quelle che verranno.

Se ripenso a questi anni trascorsi, sento di dover rivolgere il mio pensiero ad altre due persone, Giulia e Daniela. Con loro ho condivo periodi diversi e brevi di questa mia esperienza ma entrambi intesi e soprattutto ricchi di sentimenti belli, veri e sinceri.

E infine, grazie a te Peppe! Sei in ogni pagina di questa tesi...con il tuo aiuto (sia morale che materiale), con il tuo sostegno e con quella tenacia che sei riuscito a trasmettermi. Mi hai dato la spinta per credere in me stessa!

07/06/2010

A conclusione definitiva di questo capitolo sento di dovere ringraziare due persone: Gerardo e Marina.

Gerardo ha vissuto con me i giorni di preparazione al viva rendendoli, con le sue parole, con la sua presenza e con le nostre risate, piacevoli e meno pesanti.

Grazie ancora a te Marina. I tuo consigli e i tuoi siggerimenti sono stati apprezzati e fondamentali, come fontamentale e' stata la tua presenza durante il viva anche e soprattutto da un punto di vista emotivo.

PART I: INTRODUCTION

OVERVIEW

Dim-light vision in vertebrates is initiated when a photon is absorbed by the retinylidene prosthetic group of the transmembrane protein rhodopsin, a G-protein coupled receptor (GPCR) molecule which is abundant in the rod cells of the retina. Light sensitivity is provided by the 11-*cis* retinylidene chromophore covalently bounded to the opsin protein. The photon absorption lead to an ultrafast (200 fs) and highly selective isomerization of the retinylidene chromophore from the 11-*cis* configuration to a distorted all-*trans* configuration. The resultant photostate is called bathorhodopsin and stores instantly two-thirds of the absorbed photon energy. Under physiological conditions, bathorhodopsin is converted rapidly in a series of spectrally distinct photointermediates to reach the unprotonated metarhodopsin II conformation and activate the signalling process leading to vision. For several reasons, rhodopsin has been studied a lot by means of many different techniques and almost all we know about G-proteins comes from studied carried out on rhodopsin. Despite these studies, rhodopsin remains a very interesting case since many of its features are still not well understood. It is the case, for example, of the ultrafast isomerization (one of the fastest known in nature) or the mechanism in which the photon energy is stored in the different photointermediates.

This thesis reports a study on bathorhodopsin carried out by means of low-temperature solid-state NMR. Its main aim is to address the question how the photon energy is stored in this photointermediate. As an outcome of. perhaps, more general interest, this thesis discusses equipments, experimental set up, techniques and procedures to allow the study of any other light-triggered *reaction* by means of solid-state NMR. Whilst it is easy to understand how NMR and its recognized ability to *picture* dynamics and local information could add very important pieces of information and contribute to the disputes still on about rhodopsin, the challenges in doing so are, instead, not so easy to overcome. The lifetime of bathorhodopsin in physiological conditions is a few hundreds of femtoseconds and this is far to short time to allow any solid-state NMR investigation. However, the photointermediate can be trapped and stably maintained *in-vitro* at temperatures strictly below 125K. These temperatures and the stability required for such an investigation are not achievable using conventional low temperature solid-state magic angle spinning (SSMAS) probes available on the market. Therefore, a customized solution has to be made. On this point there is some more to care about. The spinning of the sample required by the SSMAS techniques, creates temperature gradients in the proximity of the sample itself due to the mixing of the cold nitrogen gas used to cool the sample and the warmer nitrogen gas used to spin the sample. This problem has been minimized in our customization of the equipment by redesigning the conventional NMR sample cooling system (VT stack) in order to allow pre-cooling of the spinning gas by thermal contact with the exhaust of the main stream used to cool the sample. The residual (and still important) thermal gradient was then accurately quantified and corrected as explained in the thesis.

Another challenge is constituted by the light-triggering of the rhodopsin sample needed to start the photocycle and produce the bathorhodopsin photointermediate. Firstly, in order to keep the sample stable at the correct temperature, it has to happen *in-situ*. This problem was sorted out in our customization of the NMR probe that uses optical fibers to shine light directly to the sample. On a more chemical basis, the complexity of the rhodopsin absorption spectrum and the very high molar extinction coefficient of rhodopsin and its photointermediates required an accurate study that, through experiments and simulations, suggested not only the best wavelength to be shined through or how long it needs to be turned on, but also the way the sample has to be prepared.

There are challenges also in the way to chose and/or design the NMR experiments. How to isolate the signal from the chromophore in the protein in its native membrane? Which is the best way to address the aim of this thesis, i.e. which kind of information can provide answers to the way bathorhodopsin stores energy? And which kind of experiments can be performed in order to acquire these information? Our strategy was to combine cross polarization magic angle spinning (CPMAS) and symmetry based recoupling sequences on a series of $^{13}C_2$-retinylidene-rhodopsin samples selectively doubly labeled along the different (and adjacent) carbon positions in the retinylidene chain. In this way, and through the use of double-quantum filtering, it was possible to isolate the signals of the two coupled carbons along the chain and acquire the chemical shift of those carbons. These provided insights into the energy storage mechanism since the chemical shift is very sensitive to the local environment and to charge delocalization in the chain. It was therefore possible to probe the existence and the importance of electrostatic interactions in the surrounding of the chromophore. To probe an eventual contribution of steric strain to the energy storage (another accredited mechanism) a solid state NMR experiment called double-quantum heteronuclear local field spectroscopy (2Q-HLF) was setup to allow the direct estimation of torsional angles in H-C-C-H molecular fragments. These experiments, performed on the retinylidene-rhodopsin sample labeled in the positions C11 and C12, i.e. at the double bond where the light-triggered isomerization takes place, has evidenced a quite relevant local distortion from planarity and therefore a non-yet-quantified amount of steric strain. Finally, carbon-carbon distance measurements have been done using a double quantum filtered dipolar recoupling technique. These experiments, here performed only on the retinylidene-rhodopsin sample labeled in the positions C14 and C15, at the end of the retinylidene chain, showed no significant distance differences between bathorhodopsin and rhodopsin. However, the meaning of this is not easily readable in terms of the energy storage issue and further measurements are needed.

The material presented in this overview will be discussed in the rest of this thesis according to the following scheme: **Introduction**, **Theory** and **Experiments**. **Introduction** mainly focuses on rhodopsin by describing its structure, role and photocycle. This part also resumes the relevant results on rhodopsin and its photointermediate achieved by means of NMR and other spectroscopic techniques. **Theory** describes the NMR hamiltonian and the magic angle spinning technique in Chapter 2 and the solid-state NMR techniques relevant to this work in Chapter 3. A detailed theoretical explanation of the pulse sequences used is also included. **Experiments** contains a detailed description of materials and procedures together with discussion and schematics of the customized equipment proposed and used in these studies (Chapter 4). The three types of experiments performed and their outcomes are discussed in Chapter 5 where these results will also be correlated and discussed to target the aim of this thesis. A conclusive chapter summarizes the main achievements of this work.

1. RHODOPSIN

Rhodopsin is the protein component of the light receptor in the retinal rods of the vertebrate eye and it is responsible for vision under dim light. Rhodopsin is a prototypal G-protein coupled receptors (GPCRs) for signal transduction. This means that the transmembrane protein is coupled to other proteins, called G proteins, and carry messages across the cell membrane. They provide a molecular link between extra- and intra-cellular processes. In the visual system, GPCRs such as rhodopsin and cone visual pigments absorb photons and initiate a signal transduction cascade that result in electrical signals finally processed by the brain [20, 21, 22]. GPCR are of central importance in pharmaceutical industrial processes as many of the drugs produced have GPCRs as target. This justifies the attention not only in spotting the structure of GPCRs but also in the investigations aimed to the comprehension of their active site and their mechanisms. Rhodopsin, thanks to its good stability in detergent solution, is the first GPCR for which structure has been solved [1, 23], therefore, much of what is known about GPCR structure comes from rhodopsin studies. The determination of the rhodopsin structure at atomic resolutions and the fact that GPRC are highly homologous [24, 25], opens the way to a deeper understanding of GPCR activation and transmembrane signaling. Significant progress in understanding the structure and function of rhodopsin has been made in recent years. Electron cryomicroscopy on two-dimensional crystals of bovine rhodopsin provided the first direct visualization of the seven transmembrane helices of a G-protein-coupled receptor (GPCR) [26, 27], and led to structural information about other members of the superfamily through homology-modeling studies [28]. Other biochemical and biophysical studies, provided valuable information on the nature of rhodopsin structure and the mechanism of rhodopsin activation. In addition, the structural determination of bovine rhodopsin by X-ray crystallography [1, 23] offers a new opportunity to assemble these related studies, providing further insight into the mechanism of activation of rhodopsin and GPCRs in general. This section will try to give a brief overview of the structure and the role of this protein. These information, far beyond my background of chemist, have been here reported for the sake of completeness. They do not constitute a research topics of this thesis and therefore have been extrapolated from various literature sources.

1.1 Overview of Rhodopsin Structure

Rhodopsin is found in the rod cells of the retina at the back of the vertebrate eye. An overview of rhodopsin structure together with its location in the rod cells is given in Fig. 1.1

The first X-ray crystallographic structure of rhodopsin (2.8 $\AA$ resolution) was obtained by Palczewsky *et al.* in 2000 [23]. This revealed the arrangement of helices, the interhelical connections, the chromophore binding site and interactions involved in the ligand binding. Further improvements in the rhodopsin crystals led to higher-resolution diffraction data that allow the identification of the protein fragments to a resolution of 2.6 $\AA$ [2] and the determination of the size and shape of the binding pocket. Seven water molecules were also evidenced as located close to the retinal chromophore. Despite no information are so available to elucidate the mechanism of activation, these X-ray studies have provided interesting data. Here some insights into its structure and functionality:

- *Structure*

  Rhodopsin is a 41 kDa membrane protein which consists of a single polypeptide "opsin" and a chromophore, 11-*cis*-retinal which is formed by oxidation of the vitamin A. The opsin contains 348 amino acids building up seven transmembrane α-helices as typical structural motif of the GPCRs [28]. A ribbon diagram is presented in Fig. 1.1a. The overall elliptic, cylindrical shape of the protein is due to the particular arrangement of its seven transmembrane helices, which are irregular in both length and orientation. The amino-terminal region is located intradiscally (extracellularly), and the C-terminal region is cytoplasmic (Fig. 1.1c). Rhodopsin's dimensions are $\sim$75 $\AA$ along the axis perpendicular to the membrane and $\sim$48 $\AA$ x $\sim$35 $\AA$ in the plane perpendicular to this axis. The surface area of the portions projecting out of the membrane is $\sim$1200 $\AA^2$, with the cytoplasmic projection larger in volume and surface area than the intradiscal face (Fig. 1.1d). The photoreactive chromophore, 11-*cis*-retinal, is covalently bound to Lys-296 by a protonated Schiff base

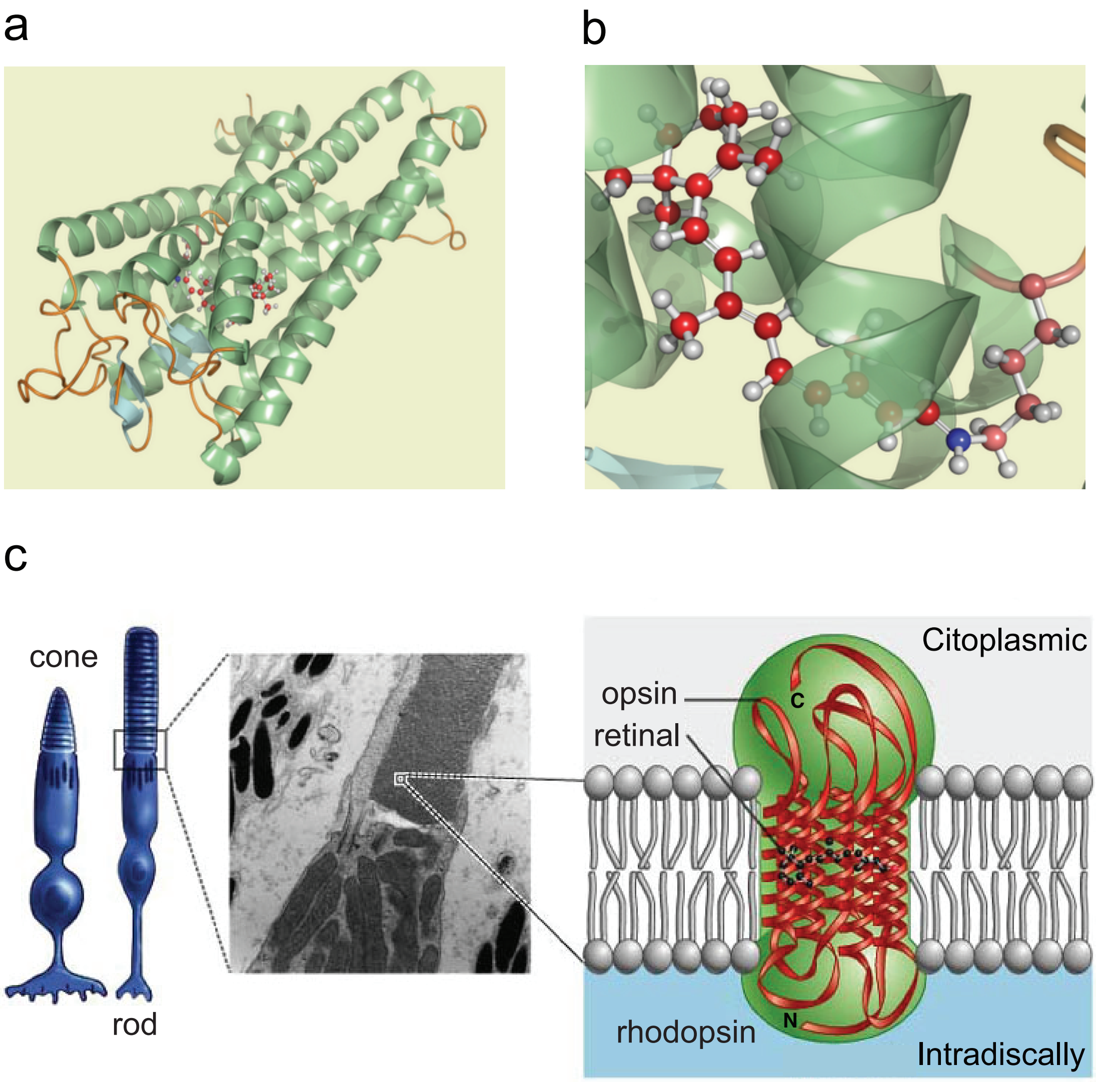

Fig. 1.1: a) the rhodopsin ribbon structure at the initial state of its photocycle; b) the chromophore structure at the same initial state; c) overview of rhodopsin and its location in the rod cell of the eye. Source: google (a, b); http://www.bio.miami.edu/∼cmallery/150/neuro/senses.htm (c).

(PSB) linkage. This appears to be stabilized by electrostatic interactions with a complex counterion mainly involving the negatively charged Glu113. Disruption of this salt bridge [29] upon proton transfer is thought to trigger conformational changes in rhodopsin [30] which are at the basis of the G protein activation mechanism. This may explain why the nature of the interaction between the Schiff base and the counterion in the ground state of rhodopsin has been the focus of many studies [31]. X-ray crystal structure, for example, has revealed that i) the side chain of Glu113 is located in the vicinity of the

Schiff base nitrogen (suggesting a direct contact between them) and ii) other (charged and/or polar) residues are also close and may effect the electrostatic interaction. Furthermore, according to some previous NMR and FT-IR studies [32, 33, 34, 35] water molecules may mediate the electrostatic interaction.

- *Retinal and its Environment*

  The major function for rhodopsin is to couple the conformational change of the chromophore (successive to the absorption of a photon) with the structural changes of the protein itself in order to generate a signal on the cytoplasmic side of the molecule. This explains the great interest in the retinal environment and its conformation inside the protein. A detailed description of the retinal environment has been published [22, 36]. The retinal lies embedded in the center of the protein, towards the extracellular side. It is completely buried inside the protein and there are no gaps between the helices so that the retinal cannot escape from the binding side. The 11-*cis* conformation was identified by X-Ray diffraction at 2.8 *Å* resolution [23]. The chromophore is not planar [37] about C6-C7 and C12-C13 bonds: the conjugated system is twisted possibly due to both electrostatic interactions with the protein, and steric strain inside the binding pocket. Images of the chromophore and its binding site are shown in Fig. 1.2 where the closest amino acids residues were highlighted.

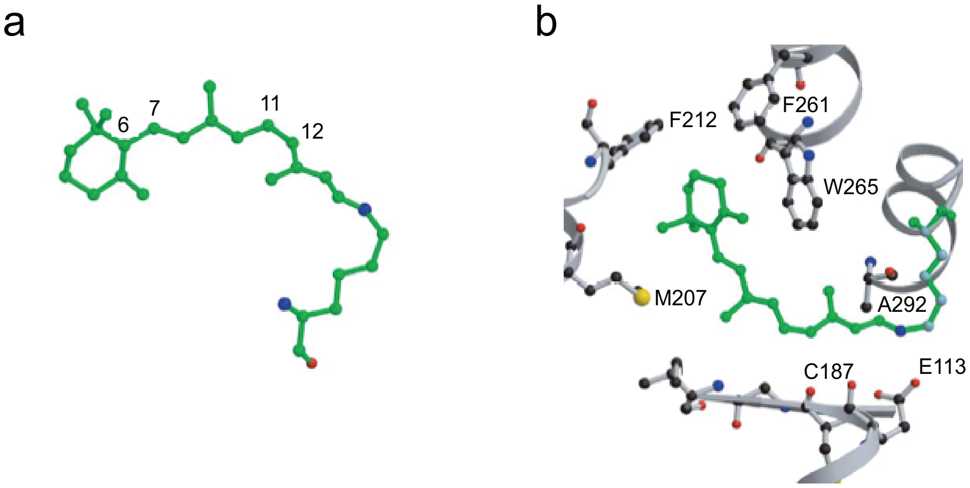

Fig. 1.2: Retinal chromophore and its environment in the crystal: a) 11-*cis*-retinal Schiff base linked to Lys296. Nitrogen and oxygen atoms are colored in blue and red respectively. b) chromophore-binding site with some nearby amino acid residue. Adapted from Ref. [1]

The C11-C12 is the double bound at which the isomerization occurs and it is found to be twisted already in the ground state. It is likely that the interaction between the methyl group attached to C13 and the W265 residue (Fig. 1.2b) contributes to the twist around C11-C12 causing the observed ultra fast photoisomerization and explaining its high quantum yield [38].

Another region of interest concerns the C6-C7 single bond, which defines the orientation of the β-ionone ring. In the electron density map calculated to 2.2 *Å* resolution [1], a 6*s-cis* form with substantial negative twist was found. All the dihedral angles and the bond lengths are given in Ref. [1] and compared with theoretical calculations. The orientation of the β-ionone ring is restricted by a set of hydrophobic residues (F212, F261 and W265) in the cytoplasmic side (Fig. 1.2b).

- *The Hydrogen Bonded Network at the Chromophore Binding Site*

  The higher resolution (2.6 *Å*) X-ray structure produced by Okada and colleagues [2] has showed the importance and the functional role of water molecules in the transmembrane region of rhodopsin. Seven water molecules were, in fact, observed (see Fig. 1.3) suggesting that amino acids residues in the proximity of the binding site are stabilized by water molecules.

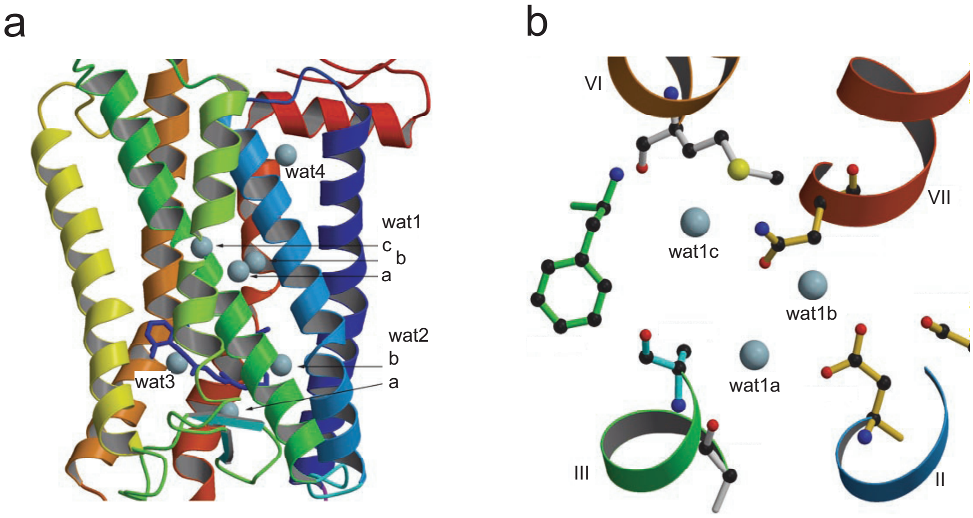

Fig. 1.3: (a) Global view of the transmembrane helical region of the refined rhodopsin structure showing the position of the seven water molecules. (b) Expanded view of the *wat1* site located in the proximity of the chromophore. Adapted from Ref. [2]

This has also been explored by theoretical calculation but deviation from the crystal structure were found (Fig. 1.4).

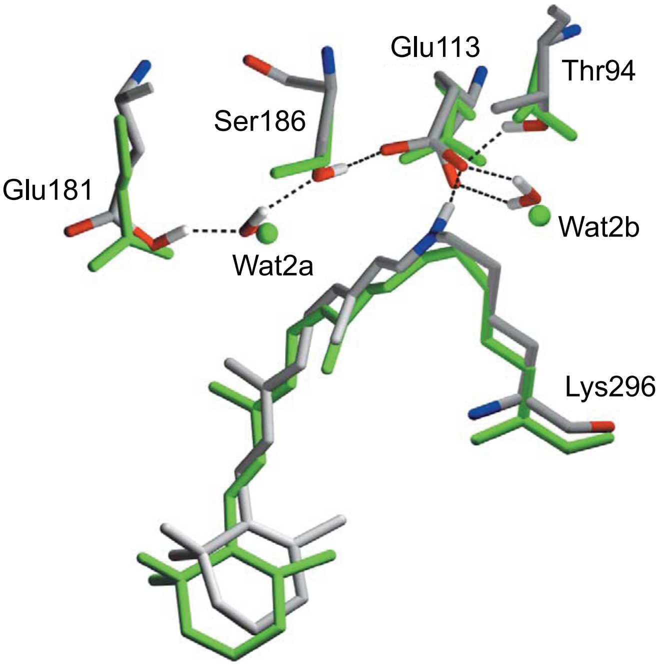

Fig. 1.4: The hydrogen bonded network from Thr94 to Glu181 as results from theoretical calculations and compared to the X-ray crystal structure (2.2 *Å* resolution, shown in green). Source: Ref. [1]

The hydrogen bonded network around the chromophore appears to be crucial for the stabilization of protonated Schiff base, the regulation of absorption wavelength and the activation upon photon absorption. The water molecule Wat2b near to Glu113, is suspected to be part of the complex counterion that stabilizes the protonated state of the chromophore. The Thr94 hydroxyl group binds to the Glu113 carboxylate oxygen atom, which is involved in the salt-bridge with the chromophore. This oxygen atom also coordinates with Wat2b, which forms a bridge to the Glu113 backbone. The second oxygen atom of the carboxylate is connected to the Ser186 hydroxyl group and the peptide backbone hydrogen atom of Cys187. Wat2a is involved in three hydrogen bonds to Ser186, to the backbone oxygen atom of Cys187, and to the OH group of Glu181. Out from Glu181 the network extends further to Tyr268 and Tyr192. In the dark state it stabilizes the charge distribution of the chromophore at the binding site. Calculations [39, 40] have shown that a major contributing factor for keeping the Schiff base nitrogen atom protonated is the involvement of Glu113 in hydrogen bonding, which reduces its basicity. The strongest of these bonds is the one to Thr94, but bonding to Wat2b stabilizes the negatively charge counterion even further.

1.2 *How does Rhodopsin Work?*

Ground-state rhodopsin is inactive, and several of its structural elements combine to retain this structure. Interactions among the extracellular loops limit the conformational flexibility of this part of the molecule under dark conditions. In addition, the interactions between the chromophore and the protein, both hydrophobic and electrostatic, tighten the inactive receptor structure. Mutation of Lys296 or Glu113 eliminating this interaction result in constitutively active receptors [41]. Three other parts of the rhodopsin structure are also important and concur to its inactive form. One of these is a tight set of interhelical contacts involving Asp83, Asn55 and Asn302 (Fig. 1.2). A further stabilization comes from the interaction between residues in helix III, at the center of the seven helices, and residues in each of the other helices (except helix I). Finally, Arg135 makes ionic interactions within the receptor.

What happens after absorption of a photon can be divided into three main steps: 1) isomerization of the chromophore by the absorption of photons; 2) conformational change and activation of the protein; and 3) production of a nervous impulse by a signal transduction cascade. These are here briefly described:

1. *Isomerization of the Chromophore*

   When the rhodopsin's chromophore absorbs a photon it isomerises to its all-*trans* configuration (see Fig. 1.5) without (at first) any accompanying change in the structure of the protein.

   In more details, when light is absorbed by rhodopsin, the 11,12-double bond electrons (note the high natural selectivity) of a π orbital in 11-*cis*-retinal are promoted to a π^* orbital. The excitation reduces the π component of the double bond allowing a "free" rotation about that bond and the all-*trans*-retinal is formed. This process occurs in 200 fs with a quantum yield of 0.67 [42]. The light excitation is crucial as spontaneous isomerization in the dark would only occur once in 1000 years [43]. It is worth to note that isomerisation of 11-*trans*-retinal is slower when in solution suggesting that the protein also plays a role in the isomerisation. One possible speed-up mechanism can rely

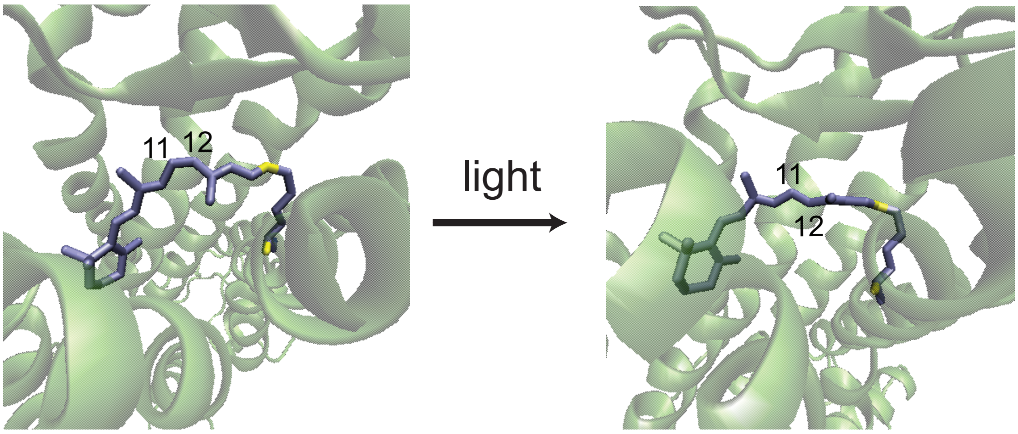

Fig. 1.5: Views from the seven helices of opsin before and after the *cis-trans* isomerization.

on the fact that the dihedral angle $C_{10}C_{11}C_{12}C_{13}$ was found to be 42° in the retinilydene instead of 0° in the unbound case [1].

Fig. 1.6 shows a schematic representation of how the transmembrane helices of the GPCR are affected by the isomerisation of the retinylidene chromophore.

The photoisomerisation step is crucial in the visual transducing process. Despite a lot of studies have been carried out on this subject, still a lot of unanswered questions exist. They mainly concern on why the process is so fast, selective and efficient. The isomerization process is also a central spot for this work and will be later discussed in more details (Sec. 1.3).

2. *Conformational Changes Following the Isomerization*

The rhodopsin's conformer containing the all-*trans* isomer of retinal is known as bathorhodopsin. The all-*trans*-retinal does not fit well into the protein, due to its rigid, elongated shape. It, therefore, adopt a twisted conformation, which is energetically unfavorable. As a consequence of that, a series of changes occur and the chromophore is finally expelled from the protein (see Fig. 1.7a).

Although the initial isomerisation occurs without any change in the shape of the opsin protein, the twisted conformation of all-*trans*-retinal in bathorhodopsin is too unstable to remain in this configuration for long. Within nanoseconds (10^{-9} s), the protein begins to change its conformation through a series of transient intermediates Fig. 1.7a. During the transition from metarhodo-

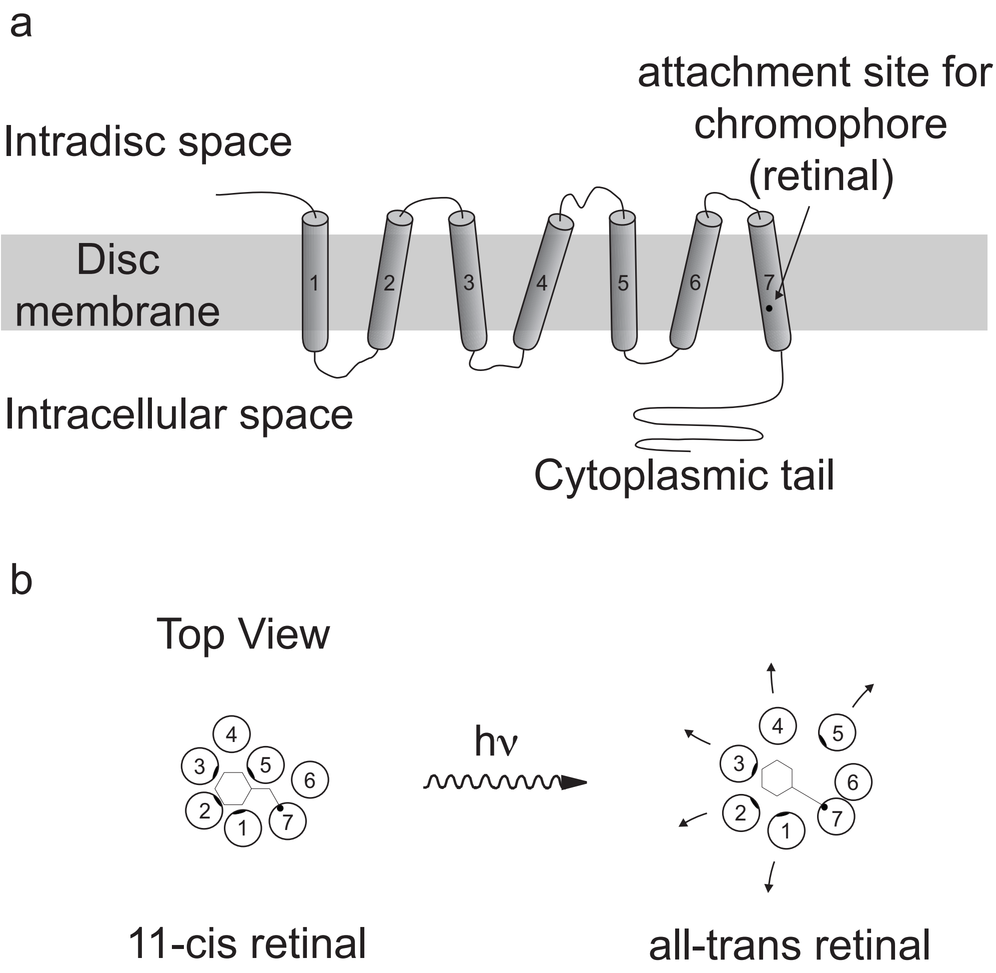

Fig. 1.6: a) The seven transmembrane helices sit in the membranous discs within the rod cells. The chromophore attachment site is in helix VII. b) Top view of the seven transmembrane helices before and after the absorption of a photon. Adapted from Ref. [3]

psin I to metarhodopsin II the protonated Schiff base linkage becomes deprotonated (Fig. 1.7b) which is then hydrolysed yielding free opsin plus free all-*trans* retinal. The all-*trans* retinal is reduced to all-*trans* retinol which is oxidised and isomerised in the dark to 11-*cis* retinal to generate rhodopsin by the formation of a protonated Schiff base linkage. Rhodopsin intermediates (each with a characteristic maximum of absorption in the visible spectrum) have been isolated at low temperatures. Name and duration of each step and the temperature of these intermediates are shown in Fig. 1.7a and discussed in more details in Sec. 1.3.

3. *Signal Transduction Cascade*

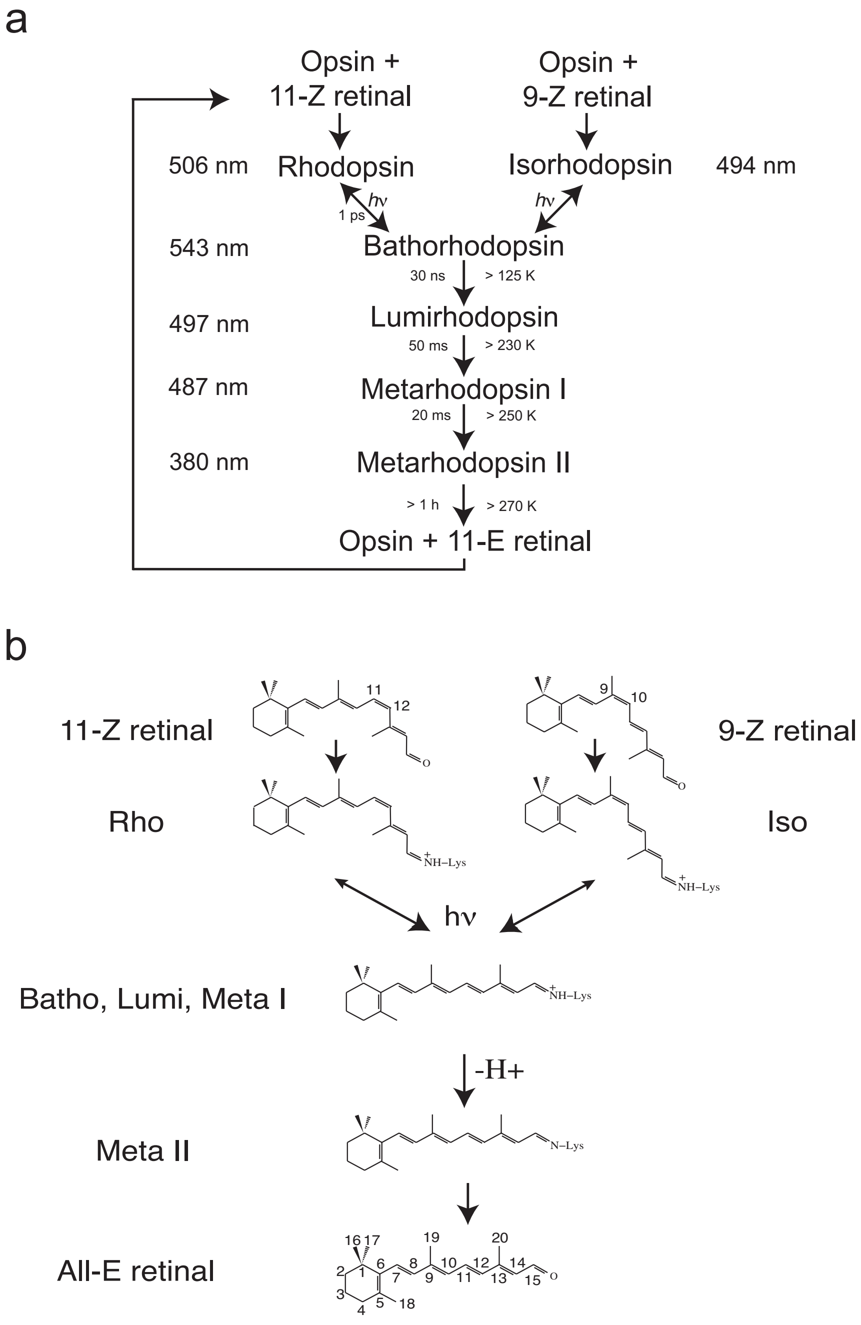

Fig. 1.7: a) A schematics of rhodopsin's photocycle. The numbers in nanometers are the maximum of absorption of the corresponding rhodopsin's photointermediate. The timings represent its lifetime and the temperatures in Kelvin are the upper thresholds below which the photointermediate can be stably trapped. b) Structure assumed by retinal in the different photointermediates of rhodopisin photocycle. Adapted from Ref. [4].

The most important photointermediate for vision to occur is metarhodopsin II. This intermediate activates the enzyme transducin, which starts the signal

transduction cascade resulting in production of a nerve impulse to the brain. After the metarhodopsin II is formed four more steps occur. The photointermediate complexes the enzyme transducin in order to activate it. This, in turn, activates another enzyme (phosphodiesterase) that acts in catalyzing the hydrolysis of cyclic guanine monophosphate (GMP) into a phosphodiester. The cyclic GMP is required to keep open the Na^+ channel (sodium cations are free to enter the rod cells since the cell is more negative than the external environment thus attracting positive charges). With the phosphodiester formation the channel is closed. The cell becomes more and more negatively charged with respect to its environment (this state is called "hyperpolarization" of the cell) and the large electrical potential difference between the cell and the environment travels as an electrical impulse down along the rod cell to the synaptic terminal and is, then, transferred to an adjoining nerve cell. The nerve cell carries the impulse all the way to the brain.
The activation process of a G-protein by a GPCR (where the activated G-protein (indicated by G^*_α) is the transducin in the case of rhodopsin) is sketched in Fig. 1.8.

Rhodopsin switches from the inactive to the active form after the binding of a ligand. In its inactive state, rhodopsin is free to diffuse across the cell membrane and when activated it becomes able to interact with the G-protein. The activation mechanism involves three dimensional structural changes in both the GPCR (rhodopsin) and the related G-protein (transducin). These structural changes induce biochemical signals which initiate a cascade of amplification inside the cell. During the activation process retinal plays a dual role, both as a chromophore in the initial rapid photochemistry and, after relaxation of the photoexcited state, as an agonist in producing the active state of the receptor (metarhodopsin II).

To summarize the whole mechanism in few words: the activation is due to light photons; when the light reaches rhodopsin, the 11-*cis*-retinal absorbs photons and isomerises to all-*trans*-retinal; the isomerization event causes the protein to change its shape; the shape change, ultimately, leads to the generation of a nerve impulse to the brain.

Cross-linking studies [6] indicates that a large movement of the β-ionone ring is involved in forming metarhodopsin II (see Fig. 1.9).

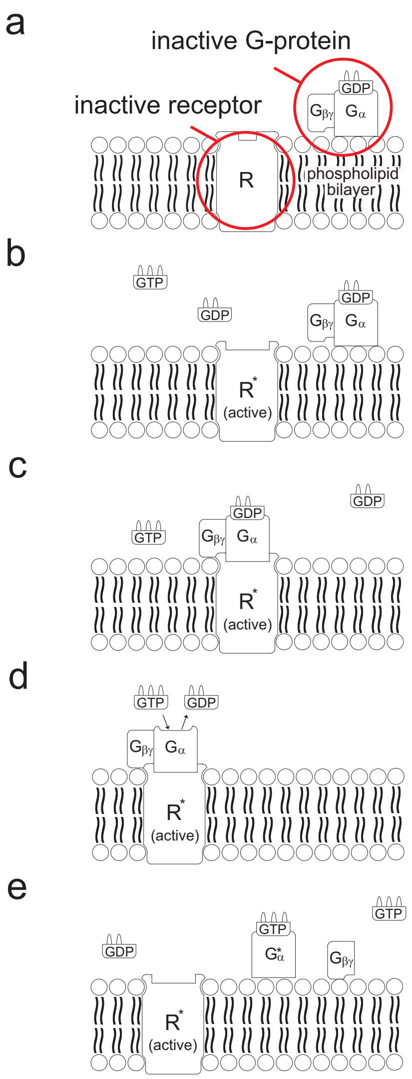

Inactive G-protein receptor and inactive G-protein

G-protein receptor is activated, in the case of rhodopsin, by light. By means of diffusion, the receptor encounters an inactive G-protein

The Gα part of the G-protein temporarily binds to the exposed surface of the activated receptor molecule

As a result of interacting with the receptor, the GDP molecule is replaced by a GTP molecule, which converts the subunit into its activated form

The active state of the Gα subunit, G*α, separates from the receptor and the Gβγ portion of the G-protein

Fig. 1.8: Activation of a G-protein by a GPCR: (a) the inactive GPCR; R sits in the membrane and the inactive G-protein diffuses about. The G-protein consists of three sub-units α, β and γ and a GDP molecule. When both are in their inactive state, there is no interaction between them. (b) On the activation, the GPCR changes its configuration ready to accept a G-protein. The G-protein encounters the activated GPCR, R*, purely by diffusion. (c) The G-protein binds R*. (d) GDP is displaced by GTP, resulting in the active G-protein. (e) The α-subunit falls away from the βγ subunit. G^*_α interacts with the target protein, which in turn sends signals into or out of the cell. After this step, the GTP is hydrolysed and the G-protein returns inactive. Adapted from Ref. [5]

It was proposed that the β-ionone ring, close to W265 in rhodopsin and bathorhodopsin, resides close to A169 in metarhodopsin II. This is accompanied by changes in the helical structure. This conformational switching of the chromophore might require reorganization of the helical structure of helix VII leading to disruption of the salt bridge between Glu113 and Lys296 [41] and movement of a proton

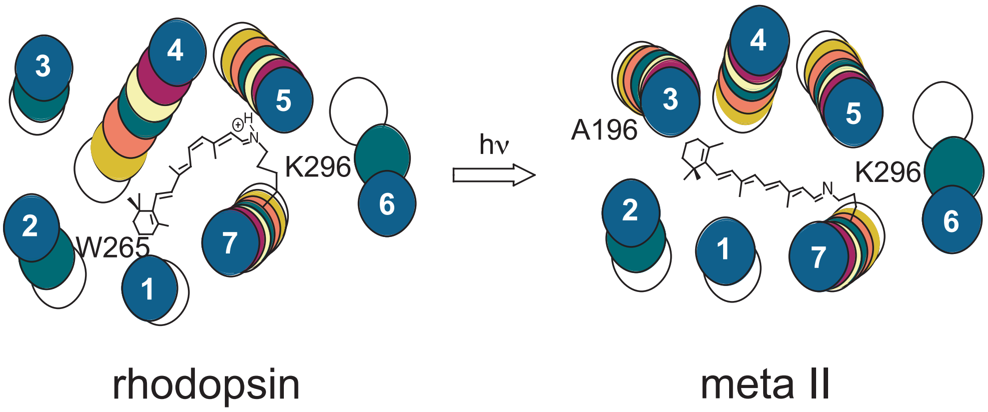

Fig. 1.9: The large displacement of the β-ionone ring between rhodopsin and metarhodopsin. Adapted from Ref. [6]

[44].

As shown in Fig. 1.9, there is a reorganization of the transmembrane helices after the conformational change in the chromophore [45, 30]: helix VII moves away from helix I and helix VI moves away from the other helices.

1.3 The Photointermediates of Rhodopsin

Absorption of a photon provides rhodopsin with the energy to form the active state. As shown in Fig. 1.10, the activation process can be divided in three phases: 1) cis-trans isomerization of the retinal; 2) thermal relaxation of the retinal-protein complex; and 3) the late equilibria that are affected by the interaction of rhodopsin with the G-protein.

About two-thirds (38 kcal mol^{-1}) of an energy of 57 kcal mol^{-1} (238 kJ mol^{-1}) taken up by light absorption are stored in the photoisomerized chromophore-(all-trans-retinylidene)-opsin complex [46, 47], lifting the receptor from the 11-cis-retinal-opsin conformation, via photorhodopsin, to bathorhodopsin (Fig. 1.10) . The primary photoproduct, i.e. photorhodopsin, is formed on an ultrafast time scale [48] as has been observed by Raman spectroscopy. It has not been trapped yet. Photorhodopsin thermally relaxes within a few picoseconds to bathorhodopsin, the first thermally equilibrated intermediate of the rhodopsin photocycle. The total quantum yield for the conversion of rhodopsin to bathorhodopsin is 0.67 [42] which means that more then half of the photons are used to isomerize the molecule. The intermediate can be trapped at a temperature approximately below 120 K [4] and its UV-

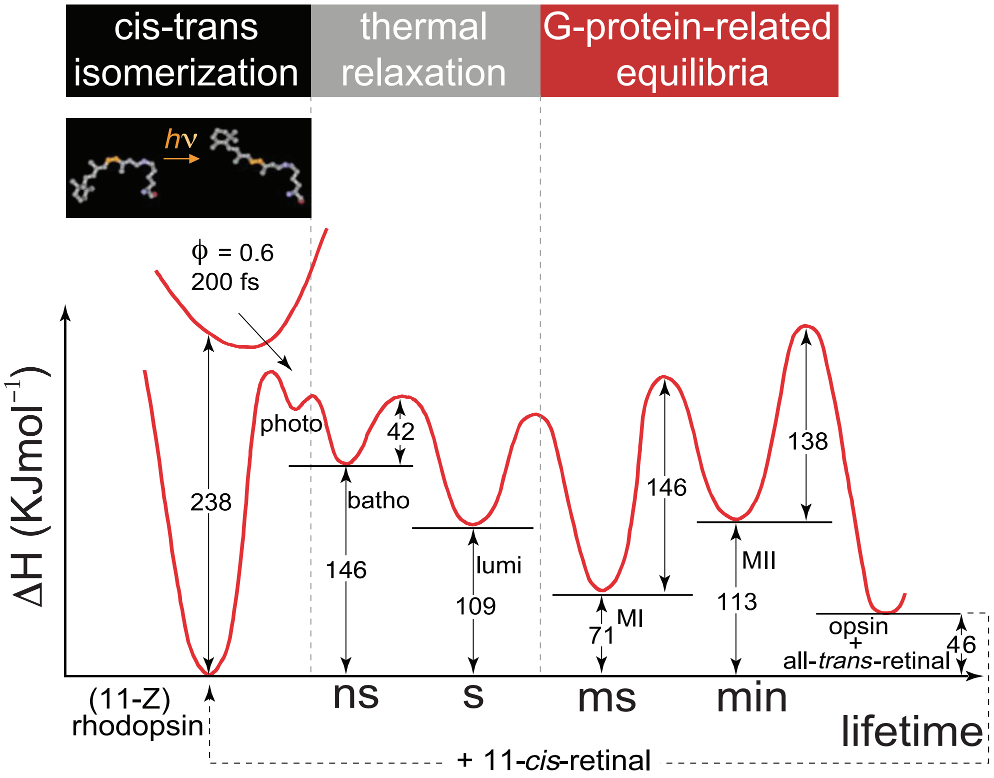

Fig. 1.10: An energy plot of rhodopsin photocycle. The vertical axis reports the energy in kJ mol^{-1} for each photointermediate scaled to rhodopsin (assumed zero). The horizontal axis reports the lifetime of the various photostates. ϕ is the quantum yield for the conversion from the excited state to the bathorhodopsin photointermediate.

visible absorption spectrum is red shifted with respect to rhodopsin. Note that the retinylidene part is now in its all-*trans* conformation and is still bonded to Lys296 residue through an imine bond (-C=N-, also known as Schiff base - Fig. 1.7b). The nitrogen atom of the imine bond is positively charged. Isomerization might proceed by rotation around the Schiff-base side of the double bond between C11 and C12 of the retinal, which would bring the polyene chain closer to the side chain of Ser186 (see Fig. 1.4). The interconversion step between rhodopsin and bathorhodopsin happens within 30 ns. Lumirhodopsin intermediate can be trapped at a temperature of about 220 K. The retinilydene part is still the same as in bathorhodopsin (Fig. 1.7b).

However, lumirhodopsin is not the only possible way of photoconversion of bathorhodopsin. In fact, it can interconvert into a new photoisomer known as isorhodopsin. Isorhodopsin is quite close in energy to rhodopsin (just 5 kcal/mol above) [7] and is characterized by containing the 9-*cis*-retinylidene conformer. The interconversion from bathorhodopsin to isorhodopsin happens within few nanoseconds with a quantum yield of 0.22. When this occurs the photoconversion reaches a quite stable intermediate and remains stalled. Reconversion of isorhodopsin into bathorhodopsin is needed to proceed towards metarhodopsin II photointermediate.

Metarhodopsin I is transiently formed and rapidly decays to metarhodopsin II [22]. The photoconversion from lumirhodopsin to metarhodopsin I happens within 50 ms and the photoisomer can be trapped at a temperature of about 250 K. The conformation of the chromophore is still the same as in bathorhodopsin and lumirhodopsin.

Finally, within 20 ms the metarhodopsin I photoisomer is converted to metarhodopsin II. The positive enthalpy of metarhodopsin II formation indicates that molecular interactions built up in metarhodopsin I are lost upon transition to metarhodopsin II. To drive the conversion, the entropy, and thus the overall disorder in the protein, must increase. The intermediate metarhodpsin II is the signaling state capable of interacting with the G-protein [4]. As explained before, formation of metarhodopsin II accompanies a large blue shift in the absorption maximum, the breakage of the stabilizing salt bridge between the negatively charged side chain of Glu113 and the protonated Schiff base [29], and the motion of transmembrane helices [45, 30]. All of those events occur within milliseconds.

Generally speaking, proton-transfer reactions occur when factors such as the relative orientation and distance of proton donor and acceptor are favorable. Therefore, proton-transfer can be an indicator of conformational changes.

1.4 Absorption Spectra

As shown in Fig. 1.7a, the distorted all-*trans* chromophore of bathorhodopsin may itself be photoisomerized, leading to either the starting 11-*cis*-state (i.e. rhodopsin), or to the 9-*cis* side product (i.e. isorhodopsin) [7]. The three species have different optical absorption spectra, as sketched in Fig. 1.11.

The absorption spectra and wavelength-dependent quantum yields of rhodopsin, bathorhodopsin and isorhodopsin have been thoroughly documented [49, 7, 50].

The maximum of absorption for rhodopsin is 505 nm which falls in the yellow-green region of the electromagnetic spectrum. The absorptivity is at a minimum (nearly zero) for wavelengths higher then 600 nm, i.e. in the red region of the spectrum. This implies that the sample can be safely handled under dim red light. Finally, the extremely high molar absorptivity of rhodopsin makes very difficult the

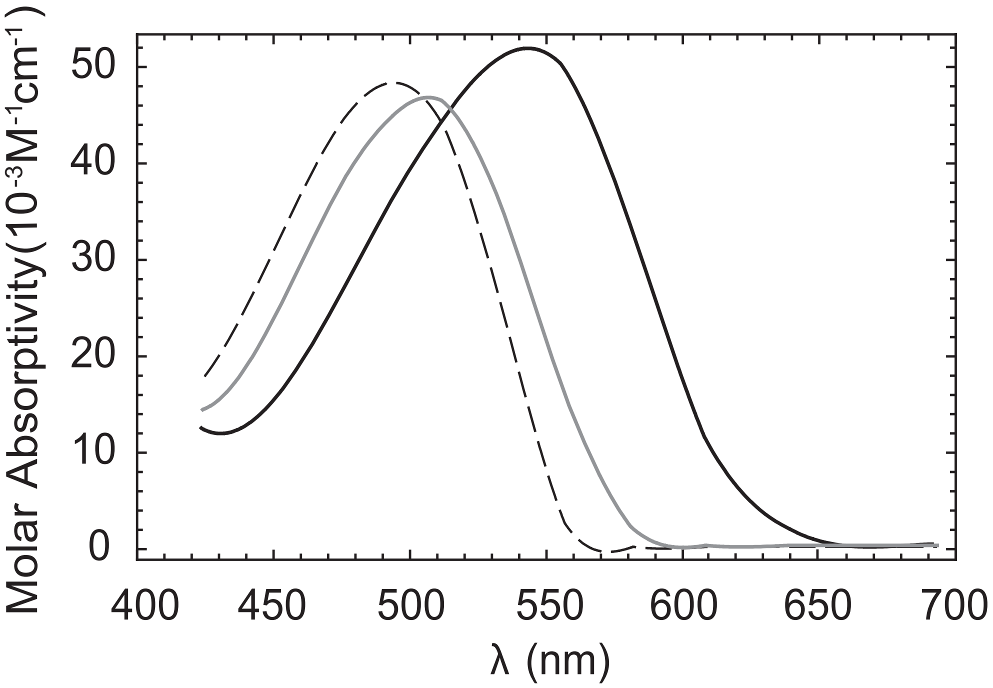

Fig. 1.11: The absorption spectrum of rhodopsin (solid gray line), bathorhodopsin (solid black line) and isorhodopsin (dotted black line) at 77K. Reproduced from Ref. [7].

penetration of the light deep into the sample.

Bathorhodopsin has its maximum of absorption around 543 nm. The molar absorptivity is slightly higher than rhodopsin and there is an appreciable absorption even in the red region. More interesting, is the fact that the molar absorptivity of bathorhodopsin is quite high at the maximum of absorption of rhodopsin which means that while irradiating at 505 nm rhodopsin is converted to bathorhodopsin but, at the same time, a certain amount of bathorhodopsin is converted back to rhodopsin or forward to isorhodopsin.

The maximum of absorption of isorhodopsin is about 492 nm which is very close to rhodopsin. This means that irradiating around 480 nm both rhodopsin and isorhodopsin are converted to bathorhodopsin, part of which, in turn, is converted back to rhodopsin and isorhodopsin.

Many early NMR studies on rhodopsin photointermediates did not pay much attention to the issue of light penetration and the possible generation of multiple photoisomers. For example, several studies of the photostate metarhodopsin I used illumination of rhodopsin by white light under cryogenic conditions, followed by warming up to 250 K, to trap the metarhodopsin I photostate [51, 52]. However, as shown in this thesis, these conditions are much more likely to accumulate the photostate isorhodopsin rather than metarhodopsin I. This calls into question some of the conclusions of those studies.

1.5 State of Art of Rhodopsin Studies

In this section, a very short overview on what has been already done on this membrane protein is given. The information come from several sources: diffraction, vibrational, optical and NMR spectroscopy plus quantum mechanical calculations.

- *Optical Studies*

  The optical studies at variable temperature [49], clarified the main photointermediate states of rhodopsin. The temperature below which they can be trapped are listed in Fig. 1.7. Each intermediate of rhodopsin is clearly distinguishable in terms of a shift in absorbance band, λ_{max}, in its UV-Vis spectrum [49, 48]. An estimate of the time-scales for the formation of the different photointermediates, as listed in Fig. 1.7, also comes from optical measurements.

- *X-Ray Studies*

  Diffraction data [2] produced an high resolution (2.6 $\AA$) structure of rhodopsin that allows the identification of the protein fragments determining the size and shape of the binding pocket as well as the role of water in the proximity of the chromophore. These structural data are of great importance for a deeper understanding of the chromophore structure, since they reveal which groups are in a range to affect the retinylidene, either directly or through a hydrogen-bonding network, and thereby allow a better description of the electrostatic and steric interaction between the chromophore and the surrounding. A more recent 2.7 $\AA$ X-ray structure of bathorhodopsin has verified the distorted all-*trans* configuration of the chromophore and also identified various structural changes in the immediate protein environment, including a small displacement of the negatively charged Glu113 counterion relative to the positively-charged nitrogen atom of the protonated Schiff base (PSB) linking the chromophore to the Lys296 sidechain of the opsin protein [53].

- *Vibrational Data*

Vibrational studies by means of FT-IR and Raman spectroscopy provide insight into the bond distribution and the general conformation of the observed molecule. The information on bond distances and angles are, however, not quantitative due to the complexity of the system and to the strength of the coupling between vibrational modes of similar frequency.
Raman spectroscopy gives a clear indication of the following facts:

  - the fingerprint region of 11-*cis* retinal PSB in solution and rhodopsin are quite similar, confirming a general similarity in conformation and bond orders [54]. The differences may be related to the protein environment and to the photoreaction pathway;
  - there is a significant hydrogen out-of-plane (HOOP) distortion about the C11=C12 bond [55], believed to be an important normal coordinate in the fast isomerization [56];
  - there is a significant chain distortion out of the molecular plain in the C10—C13 region due to the steric interaction between C10 and the methyl group bonded to C13. This is of key importance for the efficient conversion to the first photointermediate [38];
  - bathorhodopsin seems to have a highly twisted all-*trans* structure [57, 58];
  - precise time measurements for the very first step in the photocycle show only minor differences in the vibrational spectra of photo- and bathorhodopsin, indicating high similarity in structure and interactions with the protein pocket [59].

- *Previous NMR Data*

  Several NMR studies have also been performed and hypotheses confirmed by the high-resolution XRD structure. Here we recall some of the previous NMR data, with particular attention towards the constraints on the chromophore structure:

  - chemical shift tensor estimation of the chromophore [60];
  - low temperature isotropic chemical shift determination of rhodopsin, bathorhodopsin and isorhodopsin [11, 61]. These studies support a mechanism of energy storage that does not involve significant charge separa-

  tion [62]. Chemical shift differences between some labeled sites in rhodopsin and model compounds suggest electrostatic interactions within the pocket in the vicinity of C13;

  - HCCH torsion angle measurements around C10-C11 bond [63, 51] (ϕ = 160° ± 10° in rhodopsin and ϕ = 180° in metarhodopsin I);
  - rotational resonance distance determination ($r_{10,20} = 304 \pm 15$pm and $r_{11,20} = 293 \pm 15$pm). These data have been used to determine a torsional angle of 44° between the C6-C10 and C13-C15 plane. Measurements have been also done on metarhodopsin I and a distance $r_{10,20} > 430$ pm was estimated [52];
  - evidence of a complex counterion involving mainly the negatively charged carboxylate residue Glu113 and a structural water molecule [64, 35];
  - ^{2}H-NMR of aligned samples, deuterated at specific methyl group, provide the orientation of the C5-C18H$_3$ [65]. The data suggest a 6s-*trans* conformation as the most favorable although X-ray structures did not agree with this conclusion [23].
  - studies on fully ^{13}C labelled retinylidene chain [34, 66] and determination of isotropic ^{13}C and ^{1}H chemical shifts;

- *Quantum Mechanical Calculation*

  Ab-initio quantum mechanical calculation [67, 68] have been done in order to estimate the structure and the isotropic chemical shift distribution of the molecule. Theoretical ^{13}C isotropic chemical shift and CSA calculation have been used to predict conformation of specific fragments and charge delocalization [69] even if the authors themselves suggest caution in the data interpretation. The ground state of rhodopsin was investigated by Buda *et al* in 1996, using density functional theory (DFT) and the Car-Parrinello *ab initio* approach. More recently Sugihara *et al.* investigated the structure of the retinal PSB in rhodopsin using molecular dynamics DFT calculation. The electronic structure of bathorhodopsin has been modelled using density functional theory [70, 58], QM/MM [15, 71] and molecular dynamics [72] calculations, but in general the level of agreement between the reported NMR chemical shifts [11, 61] and the calculated values has been quite poor.

This thesis adds a few more pieces of information to the knowledge of rhodopsin reporting some experimental data on the first stable photointermediate in the photocycle by means of double-quantum solid state NMR. All the information obtained on rhodopsin, whether by UV/Vis, X-ray diffraction, IR or Raman spectroscopy, solution or solid-state NMR, all contribute to a bigger picture, which allows direct calculation of structural refinements and theoretical calculations used for modelling.

1.6 Open Questions

Despite the number of studies focused on rhodopsin and above briefly summarized, there is still debate about how the protein pocket assists the photoisomerization process. In particular the initial protonation state of another carboxylate residue Glu181 is the central point of a controversy opposing two models for the detailed photoactivation mechanism. A "counterion switch" model has been suggested [73] that proposes that the Glu181 residue on the second extracellular loop acts as the primary proton acceptor from the Schiff base during the photoactivation. Glu181 being neutral and protonated in the dark state transfers a proton through a H- bond network involving two water molecules, Ser186 and Glu113 as the final proton acceptor. This model was later challenged by FT-IR studies that suggest Glu181 and Glu113 are both in a charged deprotonated state during the dark state, thus preventing a counterion switch [74]. On the other side, it was suggested that both sites operate in a "complex-counterion" with Glu113 acting as the primary counterion in the inactive state while in the later photointermediate states, Glu181 becomes the primary counterion with some contribution by Glu113. This would originate from a rearrangement of internal hydrogen bond networks occurring during photoactivation. Quantum-chemical calculations have yielded evidence in favor of either model[74, 40, 62, 18, 13, 15, 75, 76, 77, 78].

A more intriguing point (and more relevant to this work) is the debate about how bathorhodopsin stores two thirds of the absorbed photon energy. The mechanism of energy storage inside this photointermediate, as well as the origin of its bathochromic shift, are closely related to the mechanism and pathway of photoactivation. The first model proposed in 1979 by Honig et al. [32] suggested that the 11-*cis* to all-*trans* photoisomerization results in a separation of the positively charged PSB from its counterion in bathorhodopsin. FT-IR spectroscopy studies [79, 80, 81, 82] showed that a hydrogen bonded water network involving Glu113 is significantly modified upon formation of bathorhodopsin. The large body of Raman data has rather been interpreted as indicative for intramolecular strain to be a major contributor to the energy storage [73, 57, 58]. Recent X-ray crystal structures provide more detailed structural models for rhodopsin [2] and bathorhodopsin [53]. Due to their limited resolution, these structures do not provide direct clues for the energy storage mechanism, but they do provide a very useful framework for hybrid quantum mechanical/molecular mechanical (QM/MM) [15, 71], molecular dynamics (MD) [72], and density functional theory (DFT) [70, 58] calculations. These calculations led to several models assessing the respective contributions of intramolecular strain, electrostatic interaction, and chromophore/protein van der Waals interactions to the energy storage mechanism. Solid state NMR measurements on rhodopsin photointermediates provide chemically resolved data on the chromophore from which precise information on electronic charge distribution can be derived; this may be really valuable for testing the different models suggested by computational methods or other possibilities. Unfortunately, an early attempt to measure ^{13}C chemical shifts in bathorhodopsin [61, 11] appears to have been methodologically flawed.

In this thesis, a quite different set of retinylidene chain ^{13}C chemical shift data in bathorhodopsin were obtained using custom-built hardware, with a careful control of the sample temperature and with an improved and precise illumination protocol. These new and modern hardware facilities (developed on purpose) were combined with modern double-quantum NMR techniques to allow selective observation of the retinylidene ^{13}C signals. The mechanistic conclusions drawn from the earlier solid-state NMR study, which detected only small chemical shift changes between rhodopsin and bathorhodopsin [61, 11], must be reassessed.

PART II: THEORY

2. THE SPIN HAMILTONIAN IN SOLID-STATE NMR

Solid-state NMR methods provide several powerful biophysical tools for mapping structure and dynamics in biomolecules. These tools are especially promising for studying important systems that are inaccessible to crystallography or solution NMR, such as membrane proteins. The solution state NMR spectrum of a sample with only one type of NMR active spin is a sharp single line. This is due to the rapid isotropic molecular motion which averages out all the anisotropic interactions either to zero in the case of dipole-dipole and quadrupole interactions or to their isotropic component as in the case of the chemical shift. For static or slowly tumbling molecules these interactions are not completely averaged, which means broad NMR resonances with slow resolution and sensitivity. Both resolution and sensitivity may be improved significantly by rapid rotation of the sample about an axis fixed at the “magic angle” ($\beta_{mag} = 54.74°$), with respect to the static magnetic field. This technique, called magic-angle spinning (MAS), is able to remove or, at least, dramatically scale down the anisotropic interactions in order to produce a “liquid-like” high-resolution spectrum. Removal of dipolar couplings by MAS helps to narrow the ^{13}C or ^{15}N resonances, but also discards structural information (for example, the dipolar coupling between two nuclei is inversely proportional to the cube of the internuclear distance). Therefore, it is often desirable to temporarily recouple certain anisotropic spin interactions by applying pulse schemes of resonant *rf* fields to the nuclear spins, in order to suspend the averaging effect of the magic angle rotation over a limited time interval. These *rf* schemes are called *recoupling pulse sequences* [8] and the recoupling of dipolar couplings by *rf* pulse sequences is called *dipolar recoupling* [83].

2.1 Reference Frames

This chapter will make extensive use of objects such as spherical tensors that are frame dependent. A clear discussion of these frames is needed in order to fix the notation.

The ***Laboratory Frame*** is a Cartesian frame in which the $\overrightarrow{Z^L}$ axis lies along the static magnetic field $\overrightarrow{B}_0$. The frame is here dubbed either as LAB or L.

The ***Rotor Frame*** is a Cartesian frame in which the $\overrightarrow{z^R}$ axis lies along the rotor long dimension that in the case of MAS is tilted by the magic angle (β_{mag}) with respect to $\overrightarrow{B}_0$. The frame is here dubbed either as ROT or R.

The ***Molecular Frame*** is a Cartesian frame fixed on the molecule with axes labeled as $\overrightarrow{x^M}$, $\overrightarrow{y^M}$ and $\overrightarrow{z^M}$. The frame is here dubbed as MOL or M. Molecular symmetry can be exploited to fix the axes direction.

The ***Principal Axis Frame*** or Principal Axis System is a particular molecular frame in which a selected interaction is described by a diagonal tensor (the frame is principal for that specific interaction and, in general, different interactions have different principal axis systems). The same notation of the molecular frame is used for axes but the frame is now dubbed as PAS or P.

Fig. 2.1 shows these frames and their relationships.

2.2 The NMR Hamiltonian in Spherical Tensor Notation

A convenient way to write the nuclear Hamiltonian especially under MAS conditions is to factorize it into a part describing the interaction with the *rf* field and another one describing the internal spin interactions plus the interaction of the nuclear spins with the static magnetics field. Thus, the total Hamiltonian at time point t may be written as [84]:

$$H(t) = H_{rf}(t) + H_{int}(t) \tag{2.1}$$

where the internal spin Hamiltonian $H_{int}(t)$ is time dependent because of molecular motions, or when, as in the MAS technique, the whole sample is rotated; the *rf* spin Hamiltonian is time dependent because of the modulation of the *rf* field itself.

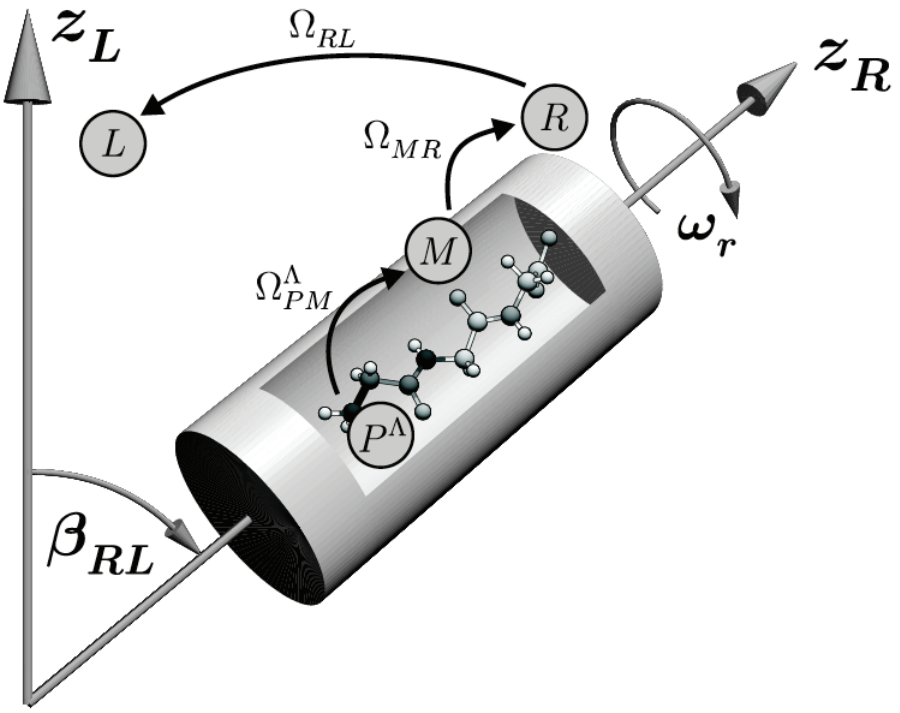

Fig. 2.1: Laboratory, rotor, molecular and principal axis frames and their transformations. Source: Ref. [8]

The internal spin Hamiltonian is better (and more compactly) written using spherical tensor notation [85] as:

$$H_{int}(t) = \sum_{\Lambda} \mathscr{C}^{\Lambda} \sum_{l} \sum_{m} (-1)^m [A^{\Lambda}_{l,m}]^L [\mathscr{T}^{\Lambda}_{l,-m}]^L \tag{2.2}$$

where $\mathscr{C}^{\Lambda}$ is a constant specific for the interaction Λ, $[A^{\Lambda}_{l,m}]^L$ is the space spherical tensor component of the interaction Λ with rank l and component m expressed in the frame L (laboratory frame) and $[\mathscr{T}^{\Lambda}_{l,-m}]^L$ is the spin-field spherical tensor operator. Since the static magnetic field is very high in conventional applications (and in all the case discussed in this thesis), the interaction with this field (Zeeman interaction) is the strongest among all the other interactions in the spin Hamiltonian above. Therefore, it is possible to neglect all the terms which do not commute with it as in a conventional perturbative approach. This constitutes a simplification and is often referred as *High Field Approximation* (HFA). In fact, it can be easily demonstrate that all the spherical tensor operators with $m \neq 0$ do not commute with the hamiltonian describing the Zeeman interaction and, therefore, only terms with $m = 0$ are retained, i.e.:

$$H_{int}(t) = \sum_{\Lambda} \mathscr{C}^{\Lambda} \sum_{l} [A^{\Lambda}_{l,0}]^L [\mathscr{T}^{\Lambda}_{l,0}]^L \tag{2.3}$$

The equation above can be rewritten on the basis of the following two observations: i) the static magnetic field is constant and ii) an external *rf* field is able to rotate the spin angular momenta. This means that we can factorize out the field from the spin-field spherical tensor operator $[\mathscr{T}^{\Lambda}_{l,-m}]^L$ which becomes, now, a pure-spin spherical tensor operator here indicated with $[T^{\Lambda}_{\lambda,-m}]^L$ where, at the same time, we changed the tensor rank from l to λ as the rank of the pure-spin tensor operator does not in general coincide with the rank of the spin-field one. Eqn. 2.3 can be rewritten as:

$$H_{int}(t) = \sum_{\Lambda} C^{\Lambda} \sum_{l,\lambda} [A^{\Lambda}_{l,0}]^L [T^{\Lambda}_{\lambda,0}]^L \tag{2.4}$$

where C^{Λ} is different from $\mathscr{C}^{\Lambda}$ as it can also contain (for some specific interaction Λ) the magnetic field.

2.3 *The Spin Hamiltonian under Magic Angle Spinning (MAS)*

In order to show where the MAS comes in, the time dependence of the spin Hamiltonian must be written explicitly. This is best done if a frame transformation is applied. Spherical tensors have very well defined rotational properties like:

$$[A_{l,m}]^F = \sum_{m'=-l}^{l} [A_{l,m'}]^{F'} D^{l}_{m',m}(\Omega_{F'F}) \tag{2.5}$$

i.e., any spherical tensor expressed in the frame F' can be rewritten in the frame F using Eqn. 2.5 where the Wigner matrices [86] ($D^{l}_{m',m}(\Omega_{F'F})$) are involved. $\Omega_{F'F} = \{\alpha_{F'F}, \beta_{F'F}, \gamma_{F'F}\}$ is the set of three Euler angles that describes the rotations between the two frames. Note that in the transformation of a spherical tensor between the frame F and F' the rank of the spherical tensor itself does not change while all the rank components (m') are mixed together. Wigner matrices can be also written as:

$$D^{l}_{m',m}(\alpha_{F'F}, \beta_{F'F}, \gamma_{F'F}) = e^{-im'\alpha_{F'F}} d^{l}_{m',m}(\beta_{F'F}) e^{-im\gamma_{F'F}} \tag{2.6}$$

where $d^{l}_{m',m}(\beta_{F'F})$ is an element of a reduced Wigner matrix.

These transformations can be applied to express the space part of all the internal interaction in Eqn. 2.3 in any desired frame. Of relevance to MAS is the transformation of these space parts into the rotor frame (R) as:

$$H_{int}(t) = \sum_{\Lambda} C^{\Lambda} \sum_{l,\lambda} \sum_{m} [A^{\Lambda}_{l,m}]^{R} e^{-im\alpha_{RL}} d^{l}_{m,0}(\beta_{RL}) [T^{\Lambda}_{\lambda,0}]^{L} \tag{2.7}$$

Here α_{RL} is the Euler angle that describes the rotation around the z-axis in the rotor frame ($\overrightarrow{z^R}$). Thus, since the rotor is spun with a frequency ω_r around its z-axis (MAS), $\alpha_{RL} = \alpha^0_{RL} - \omega_r t$, with α^0_{RL} the value of α_{RL} at the time t_0. β_{RL} is the angle between the rotor z-axis and the laboratory z-axis, that under MAS, it is the so called magic angle $\beta_{RL} = \beta_{mag} = arctan(\sqrt{2}) = 54.74°$. In a more compact form we can write:

$$H_{int}(t) = \sum_{\Lambda} C^{\Lambda} \sum_{l,\lambda} \sum_{m} H^{\Lambda}_{l,m,\lambda,0}(t) \tag{2.8}$$

with

$$H^{\Lambda}_{l,m,\lambda,0}(t) = [A^{\Lambda}_{l,m}]^{R} e^{-im\alpha_{RL}} d^{l}_{m,0}(\beta_{RL}) [T^{\Lambda}_{\lambda,0}]^{L} \tag{2.9}$$

The ranks l and λ, which are specific for the interaction Λ, are also called rotational signatures. Their value for the interactions relevant to this thesis are resumed in Tab. 2.1.

2.4 NMR Interactions

Before describing the nature of the spin interactions that are accounted for in the internal Hamiltonian a further observation will be used in order to simplify the Hamiltonian in Eqn. 2.3. Since all the NMR observable quantities are described by second rank tensors, the l indices run up to 2 (i.e. l=0,1,2). Moreover, all the terms with l=1 disappear when dealing with symmetric tensors [84]. This is certainly true for the dipolar and quadrupolar interaction while the symmetry of chemical shift and indirect spin-spin coupling tensors is yet not well clear. In the latter two cases, however, l=1 component may be neglected without any significant errors in routine NMR [84]. Combining these argumentation within the **HFA** regime Eqn. 2.3 may be written as:

$$H_{int}(t) = \sum_{\Lambda} \mathscr{C}^{\Lambda} \left([A^{\Lambda}_{0,0}]^{L} [\mathscr{T}^{\Lambda}_{0,0}]^{L} + [A^{\Lambda}_{2,0}]^{L} [\mathscr{T}^{\Lambda}_{2,0}]^{L} \right) \tag{2.10}$$

Tab. 2.1: Rotational signatures for some NMR interaction and values of the constant $\mathscr{C}^\Lambda$ for the relevant NMR interactions. Space, spin and spin-field spherical tensors components are also reported within the high field approximation.

Λ^a	l	λ	field rank	$\mathscr{C}^\Lambda$	$[\mathscr{T}^\Lambda_{l,m}]^L$	C^Λ	$[T^\Lambda_{\lambda,0}]^L$	$[A^\Lambda_{l,0}]^P$	$[A^\Lambda_{l,\pm 2}]^P$
Z	0	1	1	$-\gamma_j$	$-\frac{1}{\sqrt{3}}I_{jz}B_0$	$-\gamma_j B_0$	$-\frac{1}{\sqrt{3}}I_{jz}$	$-\sqrt{3}$	-
isoCS	0	1	1	$-\gamma_j$	$-\frac{1}{\sqrt{3}}I_{jz}B_0$	$-\gamma_j B_0$	$-\frac{1}{\sqrt{3}}I_{jz}$	$-\sqrt{3}\delta^j_{iso}$	-
J	0	0	0	2π	$-\frac{1}{\sqrt{3}}I_j I_k$	2π	$-\frac{1}{\sqrt{3}}I_j I_k$	$-\sqrt{3}J_{jk}$	-
Jan	2	2	0	2π	$\frac{1}{\sqrt{6}}(3I_{jz}I_{kz}-I_jI_k)$	2π	$\frac{1}{\sqrt{6}}(3I_{jz}I_{kz}-I_jI_k)$	$-\sqrt{6}J^{an}_{jk}$	-
CSA	2	1	1	$-\gamma_j$	$\sqrt{\frac{2}{3}}I_{jz}B_0$	$-\gamma_j B_0$	$\sqrt{\frac{2}{3}}I_{jz}$	$\frac{\sqrt{3}}{2}(\delta^j_{zz}-\delta^j_{iso})$	$\frac{\eta^j}{2}(\delta^j_{zz}-\delta^j_{iso})$
DD	2	2	0	1	$\frac{1}{\sqrt{6}}(3I_{jz}I_{kz}-I_jI_k)$	1	$\frac{1}{\sqrt{6}}(3I_{jz}I_{kz}-I_jI_k)$	$\sqrt{6}b_{jk}$	0

[a] Interactions are: Zeeman (Z), isotropic chemical shift (isoCS), indirect spin-spin coupling (J), indirect spin-spin coupling anisotropy (Jan), chemical shift anisotropy (CSA) and direct dipole-dipole coupling (DD).

γ_j is the magnetogyric ratio for the k-th nucleus.

B_0 is the static magnetic field.

δ^j_{iso} is the isotropic chemical shift for the j-th atom.

δ^j_{zz} is the zz component (expressed in the PAS) of the chemical shift spatial tensor.

$\eta^j = (\delta^j_{yy}-\delta^j_{xx})/(\delta^j_{zz}-\delta^j_{iso})$

J_{jk} is the homonuclear isotropic coupling constant

b_{jk} is the homonuclear dipolar coupling constant defined as $b_{jk} = -\mu\gamma_j\gamma_k\hbar/4\pi r^3_{jk}$.

We are now in the position to describe the spin interactions that may occur in the spin Hamiltonian. We do that by explicitly writing down their Hamiltonian.

2.4.1 Zeeman Interaction

The Zeeman interaction expresses the interaction of spin moments with external magnetic fields. It can be classically written as:

$$\widehat{H}_Z = -\overrightarrow{\mu} \cdot \overrightarrow{B} \tag{2.11}$$

where $\overrightarrow{\mu}$ is the magnetic moment and $\overrightarrow{B}$ is a static magnetic field. Since:

$$\overrightarrow{\mu_j} = \gamma_j \mathbf{I}_j \tag{2.12}$$

then:

$$\begin{aligned}\widehat{H}_Z &= -\sum_j \gamma_j \mathbf{I}_j \cdot \mathbf{1} \cdot \overrightarrow{B} \\ &= -\sum_j \gamma_j B_0 \mathbf{I}_{jz} \\ &= \sum_j \omega_0^j \mathbf{I}_{jz}\end{aligned} \tag{2.13}$$

Note that the static magnetic field $\overrightarrow{B}$ has been considered aligned with the $\overrightarrow{Z}^L$ axis with $B_z = B_0 \neq 0$ and $B_x = B_y = 0$. In the notation of Sec. 2.2 the space and the spin-field part of the Zeeman Hamiltonian are easily identified by writing:

$$\widehat{H}_Z = \mathscr{C}^Z \sum_j [A_{0,0}^{Z,j}]^L [\mathscr{T}_{0,0}^{Z,j}]^L \tag{2.14}$$

Remembering that for isotropic (rank zero) interactions the space part assumes the same value in any reference frame as it must be invariant by definition of the trace:

$$[A_{0,0}^{\Lambda}]^{F'} = [A_{0,0}^{\Lambda}]^F \tag{2.15}$$

for any F and F' that are related by an Euler rotation. Thus:

$$[A_{0,0}^{Z,j}]^P = [A_{0,0}^{Z,j}]^L \tag{2.16}$$

and, according to Tab. 2.1:

$$\begin{aligned}
\mathscr{C}^{Z} &= -\gamma_j \\
[A^{Z,j}_{0,0}]^{P} &= -\sqrt{3} \\
[\mathscr{T}^{Z,j}_{0,0}]^{L} &= -\frac{1}{\sqrt{3}}\mathbf{I}_{jz}B_0
\end{aligned} \tag{2.17}$$

2.4.2 Interaction with a r.f. Field

Interaction with a r.f. field is very similar to the Zeeman interaction. In this case the relevant Hamiltonian is

$$H_{rf}(t) = -\sum_j \gamma_j \mathbf{I}_j \cdot \mathbf{1} \cdot \overrightarrow{B}_{rf}(t) \tag{2.18}$$

where the r.f. field may be written as:

$$\overrightarrow{B}_{rf}(t) = 2B_{rf}\cos(\omega_1 t + \phi)\overrightarrow{\mathbf{e_X}} \tag{2.19}$$

with B_{rf} being the amplitude of the field, ω_1 its frequency, ϕ its phase and $\overrightarrow{\mathbf{e_X}}$ a unity vector along the $\overrightarrow{X}^{L}$ direction. From basic mathematics such an oscillating vector may be decomposed into two vectors rotating in opposite directions. Only the one rotating in the same sense as the spin precession may induce transition.

The Rotating Frame

A rotating frame is now introduced where $\overrightarrow{Z^r}$ axis coincides with $\overrightarrow{Z}$ in the LAB frame while $\overrightarrow{X^r}$ rotates in the same direction of r.f. field component that induces transitions at the frequency $\omega_1/2\pi$. In this new frame the r.f. Hamiltonian of Sec. 2.4.2 loses its time dependence and is written as:

$$H_{rf} = \sum_j \omega^{j}_{nut}(\mathbf{I}_{jx}\cos(\phi) + \mathbf{I}_{jy}\sin(\phi)) \tag{2.20}$$

where $\omega^{j}_{nut} = |\gamma_j B_{rf}|$ is the nutation frequency of the r.f. field. The use of the rotating frame implies an additional term that may be included into the Zeeman Hamiltonian by substituting ω_0 with $\Omega_0 = \omega_0 - \omega_1$. *From now on, all Hamiltonians will be written in the rotating frame.*

2.4.3 Chemical Shift Interaction

The chemical shift interaction originates from the shielding/deshilding of the static field $\overrightarrow{B}$ due to electron clouds in the molecule. i.e. the interaction between a spin and the static field is mediated by the electron clouds. This can be described introducing a shielding tensor (δ) as:

$$\begin{aligned} H_{isoCS} &= -\sum_j \gamma_j \mathbf{I}_j \cdot \delta^j \cdot B_0 \\ &= -\sum_j \gamma_j \cdot \delta^j_{ZZ} B_0 \mathbf{I}_{jz} \\ &= \sum_j \omega^j_0 \cdot \delta^j_{ZZ} \mathbf{I}_{jz} \end{aligned} \tag{2.21}$$

The Cartesian tensor δ may be expressed in irreducible spherical components of rank l=0,1,2 [84]. The 0-th rank component is called *isotropic chemical shift* and is equal to:

$$\delta_{0,0} = \delta^j_{isoCS} = \frac{1}{3}(\delta^P_{xx} + \delta^P_{yy} + \delta^P_{zz}) \tag{2.22}$$

The first rank component is called the *antisymmetric chemical shift* and may be, in first approximation, neglected, while the second rank component is called *chemical shift anisotropy* and will be discussed in the following.

As before, the spatial and the spin-field part of this interaction can be identified by writing:

$$H_{isoCS} = \mathscr{C}_{isoCS} \sum_j [A^{isoCS,j}_{0,0}]^L [\mathscr{T}^{isoCS,j}_{0,0}]^L \tag{2.23}$$

recalling Eqn. 2.15 and with (see Tab. 2.1)

$$\begin{aligned} \mathscr{C}^{isoCS} &= -\gamma_j \\ [A^{isoCS,j}_{0,0}]^P &= -\sqrt{3}\delta^j_{iso} \\ [\mathscr{T}^{isoCS,j}_{0,0}]^L &= -\frac{1}{\sqrt{3}} \mathbf{I}_{jz} B_0 \end{aligned} \tag{2.24}$$

2.4.4 Chemical Shift Anisotropy Interaction

The chemical shift anisotropy interaction is due to the second rank irreducible component of the chemical shift tensor, δ. If we define the *anisotropic chemical shift* *frequency* ω^k_{an}, the CSA Hamiltonian may be easily written as:

$$H_{CSA} = \sum_j \omega^j_{an} \mathbf{I}_{jz} \tag{2.25}$$

and the space and the spin-field part identified by:

$$H_{CSA} = \mathscr{C}^{CSA} \sum_j [A^{CSA,j}_{2,0}]^L [\mathscr{T}^{CSA,j}_{2,0}]^L \tag{2.26}$$

To work out this hamiltonian as function of the known quantities reported in Tab. 2.1, a further step is needed. Recalling Eqn. 2.5 we can write:

$$[A^{CSA,j}_{2,0}]^L = \sum_{m=-2}^{2} [A^{CSA,j}_{2,m}]^P D^2_{m,0}(\Omega_{PL}) \tag{2.27}$$

with Ω_{PL} the Euler angles that relates the frame P to the frame L. Eqn. 2.26 transforms into:

$$H_{CSA} = \mathscr{C}^{CSA} \sum_j \sum_{m=-2}^{2} [A^{CSA,j}_{2,m}]^P D^2_{m,0}(\Omega_{PL}) [\mathscr{T}^{CSA,j}_{2,0}]^L \tag{2.28}$$

that now contains all known quantities. Furthermore from Tab. 2.1 we may notice that only the components with $m = 0$ and $m = \pm 2$ are different from zero and thus all the relevant terms reduce to:

$$\begin{aligned} \mathscr{C}^{CSA} &= -\gamma_j \\ [A^{CSA,j}_{2,0}]^P &= \sqrt{\frac{3}{2}}(\delta_{zz} - \delta^j_{iso}) \\ [A^{CSA,j}_{2,\pm 2}]^P &= \frac{\eta^j}{2}(\delta_{zz} - \delta^j_{iso}) \\ [\mathscr{T}^{CSA,j}_{2,0}]^L &= \sqrt{\frac{2}{3}} \mathbf{I}_{jz} B_0 \end{aligned} \tag{2.29}$$

2.4.5 *Indirect Spin-Spin Coupling Interaction*

The indirect spin-spin coupling interaction represents the interaction between nuclear spins but mediated by electrons. The Hamiltonian for such an interaction is written introducing the tensor **J** as:

$$H_J = 2\pi \sum_{j<k} \mathbf{I}_j \cdot \mathbf{J}_{jk} \cdot \mathbf{I}_k \tag{2.30}$$

As done for the shielding tensor, it is possible to decompose the Cartesian **J** tensor into its irreducible spherical components of rank l=0,1,2. As above, the first rank tensor component is often neglected. The 0-th rank stands for the *isotropic J coupling constant* (or *scalar J coupling*) while the second rank one stands for the *anisotropy of J coupling*. The hamiltonian in the irreducible spherical representation becomes:

$$H_J = 2\pi \sum_{j<k} J_{jk} \mathbf{I}_j \mathbf{I}_k + 2\pi \sum_{j<k} \mathbf{I}_j A_J^{(2)} \mathbf{I}_k \tag{2.31}$$

with $A_J^{(2)}$ the second rank spherical component of the tensor **J**. In this form it is easy to recognize the space and spin part as:

$$H_J = \mathscr{C}^J \sum_{j<k} \left([A_{0,0}^{J,jk}]^L [\mathscr{T}_{0,0}^{J,jk}]^L + [A_{2,0}^{Jan,jk}]^L [\mathscr{T}_{2,0}^{Jan,jk}]^L \right) \tag{2.32}$$

We can now use Eqn. 2.15 for the isotropic part and Eqn. 2.5 for the anisotropic one to have:

$$H_J = \mathscr{C}^J \sum_{j<k} \left([A_{0,0}^{J,jk}]^P [\mathscr{T}_{0,0}^{J,jk}]^L + \sum_{m=-2}^{2} [A_{2,m}^{Jan,jk}]^P D_{m,0}^2(\Omega_{PL}) [\mathscr{T}_{2,0}^{Jan,jk}]^L \right) \tag{2.33}$$

All the occurring quantities that are not equal to zero are known and reported in Tab. 2.1, i.e.:

$$\begin{aligned}
\mathscr{C}^J &= 2\pi \\
[A_{0,0}^{J,jk}]^P &= -\sqrt{3} J_{jk} \\
[A_{2,0}^{Jan,jk}]^P &= \sqrt{6} J_{jk}^{an} \\
[\mathscr{T}_{0,0}^{J,jk}]^L &= -\frac{1}{\sqrt{3}} \mathbf{I}_j \mathbf{I}_k = -\frac{1}{\sqrt{3}} (\mathbf{I}_{jz} \mathbf{I}_{kz} + \frac{1}{2} (\mathbf{I}_j^+ \mathbf{I}_k^- + \mathbf{I}_j^- \mathbf{I}_k^+)) \\
[\mathscr{T}_{2,0}^{Jan,jk}]^L &= \frac{1}{\sqrt{6}} (3\mathbf{I}_{jz} \mathbf{I}_{kz} - \mathbf{I}_j \mathbf{I}_k) = \frac{2}{\sqrt{6}} (\mathbf{I}_{jz} \mathbf{I}_{kz} - \frac{1}{4} (\mathbf{I}_j^+ \mathbf{I}_k^- + \mathbf{I}_j^- \mathbf{I}_k^+))
\end{aligned} \tag{2.34}$$

2.4.6 Direct Spin-Spin Coupling Interaction

Nuclear spins can interact in a direct way through space. This interaction, the most important in the context of this thesis, is referred as *dipolar direct spin-spin coupling* or just as *dipolar coupling*. The dipolar interaction Hamiltonian is written by introducing the Cartesian tensor, $\mathbf{D}_{jk}$ as:

$$H_{DD} = \sum_{j<k} \mathbf{I}_j \cdot \mathbf{D}_{jk} \cdot \mathbf{I}_k \tag{2.35}$$

The dipolar tensor is traceless and therefore its irreducible spherical component of 0-th rank is null. The tensor is also symmetric and so the first rank component is also null. The Hamiltonian can be then written as:

$$H_{DD} = \sum_{j<k} b_{jk}(3\mathbf{I}_{jz}\mathbf{I}_{kz} - \mathbf{I}_j\mathbf{I}_k) \tag{2.36}$$

or, explicitly pointing out the spin and the space part, as :

$$H_{DD} = \mathscr{C}^{DD} \sum_{j<k} [A_{2,0}^{DD,jk}]^L [\mathscr{T}_{2,0}^{DD,jk}]^L \tag{2.37}$$

Again making use of Eqn. 2.5 we can rewrite it as:

$$H_{DD} = \mathscr{C}^{DD} \sum_{j<k} \sum_{m=-2}^{2} [A_{2,m}^{DD,jk}]^P D_{m,0}^2(\Omega_{PL}) [\mathscr{T}_{2,0}^{DD,jk}]^L \tag{2.38}$$

so that all the quantities are now known (see Tab. 2.1):

$$\begin{aligned} \mathscr{C}^{DD} &= 1 \\ [A_{2,0}^{DD,jk}]^P &= \sqrt{6} b_{jk} \\ [\mathscr{T}_{2,0}^{DD,jk}]^L &= \frac{1}{\sqrt{6}}(3\mathbf{I}_{jz}\mathbf{I}_{kz} - \mathbf{I}_j\mathbf{I}_k) \end{aligned} \tag{2.39}$$

Note that the form of the dipolar Hamiltonian does coincide with the form of the anisotropic part of the indirect coupling interactions. It is, therefore, difficult to distinguish, experimentally, the two quantities.

2.5 The Complete Internal Hamiltonian within HFA

Within the high-field approximation of Sec. 2.2 the complete form of the internal part of the NMR spin Hamiltonian for a system of N spins with I=1/2 is:

$$\begin{aligned} H_{int}(t) \cong & \sum_{j}^{N} \omega_0^j (1+\delta_{ZZ}^j) \mathbf{I}_{jz} + \sum_{j}^{N} \omega_0^j (\delta_{zz} - \delta_{iso}^j) \mathbf{I}_{jz} \\ & + 2\pi \sum_{j<k}^{N} J_{jk} \mathbf{I}_j \cdot \mathbf{I}_k + \sum_{j<k}^{N} b_{jk} (3\mathbf{I}_{jz}\mathbf{I}_{kz} - \mathbf{I}_j \cdot \mathbf{I}_k) \end{aligned} \tag{2.40}$$

where the first sum on the left hand side represents the Zeeman and the isotropic chemical shift parts combined together. The second sum represents the chemical shift anisotropy; the following one is the isotropic indirect spin-spin coupling (its anisotropic part is usually neglected or appended to the dipolar interaction). Finally, the last sum represents the direct dipolar coupling part.

3. SOLID STATE NMR TECHNIQUES FOR THE STUDY OF RHODOPSIN

3.1 Symmetry-based Rotor-synchronized Selective Recoupling

Symmetry bases recoupling sequences [8, 87] couple together the rotation of the spins achieved through *rf* pulses and the mechanical rotation of the sample achieved by MAS. Furthermore, the spin rotation is done in synchronization with the mechanical rotation as will be clear in a while.

3.1.1 The Spin Hamiltonian under MAS and rf Irradiation

We have already explored the effect of the sample spinning in Eqn. 2.7 where, once again, we have:

$$\begin{aligned} \alpha_{RL} &= \alpha_{RL}^{0} - \omega_r t \\ \beta_{RL} &= \beta_{mag} = arctan(\sqrt{2}) \end{aligned} \tag{3.1}$$

therefore, our staring point is:

$$H_{int}(t) = \sum_{\Lambda} C^{\Lambda} \sum_{l,\lambda} \sum_{m} [A_{l,m}^{\Lambda}]^{R} e^{-im(\alpha_{RL}^{0} - \omega_r t)} d_{m,0}^{l}(\beta_{mag}) [T_{\lambda,0}^{\Lambda}]^{L} \tag{3.2}$$

that, we recall for the last time, is valid within the high field approximation. The next step is to add the rotation of spins in the spin space through *rf* pulses, i.e. to write out explicitly the *rf* part of the total Hamiltonian in Eqn. 2.1. This can be done in a very general way since a series of *rf* pulses give rise to a rotation in the spin space that can be described by the propagator:

$$U_{rf}(t,t^{0}) = e^{-i\alpha_{rf}(t)\mathbf{I}_z} e^{-i\beta_{rf}(t)\mathbf{I}_y} e^{-i\gamma_{rf}(t)\mathbf{I}_z} \tag{3.3}$$

found integrating the following differential equation

$$\frac{d}{dt} U_{rf}(t,t^{0}) = -iH_{rf}(t) U_{rf}(t,t^{0}) \tag{3.4}$$

under the boundary condition:

$$U_{rf}(t^0, t^0) = \mathbf{1} \tag{3.5}$$

Here the Hamiltonian $H_{rf}(t)$ is the same as in Eqn. 2.1 and $\Omega_{rf} = \alpha_{rf}(t), \beta_{rf}(t), \gamma_{rf}(t)$ is the set of Euler angles that describes the rotation of the spins imposed by the Hamiltonian $H_{rf}(t)$. Note that, in general, there is not a simple relationship between these three Euler angles and the pulse angles and phases in the pulse sequences. However, the propagator in Eqn. 3.3 can be written using the Euler angles as:

$$\widehat{U_{rf}}(t, t^0) \rightarrow \widehat{\mathbf{R}}(\Omega_{rf}(t)) = \widehat{\mathbf{R_z}}(\alpha_{rf}(t))\widehat{\mathbf{R_y}}(\beta_{rf}(t))\widehat{\mathbf{R_z}}(\gamma_{rf}(t)) \tag{3.6}$$

with $\widehat{\mathbf{R_n}}(\theta) = e^{-i\theta\widehat{\mathbf{I}_n}}$. This rotation superoperator acts on any spherical tensor operator in the usual way, i.e. imposing a rotation described by Wigner matrices as:

$$\widehat{\mathbf{R}}(\Omega_{rf}(t))T_{l,m} = \sum_{\mu=-l}^{l} T_{l,\mu} D^{l}_{\mu m}(\alpha_{rf}(t), \beta_{rf}(t), \gamma_{rf}(t)) \tag{3.7}$$

and, for the inverse rotation given by $\widehat{\mathbf{R}^{-1}}(\Omega_{rf}(t))$:

$$\widehat{\mathbf{R}^{-1}}(\Omega_{rf}(t))T_{l,m} = \sum_{\mu=-l}^{l} T_{l,\mu} D^{l}_{\mu m}(-\gamma_{rf}(t), -\beta_{rf}(t), -\alpha_{rf}(t)) \tag{3.8}$$

These equations are very useful since will be soon used to write the total Hamiltonian in the interaction frame of $H_{rf}(t)$, here indicated as $\widetilde{H}$(t) . To do so, in fact, we need to write:

$$\widetilde{H}(t) = \widehat{\mathbf{R}^{-1}}(\Omega_{rf}(t))H(t) - H_{rf}(t) = \widehat{\mathbf{R}^{-1}}(\Omega_{rf}(t))H_{int}(t) \tag{3.9}$$

Using Eqn. 3.2 for the explicit form of $H_{int}(t)$ under MAS we have:

$$\widetilde{H}(t) = \sum_{\Lambda} C^{\Lambda} \sum_{l,\lambda} \sum_{m} [A^{\Lambda}_{l,m}]^{R} e^{-im(\alpha^{0}_{RL} - \omega_r t)} d^{l}_{m,0}(\beta_{mag}) \sum_{\mu} [T^{\Lambda}_{\lambda,\mu}]^{L} e^{i\mu\gamma_{rf}(t)} d^{\lambda}_{\mu,0}(-\beta_{rf}(t)) \tag{3.10}$$

This Hamiltonian is the basis for all the rotor-syncronized symmetry-based recoupling techniques [8]. It can be written in a more useful and compact form as:

$$\widetilde{H}(t) = \sum_{\Lambda} C^{\Lambda} \sum_{l,m,\lambda,\mu} H^{\Lambda}_{l,m,\lambda,\mu} \tag{3.11}$$

with

$$H^{\Lambda}_{l,m,\lambda,\mu} = d^{l}_{m,0}(\beta_{mag})e^{i\mu\gamma_{rf}(t)}d^{\lambda}_{\mu,0}(-\beta_{rf}(t))e^{-im(\alpha^{0}_{RL}-\omega_{r}t)}[A^{\Lambda}_{l,m}]^{R}[T^{\Lambda}_{\lambda,\mu}]^{L} \tag{3.12}$$

3.1.2 The Average Hamiltonian

The Hamiltonian above describes what happens during a rotor-syncronized pulse sequence i.e. a sequence performed under MAS conditions and where the *rf* pulses are synchronized with the sample rotation. Suppose for example that we start such a pulse sequence at the time t^0 and we want to calculate what happens at the time $t = t^0 + \tau$ and that the pulse sequence is periodic with period $T = n\tau_r$ i.e. an integer multiple of the rotor period $\tau_r = 2\pi/\omega_r$. Using the Average Hamiltonian Theory [88], the propagator for the pulse sequence between the time points t^0 and $t^0 + \tau$ can be written as:

$$U(t^0+\tau,t^0) = U_{rf}(t^0+\tau,t^0)e^{-i\overline{H}(t^0)\tau} \tag{3.13}$$

with $U_{rf}(t^0+\tau,t^0)$ given in Eqn. 3.3 and $\overline{H}(t^0)$ being the “effective Hamiltonian”. This latter can be approximated using the so called Magnus expansion [89] as:

$$\overline{H}(t^0) \approx \overline{H}^{(1)}(t^0) + \overline{H}^{(2)}(t^0) + ... \tag{3.14}$$

with the *average Hamiltonian* given by:

$$\overline{H}^{(1)}(t^0) = T^{-1}\int_{t^0}^{t^0+T} H_{int}(t)\, dt \tag{3.15}$$

and its *second-order correction* given by

$$\overline{H}^{(2)}(t^0) = (2iT)^{-1}\int_{t^0}^{t^0+T} dt_2 \int_{t^0}^{t_2} [H_{int}(t_2), H_{int}(t_1)]\, dt_1 \tag{3.16}$$

and so on. This technique is of great use as it simplifies the calculation of the evolution of spin states under a rotor-syncronized pulse sequence. Furthermore, this approximation can be used in order to calculate the symmetry rule for selective recoupling of spin-interaction in symmetry-based rotor-syncronized selective recoupling techniques.

3.1.3 Rotor-syncronized symmetry-based pulse sequences

The sample rotation can be synchronized with the spin trajectory (modified through rf pulses) to generate an average Hamiltonian that selectively contains the desired terms (i.e. the desidered combination of the four indices: l, m, λ, μ). The idea is to set up periodic symmetry relationship (here the name symmetry-based) between the mechanical rotation and the rf irradiation. Given two arbitrary time points, separated by the interval $\tau = n\tau_r/N$ (n and N are integers and $\tau_r = |2\pi/\omega_r|$ is the rotor period), there is a periodic relationship involving the spatial Euler angle that connects the R frame with the L frame, i.e.:

$$\begin{aligned} \alpha_{RL}(t + \frac{n\tau_r}{N}) &= \alpha_{RL}(t) - \frac{2\pi n}{N} \\ \beta_{RL}(t + \frac{n\tau_r}{N}) &= \beta_{RL}(t) \end{aligned} \tag{3.17}$$

A similar relationship can be found also in the case of Ω_{rf}. To work this out we will need to introduce the precise nature of the pulse sequences we would like to discuss. There are two main symmetry classes that group together an infinite number of symmetry-based rotor-syncronized pulse sequences. These are usually indicated as CN_n^ν and RN_n^ν. N is called the symmetry number, n the space number and ν the winding number. The general idea under these schemes is to synchronize N rf pulse events with n rotational periods of the sample. At the same time the rf phase is shifted as a function of ν.

CN_n^ν *type*

A CN_n^ν sequence consists of a series of *rf* cycles (i.e. the spins undergo a full 360° rotation in the spin space - or an integer multiple of it) fitted in n rotor period ($\tau_r = 2\pi/\omega_r$) with the *rf* phase of each cycle shifted by $2\pi\nu/N$ radians with respect to the previous one. This scheme is illustrated in Fig. 3.1.

This particular pulse scheme imposes the following rf-Euler angle symmetry:

$$\begin{aligned} \beta_{rf}(t + \frac{n\tau_r}{N}) &= \beta_{rf} \\ \gamma_{rf}(t + \frac{n\tau_r}{N}) &= \gamma_{rf}(t) - \frac{2\pi\nu q}{N} \end{aligned} \tag{3.18}$$

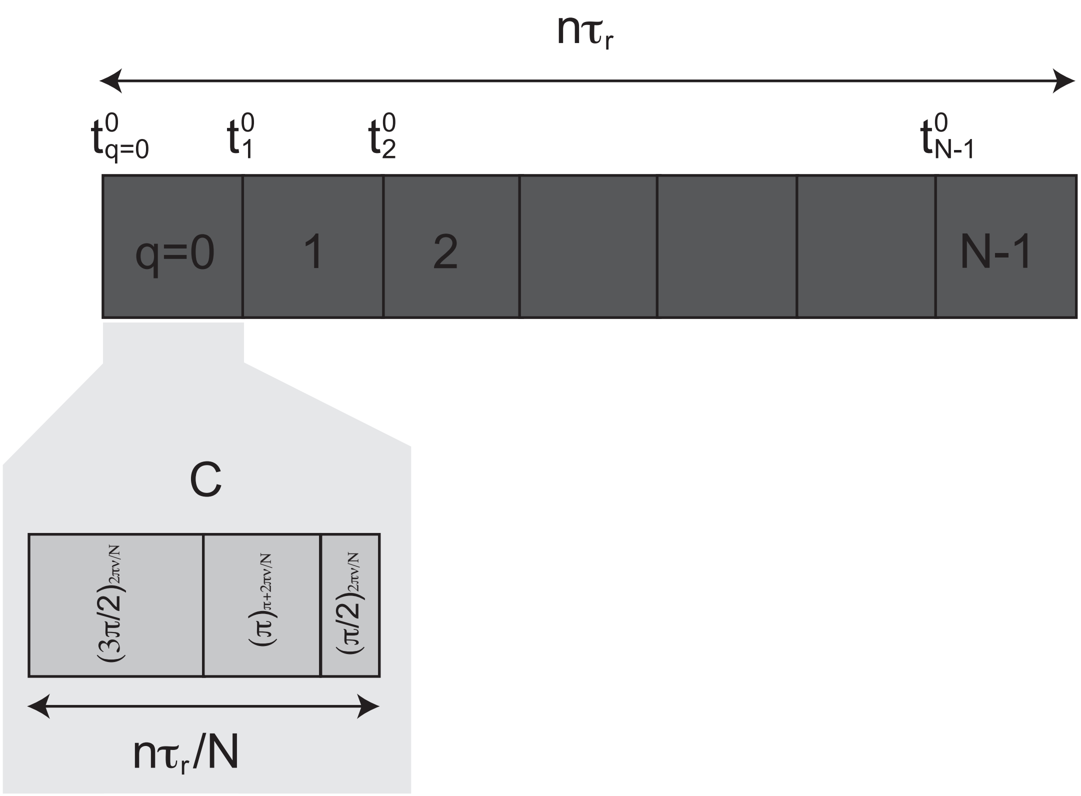

Fig. 3.1: Schematic representation of a CN_n^ν rotor-synchronized symmetry-based pulse sequence. The POST [9] basic element ($270_0 180_{180} 90_0$) has been chosen as an example.

RN_n^ν *type*

A RN_n^ν sequence consists of a series of N/2 pairs (R, R') of *rf* elements fitted in n rotor periods. The *rf* elements addressed as R, implements a 180° rotation of the resonant spins with an overall phase shift ϕ. Those addressed as R' are the same as R but with the sign of all the phases changed. The phase ϕ is equal to $\pi\nu/N$ radians. The phase is therefore alternated between $\pi\nu/N$ and $-\pi\nu/N$. This scheme is illustrated in Fig. 3.2.

This particular pulse scheme imposes the following rf-Euler angle symmetry:

$$\begin{aligned}\beta_{rf}(t+\frac{n\tau_r}{N}) &= \beta_{rf} \pm \pi q \\ \gamma_{rf}(t+\frac{n\tau_r}{N}) &= \gamma_{rf}(t) - \frac{2\pi\nu q}{N}\end{aligned} \tag{3.19}$$

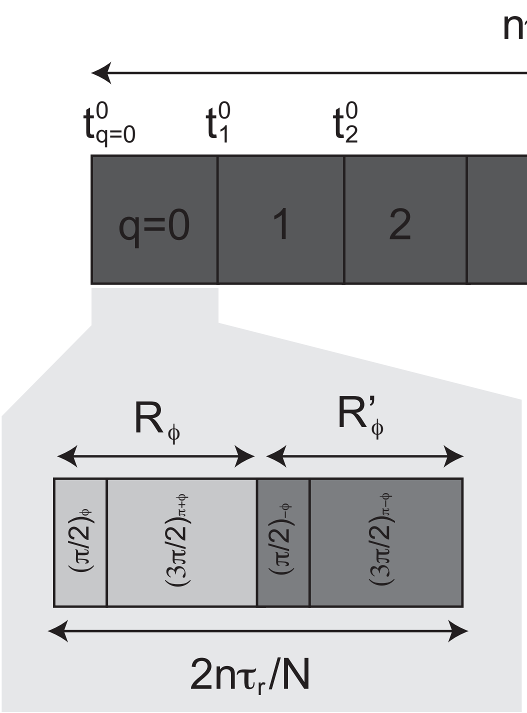

Fig. 3.2: Schematic representation of a RN_n^ν rotor-synchronized symmetry-based pulse sequence. The basic element $90_\phi 270_{\pi+\phi}$, later used for all the rhodopsin experiments, has been chosen as an example.

3.1.4 Selection Rules for Symmetry-based Rotor-syncronized Sequences

The Hamiltonian valid under MAS and in presence of *rf* irradiation for a given interaction Λ is given in Eqn. 3.11. The average Hamiltonian is therefore given by:

$$\overline{H}^{(1)}(t^0) = \sum_{l,m,\lambda,\mu} \overline{H}^{(1)}_{l,m,\lambda,\mu}(t^0) \tag{3.20}$$

with every component given by:

$$\overline{H}^{(1)}_{l,m,\lambda,\mu}(t^0) = T^{-1} \int_{t^0}^{t^0+T} H_{l,m,\lambda,\mu}(t)\, dt \tag{3.21}$$

The first-order selection rule for selective recoupling governing symmetry-based rotor-syncronized pulse sequences is obtained imposing:

$$\overline{H}^{(1)}_{l,m,\lambda,\mu} = 0 \tag{3.22}$$

and can be analytically calculated. The derivation of these selection rules is presented in Ref. [90] and in Ref. [87] for the case of the RN_n^ν sequences. In the following, only the results will be presented.

Selection Rules for CN_n^ν sequences

In the case of a CN_n^ν sequence, it has been found [90] that:

$$\overline{H}^{(1)}_{l,m,\lambda,\mu} = 0 \quad \text{if } mn - \mu\nu \neq NZ \tag{3.23}$$

with Z any integer including zero.

Selection Rules for RN_n^ν sequences

In the case of a RN_n^ν sequence, it has been found [87] that:

$$\overline{H}^{(1)}_{l,m,\lambda,\mu} = 0 \quad \text{if } mn - \mu\nu \neq \frac{N}{2} Z_\lambda \tag{3.24}$$

with Z_λ an integer with the same parity of λ.

3.1.5 Allowed Terms and Their Magnitude

The selection rules provide information on which terms are symmetry-forbidden (i.e. not recoupled). However, they provide no information on the magnitude of the symmetry-allowed terms. A first order allowed term has, for a given interaction, the general form:

$$\overline{H}^{(1)}_{l,m,\lambda,\mu}(t^0) = k_{l,m,\lambda,\mu} e^{-im(\alpha^0_{RL} - \omega_r t^0)} [A_{l,m}]^R [T_{\lambda,\mu}]^L \tag{3.25}$$

where the quantity

$$k_{l,m,\lambda,\mu} = d^l_{m,0}(\beta_{mag}) T^{-1} \int_0^T d^\lambda_{\mu,0}(-\beta_{rf}(t)) e^{i(\mu\gamma_{rf}(t) + m\omega_r t)} \tag{3.26}$$

is called the *scaling factor*. This shows that at the same time as a given symmetry-based sequence suppresses some terms in the Hamiltonian, the other allowed terms are recoupled but their magnitude is reduced by a scaling factor. Note that the scaling factor magnitude depends on the way the C or R pulse scheme is implemented. These schemes are referred as the *basic element*. Clearly there are an infinite number of way to perform a 360° or a 180° rotation of the spins starting from a single 2π or π pulse to any other possible combination of pulses of any duration and phase. It is therefore essential to underline that the scaling factor (i.e. how much of the interaction is recoupled) depends on the exact choice of rf-pulses that constitute the basic element.

3.2 Analysis of $R20_2^9$ pulse sequence

The $R20_2^9$ pulse sequence has been used as a building block in more sophisticated pulse sequences used in this thesis to measure chemical shifts, distances and torsional angles on rhodopsin and its photointermediates. These sequences will be discussed in the next two sections. Here, a detailed analysis of the $R20_2^9$ recoupling scheme is done in terms of allowed terms and scaling factors. According to the notation in Sec. 3.1.3 the symmetry numbers are:

$$\begin{aligned} N &= 20 \\ n &= 2 \\ \nu &= 9 \end{aligned} \tag{3.27}$$

therefore, $N/2 = 20/2 = 10$ basic elements, R (each one performing an overall rotation of 180° of the resonant spins), are fitted in $n = 2$ rotor period (i.e. within $2\tau_r = 4\pi/\omega_r$ seconds). The overall phase of the R basic element is $\phi = \nu\pi/N = 9\pi/20$.

The allowed terms in the Hamiltonian can be calculated using the selection rules in Sec. 3.1.4. This has been done using the routines implemented by M. H. Levitt and A. Brinkmann into Mathematica (mPackages [91]) and results are reported in Tab. 3.1. The $R20_2^9$, thus, reintroduces the isotropic indirect spin-spin coupling Hamiltonian plus the double quantum $\lambda = 2$ direct dipolar coupling Hamiltonian. Both the isotropic chemical shift Hamiltonian (isoCS) and its anisotropic part (CSA) are not allowed. Scaling factors can be calculated using Eqn. 3.26. However the precise nature of $\beta_{rf}(t)$ and $\gamma_{rf}(t)$ must be known, i.e. the exact basic element has to be known. For the basic element $90_\phi 270_{\pi+\phi}$ (see Fig. 3.2) used in all the experiments done on rhodopsin and its photointermediate (see the following), calculations (using mPackages) give the values reported in the last column of Tab. 3.1. This means that while the scalar coupling Hamiltonian is completely recoupled, the

Tab. 3.1: Number and rotational signatures of the allowed term for the $R20_2^9$ sequence. The scaling factors ($k_{l,m,\lambda,\mu}$) refer to the basic element $90_\phi 270_{\pi+\phi}$.

Λ	no. of allowed terms	$\overline{H}^{(1)}_{l,m,\lambda,\mu}$ recoupled	$k_{l,m,\lambda,\mu}$
isoCS	0	-	-
J	1	$\overline{H}^{(1)}_{0,0,0,0}$	1.0
CSA	0	-	-
DD	2	$\overline{H}^{(1)}_{2,\mp 1,2,\pm 2}$	$\pm$ 0.174

double-quantum part of the dipolar Hamiltonian is recoupled only to the extent of 0.174.

3.3 DQF-DR: Chemical Shifts and Distance Measurements

Chemical shift data and distance measurements on rhodospin and its photointermediate can be performed in the solid state using a symmetry-based recoupling technique known as Double-Quantum-filtered dipolar recoupling (DQF-DR) [8]. With such a recoupling sequence it is possible to selectively recouple the double-quantum component of the dipolar interaction (to the first order in the average Hamiltonian sense) in a spinning solid sample. This means that only spins for which it is possible to write a double quantum dipolar hamiltonian will contribute to the final NMR signal.

The pulse sequence for this symmetry is reported in Fig. 3.3. The sequence is applied under MAS conditions so that all the anisotropic interactions (i.e. CSA and DD in our case) are removed. Due to the presence of the $R20_2^9$ block, however, the DD term is recoupled and starts to build-up during the time τ_{exc} (Sec. 3.2). A double quantum filter (2Q in Fig. 3.3 - achieved by phase cycling) is then applied in order to select only double quantum terms in the dipolar Hamiltonian. Finally, the same recoupling sequence is applied for a time τ_{rec} in order to obtain the recoupled signal. The chemical shift of the two coupled carbon labels (strategically placed in the carbon chain of a retinylidene-rhodopsin isotopomer) are then easily measured as the only one occurring in the FT spectrum obtained for a selected value of τ_{exc} and τ_{rec}. Moreover, it is possible to optimize the signal intensity by running a series of experiments varying either τ_{exc} or τ_{rec} or both of them at the same time.

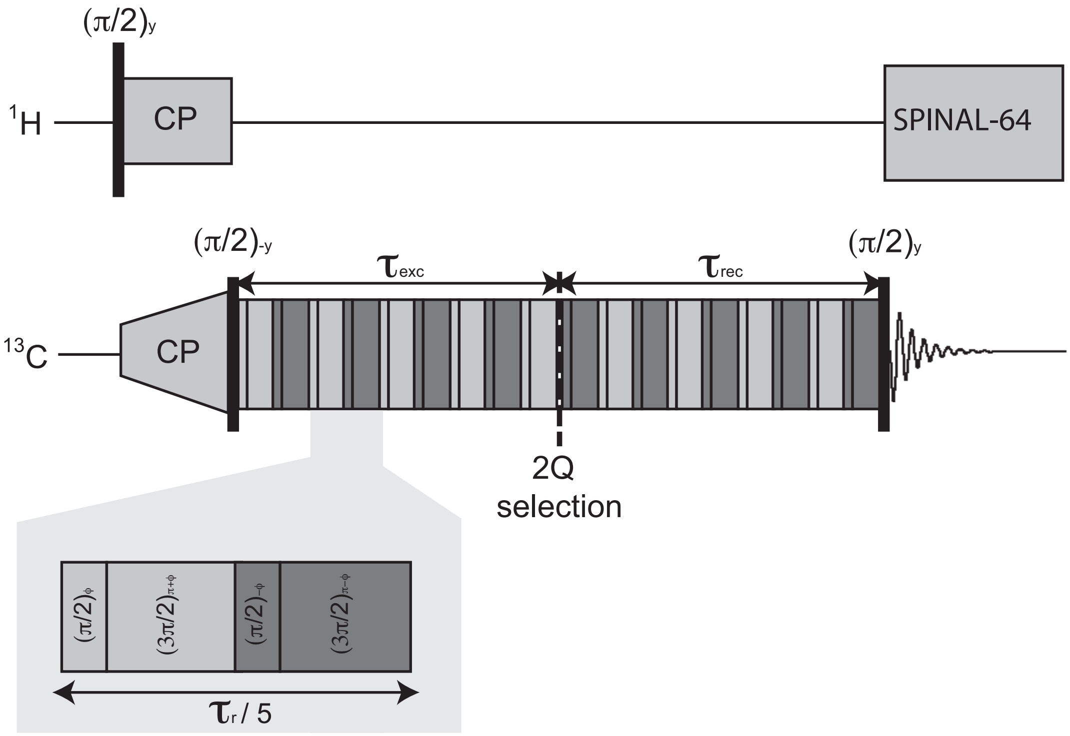

Fig. 3.3: Pulse sequence for double quantum filtered dipolar recoupling.

In particular, we refer to the *symmetric procedure* when τ_{exc} is kept equal to τ_{rec} and both are then varied at the same time; we refer to the *asymmetric procedure* when τ_{exc} is varied but τ_{rec} is kept fixed (or viceversa). The series of spectra is then collected and their intensity plotted versus the τ_{exc} (or τ_{rec}) is called a *build-up* curve. Moreover C-C distances can be obtained by fitting the build-up curve. It is possible to show [92], using theoretical argumentation, that the build-up curve comes from the powder averaging of a signal intensity of the form:

$$s(\tau_{exc}, \tau_{rec}) = \left\langle \sin\left(|\omega_{jk}\ \tau_{exc}|\right) \sin\left(|\omega_{jk}\ \tau_{rec}|\right) \right\rangle \tag{3.28}$$

were ω_{jk} is the double quantum dipolar modulation frequency (which contains the distance information) and the braket denotes a powder average over all the possible orientations of crystallites in the sample.

Moreover, a theoretical study done in our laboratory (Paper 1) showed that Eqn. 3.28 has an analytical solution that , for the symmetric procedure, is:

$$s(\tau, \tau) = \frac{1}{2} - \frac{1}{x\sqrt{8}}(sin(2\theta)F_s(x\sqrt{2}) + cos(2\theta)F_c(x\sqrt{2})) \tag{3.29}$$

with $\tau_{exc} = \tau_{rec} = \tau$ and where $F_c(x)$ is the Fresnel cosine integral given by:

$$F_c(x) = \int_0^x cos(\frac{\pi y^2}{2})dy \tag{3.30}$$

while $F_s(x)$ is the related Fresnel sine integral given by:

$$F_s(x) = \int_0^x sin(\frac{\pi y^2}{2})dy \tag{3.31}$$

and

$$\begin{aligned} x &= \{2\theta/\pi\}^{1/2} \\ \theta &= \frac{3}{2}|k_{2m22}|b_{jk}\tau \end{aligned} \tag{3.32}$$

For the asymmetric case:

$$\begin{aligned} s(\tau_{exc}, \tau_{rec}) = & \frac{1}{2x_\Delta}(sin(\theta_\Delta)F_s(x_\Delta) + cos(\theta_\Delta)F_c(x_\Delta)) \\ & - \frac{1}{2x_\Sigma}(sin(\theta_\Sigma)F_s(x_\Sigma) + cos(\theta_\Sigma)F_c(x_\Sigma)) \end{aligned} \tag{3.33}$$

with

$$\begin{aligned} \theta_\Delta &= \theta_{exc} - \theta_{rec} \\ \theta_\Sigma &= \theta_{exc} - \theta_{rec} \\ x_\Delta &= \{2\theta_\Delta/\pi\}^{1/2} \\ x_\Sigma &= \{2\theta_\Sigma/\pi\}^{1/2} \\ \theta_{exc} &= \frac{3}{2}|k_{2m22}|b_{jk}\tau_{exc} \\ \theta_{rec} &= \frac{3}{2}|k_{2m22}|b_{jk}\tau_{rec} \end{aligned} \tag{3.34}$$

$|k_{2m22}|$ is the scaling factor for the dipolar interaction that depends on the symmetry and the basic element chosen while the distance information is contained in the magnetic dipole-dipole coupling constant b_{jk} (see Tab. 2.1).

3.4 DQ-HLF: Torsional Angle Measurements

The measurements of torsional angle in rhodopsin samples have been carried out using the Double-Quantum-Heteronuclear Local Field (DQ-HLF) experiment presented in Ref. [93] and [94]. Given the molecular fragment ABCD, the torsional angle ϕ is defined as the positive angle by which the plane containing the CD bond is rotated away from the plane containing the BA bond in the positive sense, when viewing along the BC bond (see Fig. 3.4). The pulse sequence used in these experiment is reported in Fig. 3.5. It can can be divided into the following steps:

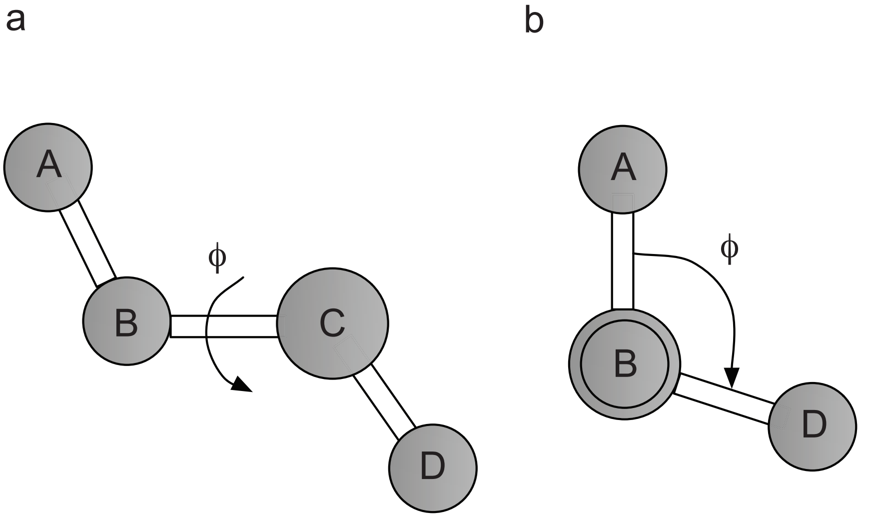

Fig. 3.4: a) Definition of torsional angle ϕ in the molecular fragment ABCD. b) view along the BC bond

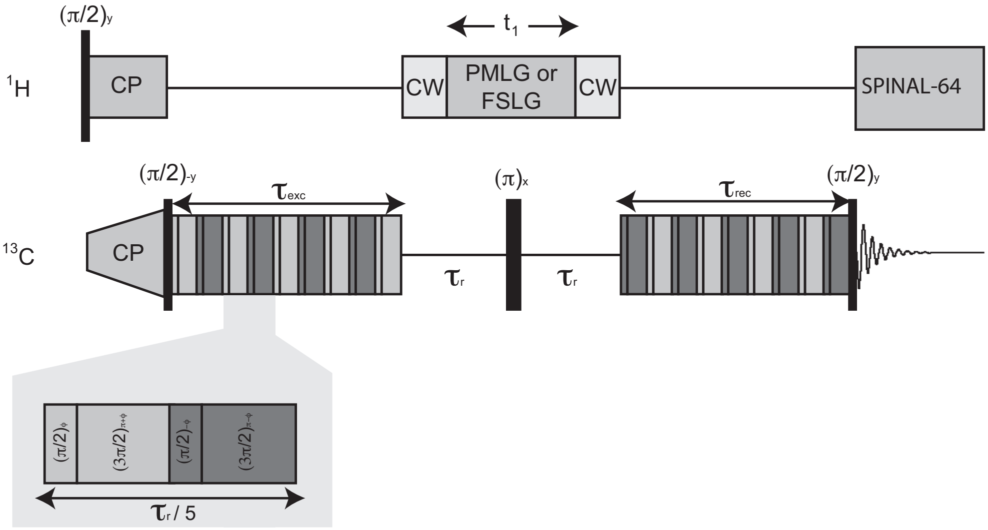

Fig. 3.5: DQ-HLF pulse sequence used for torsional angle measurements. Either Phase-Modulated Lee-Goldburg (PMLG) or Frequency Switched Lee-Goldburg (FSLG) has been used as homonuclear decoupling scheme during t_1.

1. create a double-quantum state involving the two ^{13}C sites using the DQ homonuclear dipolar recoupling technique in Sec. 3.3;

2. let the DQ coherence evolve in the presence of the heteronuclear CH couplings for a variable time interval t_1;
3. convert back the DQ coherence into observable signal.

For this application, $\tau_{exc} = \tau_{rec}$ are kept fixed to the value corresponding to the experimental maximum of DQ efficiency. During the DQ evolution period which last two rotor periods (2 τ_r), a homonuclear decoupling sequence is applied. Either Phase-Modulated Lee-Goldburg (PMLG) [95, 96] or Frequency Switched Lee-Goldburg (FSLG) [97] have been tested as the choice of the most convenient homonuclear decoupling sequence depends on the spectrometer capabilities in terms of switching phase or frequency with sufficient speed. In the middle of the evolution period a π-pulse is applied on the carbon channel in order to refocus the evolution of the double-quantum coherences under the isotropic chemical shifts of the carbon. Due to the change in the phases of the double-quantum coherences induced by the π-pulse, a reconversion sequence with opposite winding number ν has to be applied to reconvert the double-quantum coherences into longitudinal carbon magnetization. A series of spectra is finally acquired in which t_1 is varied between 0 and τ_r in steps whose length depends on the PMLG or FSLG pulse scheme. In particular, the interval t_1, occupied by the homonuclear decoupling sequence, is divided into two parts which are incremented in the directions shown in Fig. 3.5. During the period $\tau_r - t_1/2$ in which the DQ coherences are free to evolve but the homonuclear interactions on the proton channel are not selectively decoupled, a continuous wave (CW) decoupling scheme is applied instead in order to decouple any CH and HH interactions.

A detailed explanation of how the sequence works is quite complicated and can be found in Ref. [98]. However, an analytical expression of the signal as a function of the torsional angle was not found yet. Despite of this it is relatively easy to spot where this dependence comes in. To do so one need to analyze what happen during the DQ evolution under homonuclear decoupling i.e. during the interval t_1 in Fig. 3.5. The main idea is the selective reintroduction of the CH dipolar coupling interactions under decoupling of the HH ones. During the time interval t_1 a scaled heteronuclear dipolar CH Hamiltonian is present. Its analytical form can be worked out on the basis of what discussed in the previous chapter. Namely, we have:

$$\begin{aligned} H^{DD,CH} &= k_{2020}[A_{20}^{DD,CH}]^L[\mathscr{T}_{20}^{DD,CH}]^L \\ &= 2k_{2020}[A_{20}^{DD,CH}]^L \mathbf{I}_{Cz}\mathbf{I}_{Hz} \end{aligned} \tag{3.35}$$

where the non-z terms in the spin-tensors have been neglected on the basis of the secular approximation surely valid because of the heteronuclear nature of the coupling. As usual, Eqn. 2.5 is used in order to transform the space part from the L frame to a frame that helps us to reveal the features we want. In this case a double transformation in needed:

$$\begin{aligned} [A_{20}^{DD,CH}]^L &= \sum_m [A_{2m}^{DD,CH}]^M D_{m,0}^2(\Omega_{ML}) \\ &= \sum_{m,m'} [A_{2m'}^{DD,CH}]^P D_{m',m}^2(\Omega_{PM}) D_{m,0}^2(\Omega_{ML}) \end{aligned} \tag{3.36}$$

So that, according to Tab. 2.1:

$$\begin{aligned} H^{DD,CH} &= 2k_{2020} b_{CH} \sum_m D_{0,m}^2(\Omega_{PM}) D_{m,0}^2(\Omega_{ML}) \mathbf{I}_{Cz}\mathbf{I}_{Hz} \\ &= 2k_{2020} b_{CH} \sum_m d_{0,m}^2(\beta_{PM}) e^{-im\gamma_{PM}} D_{m,0}^2(\Omega_{ML}) \mathbf{I}_{Cz}\mathbf{I}_{Hz} \end{aligned} \tag{3.37}$$

The central quantity here is γ_{PM}, the angle between the z^P-axis of the principal axis frame for the CH dipolar interaction (i.e. the CH bond axis) and the z^M-axis of the molecular frame (see fig. 3.6). In fact, the difference $\gamma_{PM}(C_1H_1) - \gamma_{PM}(C_2H_2)$ equals the torsional angle ϕ. This demonstrates the dependence of the signal on the torsional angle. In the absence of an analytical equation, experimental results will be fitted to simulations in order to extract the torsional angle.

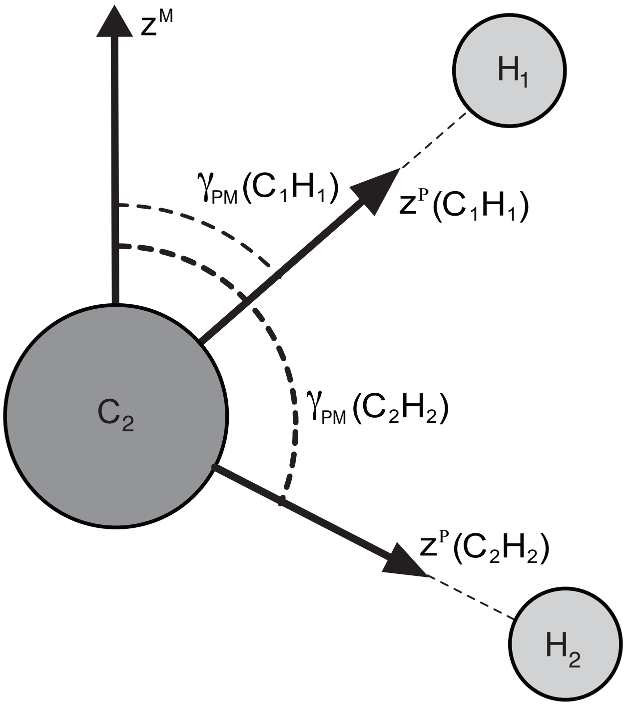

Fig. 3.6: Torsional angle of the fragment H-C=C-H and its relationship with the Euler angles γ_{PM}.

PART III: EXPERIMENTS

4. MATERIALS, EQUIPMENT AND PROCEDURES

The success of the experiments discussed in this thesis relied on the ability to perform Magic Angle Spinning (MAS) at stable and well controlled sample temperatures ranging from 230 K down to 125 K. This is due to the fact that rhodopsin photointermediates, the target molecules in this study, can be trapped only at selected and precise temperatures. At the same time, the photocycle can be triggered by illuminating the cold sample with a proper visible wavelength. Since these two tasks cannot be performed by any commercial probe a customized NMR probe has been used. This has been built in Levitt's group during the past years but set up and optimized during this work. This customization is of central importance as these tasks represent real technical challenges. On the issue of the sample temperature, for example, the frictional heating due to the spinning rotor and the warming caused by the bearing and drive air streams (typically near room temperature gases), produce a difference in temperature between the sample and the electronic temperature sensors (clearly mounted outside the rotor - at the end of the Variable Temperature (VT) stack in contact with the stator, in our equipment). The real sample temperature has therefore to be calibrated at the exact condition of the magic angle spinning experiments. Moreover, since the flow of cold gas used to cool the sample is directed straight to the center of the rotor, a gradient of temperature exists across the rotor length. This needs to be taken into account in the sense that the warmer part of the sample is kept at the right temperature. As will be described below, the sample temperature was calibrated, in this work, using the ^{207}Pb chemical shift of a lead nitrate sample [99] and the narrow proton resonance of the endohedral dihydrogen fullerene ($H_2@C_{60}$) as an independent chemical shift reference [100].

The second major issue is the optimisation of the light penetration into the sample for the in-situ irradiation of the rhodopsin chromophore that starts the photocycle. The penetration of light into rhodopsin samples is a complicated process since the photointermediate composition of the outer layers affects the penetration of light into the sample interior. Also, more than one species can be produced and this may result in losses of concentration (and therefore spectral quality) of the targeted photointermediate. The composition of photoisomers is a function of time, space, and photon wavelength distribution and, therefore, a simulation of the light penetration, the search of related physical quantities and the successive adaptation of the equipment were needed in order to achieve a successful result.

A detailed explanation of these technical challenges and the way they have been overcome is reported in this chapter after a description of the targeted samples.

4.1 Samples

As a general strategy to approach the study of rhodopsin with the purposes described in the introductory parts, a series of doubly ^{13}C-labelled retinals have been synthetized and incorporated into the protein opsin to form retinylidene-rhodopsin isotopomers. Retinylidene-photointermediates have been then produced by illumination of the respective retinylidene-rhodopsin compounds. The reason to have more than one isotopomer is clearly linked with the possibility to record, in this way, site-specific information. The chosen isotopomers were: [9,10-$^{13}C_2$]-, [11,12-$^{13}C_2$]-, [12,13 $^{13}C_2$]-, [14,15-$^{13}C_2$]-retinylidene-rhodopsin. Note that the choice assures a good region around the double bond C11=C12 (i.e. where the isomerization happens) to be investigated.

4.1.1 Isotopically-labelled Retinals

The serie of doubly ^{13}C-labelled retinals needed to produce the related retinylidene-species were prepared by organic synthesis as described in Ref. [101] and [102]. The labeled all-*trans*-retinals were isomerised to 11-*cis*-retinals by dissolving them in a solution of dry acetonitrile under controlled illumination conditions. The desired isomer was isolated and purified by high-performance liquid chromatography (HPLC) using a polar column and an apolar eluent. The structures of these compounds are shown in Fig. 4.1. The filled circles indicate the position of the ^{13}C labels. This part of the work has been carried out by co-workers in R. C. D. Brown's group at the University of Southampton.

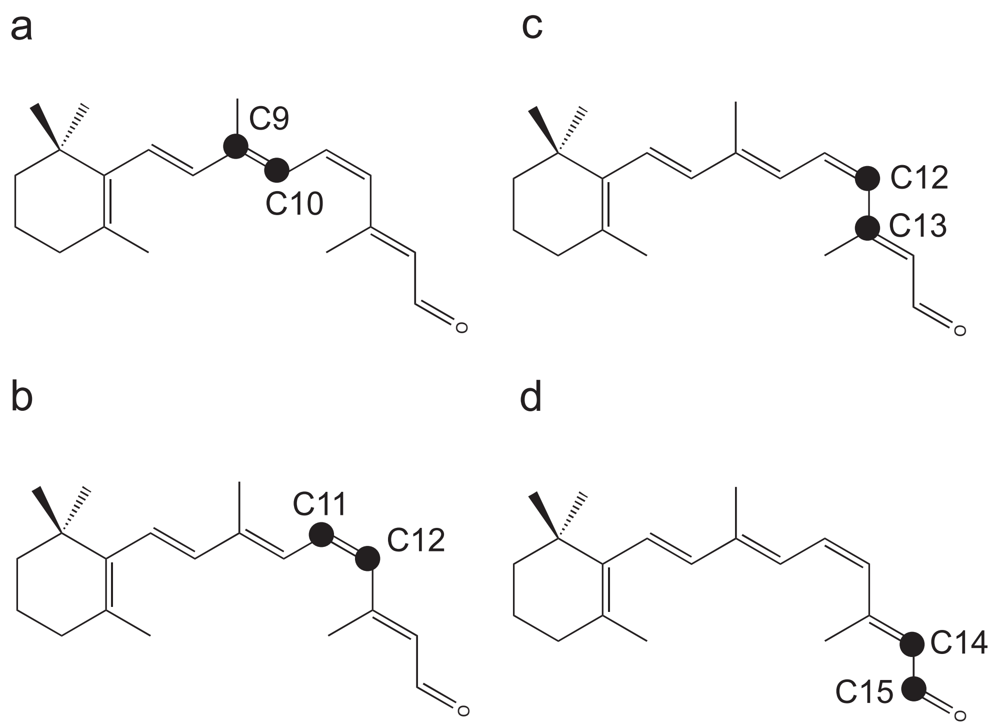

Fig. 4.1: Structure and labeling of retinals used in the synthesis of retinylidene-rhodopsin compounds.

4.1.2 Isotopically-labelled Rhodopsins

The doubly labeled retinylidene-rhodopsin samples used for the experiments were prepared by incorporating the labeled 11-*cis*-retinal into the protein opsin, isolated from fresh cattle eyes. Details of the methodology can be found in Ref. [103]. The insertion of the chromophore (11-*cis*-retinal) into the protein opsin was verified by optical measurements, due to the difference in optical absorbance between rhodopsin and 11-cis-retinal (respectively 498 nm and 380 nm in detergent solution). The w/w ratio protein to lipid was in the range 1:1 to 1:1.3 while the molar ratio protein to lipid was in the range 1:60 to 1:80. All the sample handling was carried out in a darkened room under dim red light. On storage, the samples were kept in light-tight vials in a nitrogen atmosphere at -80 °C. This is needed in order to minimize the light-induced isomerization, prevent water absorption and possible oxidation reactions of the sample. This part of the work was carried out by co-workers in W. DeGrip's group at the Radboud University Medical Centre, Nijmegen Centre for Molecular Life Sciences, Nijmegen, the Netherlands.

4.2 Technical Challenges

As briefly introduced above, there are a series of technical challenges to cope with when trapping and studying, by means of solid-state NMR, a photointermediate. These technical challenges are:

1. cool the sample at very low temperatures (< 125K)
2. keep temperature stable while spinning
3. irradiate the sample with light of the proper frequency to trigger the photocycle.

A 9.4 T Varian Infinity+ solid state NMR spectrometer was used in conjunction with other, in some cases custom-made, parts designed to allow the in-situ cooling and illumination of rhodopsin samples. These extra parts are essentially a custom-modified VT stack, an exchange Dewar and a purpose-built two channel solid state 4 mm probe. An overview of the experimental set up used in this thesis is given in Fig. 4.2.

The use and the purpose of each part of this set up is explained in the following few sections.

4.2.1 The Temperature Issue

It should be clear, at this point, that a precise control of the temperature is essential to trap rhodopsin phtointermediates. However, it must be also clear that this is one of the two key points that distinguishes this work from a previous attempt [61] where the temperature control was not carried out so rigorously. The central point of the temperature issue is the gap between the readout temperature and the real temperature of the sample due to a series of phenomena that must be kept under control. In fact, in an ordinary NMR cooling equipment the temperature inside the NMR rotor is a function of the cooling gas flow and temperature (usually slightly higher than 77 K - the liquid nitrogen temperature) and the bearing and drive gas flows and temperatures (typically about 293 K). The mixing of the three gas flows at quite different temperatures, causes a local (in the very proximity of the sample) difference in temperature between the one read by the digital thermometer, usually placed at the end of the VT stack and strongly affected by the temperature of the cooled nitrogen gas, and the one inside the sample which is perturbed (increased) by

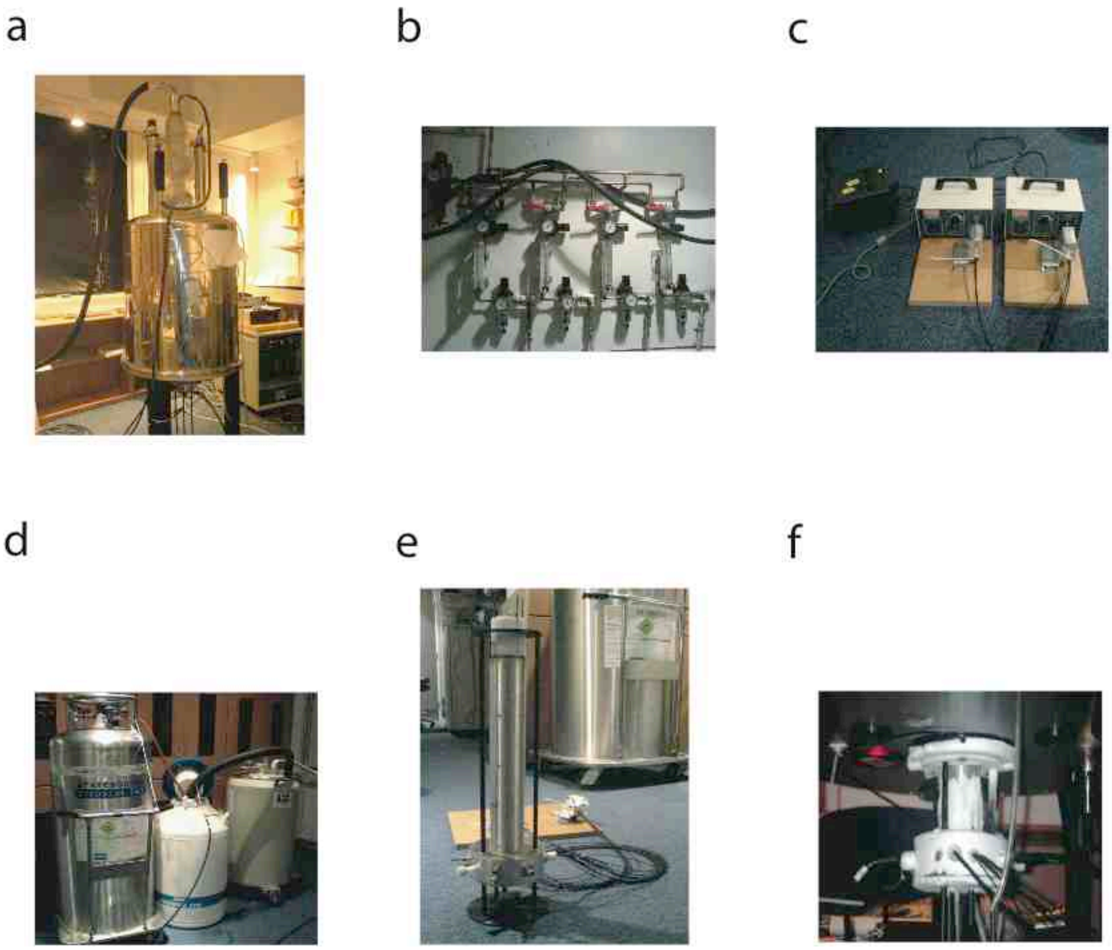

Fig. 4.2: A picture of the main pieces of the equipment used in this work: a) the varian 400 MHz infinity+ magnet; b) the gas lines for cooling, bearing and drive gases; c) the two lamps, filters, lenses and optical fibers used to illuminate the sample and trig the rhodopsin photocycle; d) the transport, precooler and exchange/cooler Dewars (left to right) used to cool the gas flows in b); e) the custom-build HX probe that allows in-situ cooling and illumination of solid 4 mm rotors (note the optical fibers that acts as pipelines for the light to reach the rotor); f) the probehead frozen at the operating temperature of 120 K during a real experiment.

the thermal mixing of the cool nitrogen gas coming out from the VT and the warmer spinning gases (drive and bearing) used to spin the sample itself. To minimize this effect, a standard Varian VT stack was modified such as that both bearing and drive gas flows are cooled, by thermal contact with the exhaust of the cooling gas flow, directly inside the VT stack itself (Fig. 4.3).

The hardware setup for the sample cooling and its calibration are discussed in the next two subsections.

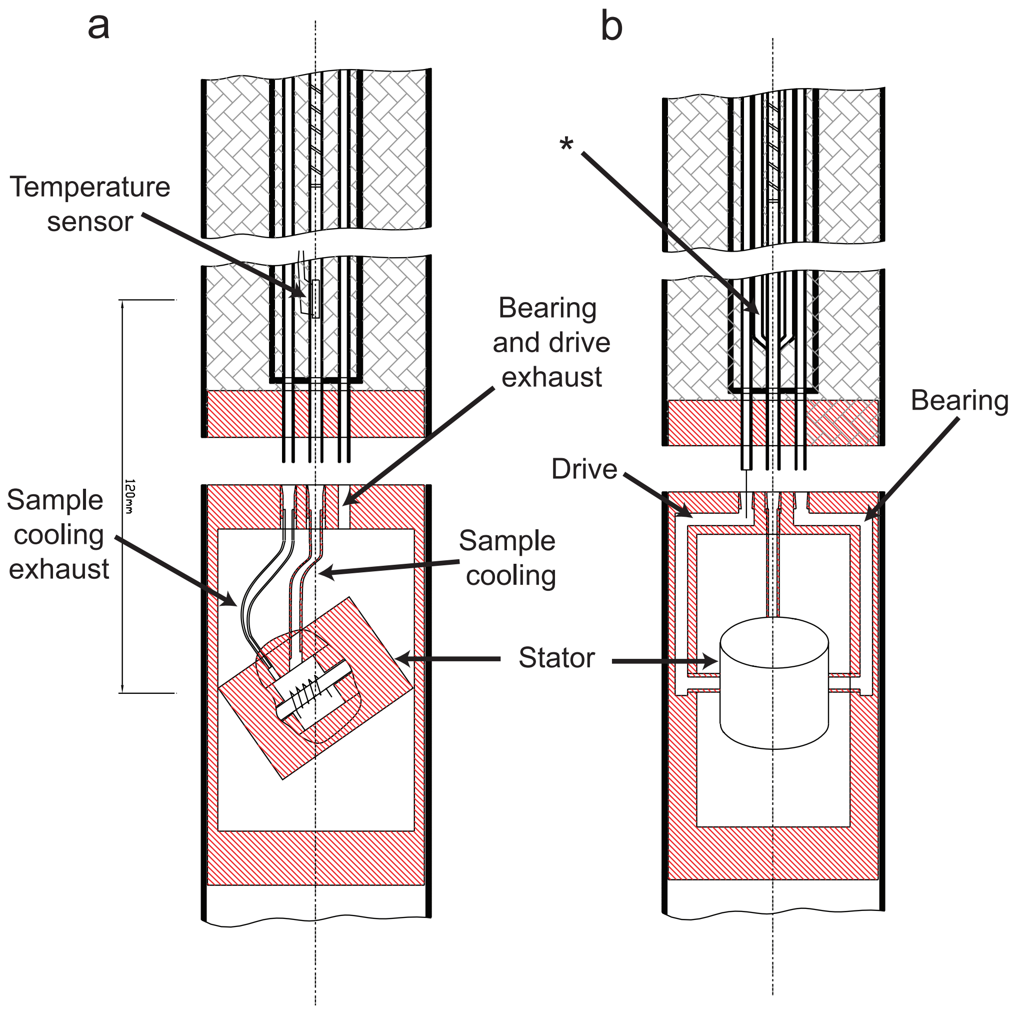

Fig. 4.3: A simplified view of the customize VT stack used in this work. a) Section view in the XZ-plane showing the cooling gas pipes and the position of the temperature sensor; b) section view in the YZ-plane showing bearing and drive pipes. The star symbol indicates how the bearing and drive pipes are in thermal contact with the exhaust of the cooling gas. The Z coincides with the direction of the static field.

Cooling Equipment

A custom made 4 mm NMR probe was designed and built to allow the in-situ cooling (and illumination) of the spinning sample. This probe is coupled to a modified VT stack (Fig. 4.3) that allows the thermal contact of bearing and drive with the precooled nitrogen gas flow used to cool the sample to the desired temperature. The VT stack and an exchange dewar are the core of the low-temperature set up in our design. The VT stack has a built-in heat exchanger that uses the cold exhaust gas to cool the bearing and the drive gases (see Fig. **??**. This effectively reduces the temperature gradient in the proximity of the sample. The exchange Dewar (capacity

160 L) is used to cool down the nitrogen gas flow below 120 K by thermal exchange with the liquid nitrogen inside the Dewar itself.

Temperature Calibration

In such an equipment, however, the readout temperature is still expected to be different, to some extent, from the real sample temperature. This latter needs to be properly calibrated, though. As explained in Ref. [104], the ^{207}Pb resonance of lead nitrate ($Pb(NO_3)_2$) is a good probe in this regard since its chemical shift varies with temperature. Moreover, the ^{207}Pb resonance in lead nitrate is very narrow, and its chemical shift has a large temperature dependence that is fairly linear over the range of -130 to 150 °C. Finally, lead nitrate provides a strong NMR signal close to the ^{13}C Larmor frequency so that measurements are quick and convenient. However, existing literature data on the ^{207}Pb chemical shift in lead nitrate do not go down to sufficiently low temperature for our purposes. Our calibrations is based on data that Ivo Heinmaa (from KBFI, Tallin) has made available in a private communication, and that show a linear relationship between chemical shift and temperature in the range 105K-300K for a static sample. These data are reported in Fig. 4.4 for both the perpendicular and parallel component of the chemical shift tensor (determined by fitting the static powder lineshape).

Since the sample is kept static, in these latter measurements, frictional heating is eliminated and the sample temperature has an error margin of roughly 1 K with respect to the readout temperature at the end of the VT stack. The isotropic chemical shift of ^{207}Pb fits the following equation:

$$\delta_{iso} = aT + b \tag{4.1}$$

where a = 0.7117 ppm K^{-1} and b = -3704.3 ppm. This trend-line is reported in Fig. 4.4 as a dotted line. The ^{207}Pb chemical shift scale was referenced to the calculated frequency of Me_4Pb derived from the ^{27}Al resonance frequency in aqueous $Al(NO_3)_3$ solution using the frequency ratio as given in Ref. [105].

In the case of a spinning sample a stepwise procedure was followed. Firstly, the thermocouple readout was properly calibrated by taking ^{1}H and ^{207}Pb NMR spectra of a rotor containing $Pb(NO_3)_2$ as well as a small sealed glass capillary of 2-methylpentane (freezing point = 119 K). The freezing of the 2-methylpentane could be detected as a broadening of the proton NMR signal. A good correspondence

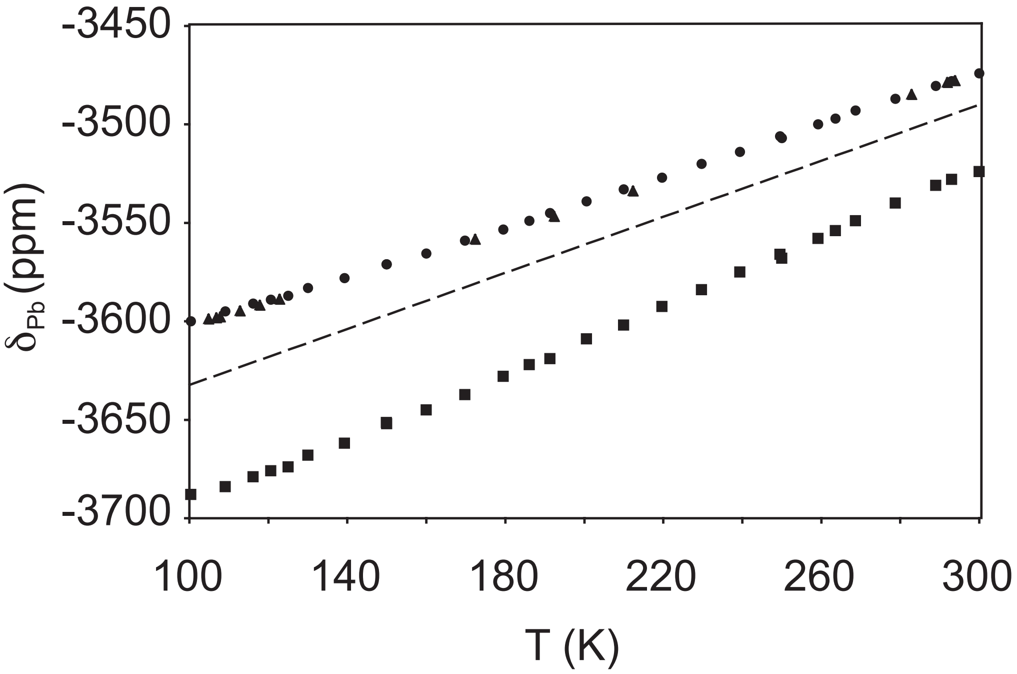

Fig. 4.4: ^{207}Pb chemical shift as a function of the sample temperature. Data from Ivo Heinmaa (private communication) refer to perpendicular (circles) and parallel (boxes) component of the lead chemical shift tensor. Triangles are data acquired in static conditions on our equipment and used for comparison. Dotted line is the best fit to isotropic chemical shift values (fitting function is reported in Eqn. 4.1).

between the sample temperature and the gas readout temperature was then observed for a static sample. More calibration points acquired with our equipment measuring the perpendicular component of the ^{207}Pb chemical shift tensor for $Pb(NO_3)_2$ are reported in Fig. 4.4 (triangles). They match quite well Heinmaa's data.

In a second step, the temperature calibration was performed while spinning at different spinning speeds. Note that the system was unstable for values of spinning speeds above 7 kHz.

The Eqn. 4.1 was used to interpret the isotropic ^{207}Pb chemical shift as a function of the temperature. As expected, the temperature inside the NMR rotor strongly depends on the cooling, bearing and drive gas flows as well as on the spinning frequency. In order to assess the temperature gradient inside the rotor, a 4 mm OD thin-wall (0.55 mm) rotor was filled with two different layers of $Pb(NO_3)_2$ (indicated as mix 1 and mix 2 in Fig. 4.5).

These layers consisted of a 1:1 mixture of $Pb(NO_3)_2$ and NaCl to avoid the damage that might occur to the rotor when spinning an high density sample at relatively

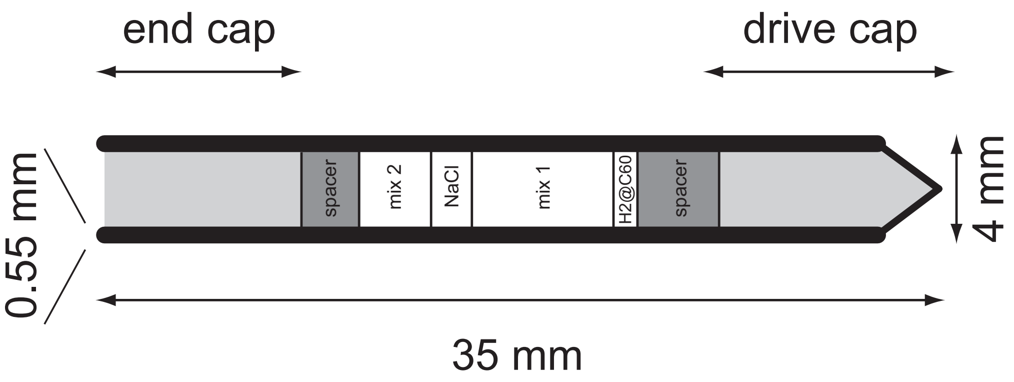

Fig. 4.5: Rotor packing used for temperature calibration procedures. Mix 1 and mix 2 labels refers to two (different) mixtures of $Pb(NO_3)_2$ and NaCl.

high MAS speeds. Moreover, the mixtures ensure the rotor is comparable in mass to the one used, later, in the rhodopsin experiments.

In addition, about 8 mg of the endohedral fullerene complex H2@C60 was fitted inside the rotor. The ^{1}H chemical shift of H2@C60 shows no measurable temperature dependence, and the proton line stays narrow even at low temperatures [100]. This make it possible to correct any apparent variation of the chemical shift due to susceptibility changes in the probe components, shim coils, or surrounding gas, rather than to a change in the temperature. Finally, to ensure reproducibility, the mass of all the rhodopsin filled rotors was kept close to the one used for the calibration and reported in Fig. 4.5. Fig. 4.6 shows the plot of real versus readout temperature as found in the calibration procedure of a sample spinning at 7 kHz.

Note the very large (but expected) difference in temperature between the interior of the rotor and the point at the end of the VT stack where the readout temperature is measured by the thermocouple. These differences are especially relevant in the low-temperature regime.

We found that the readout temperature was essentially useless for predicting the true sample temperature on our equipment. Moreover, conditions could be found where the real sample temperature (as measured by the ^{207}Pb chemical shift) was increased upon a change in gas flow parameters, while the readout temperature went down.

In the rhodopsin experiments, it was not possible to simultaneously measure the ^{207}Pb chemical shift, since the insertion of lead nitrate into the rotor would have compromised too much the sample volume. At the beginning of each NMR experimental session, the sample temperature was checked and eventually adjusted,

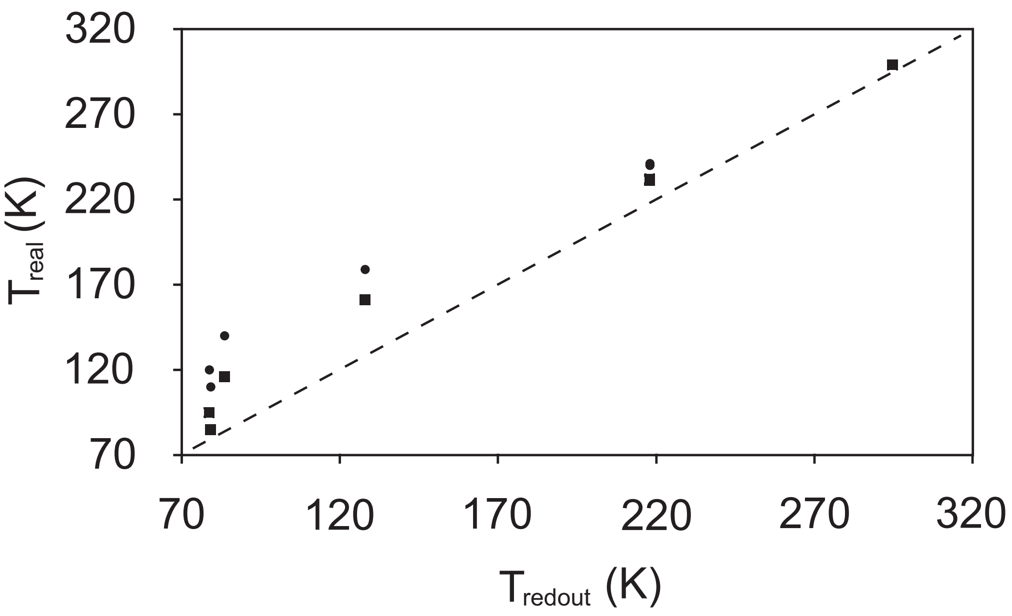

Fig. 4.6: Real sample temperature (as from the ^{207}Pb chemical shift data) versus thermocouple readout temperature, while spinning at 7 kHz. Circles: temperature at the edge of the rotor (mix 2). Boxes: temperature at the center of the rotor (mix 1). Dashed line: ideal condition - i.e the real temperature is equal to the readout temperature.

in a separate lead nitrate sample (mass and wall thickness identical to the targeted rhodopsin sample) using a single pulse experiment. The gas flows that give rise to the desired spinning frequency and stability for this rotor were then duplicated for the rhodopsin experiments. This procedure demanded the use of manual control over the bearing and drive gas flows. In separate experiments, it was confirmed that the radiofrequency irradiation has a negligible effect on the sample temperature (at least in this temperature regime). This was done by monitoring the ^{207}Pb chemical shift of a rotor containing lead nitrate in close contact with a frozen rhodopsin sample. The rf irradiation parameters were comparable to those used in the actual experiments. At these low temperatures, the mobile ions in the biological sample are immobilized and are not capable of absorbing energy from the electric field. The situation is very different when performing NMR at near-physiological conditions, where *rf* heating can be dramatic.

The temperature stability was also checked during the refilling of the exchange dewar and during the data acquisition (data are reported in Fig. 4.7).

After four hours (Fig. 4.7a) the temperature starts to go more rapidly up. How-

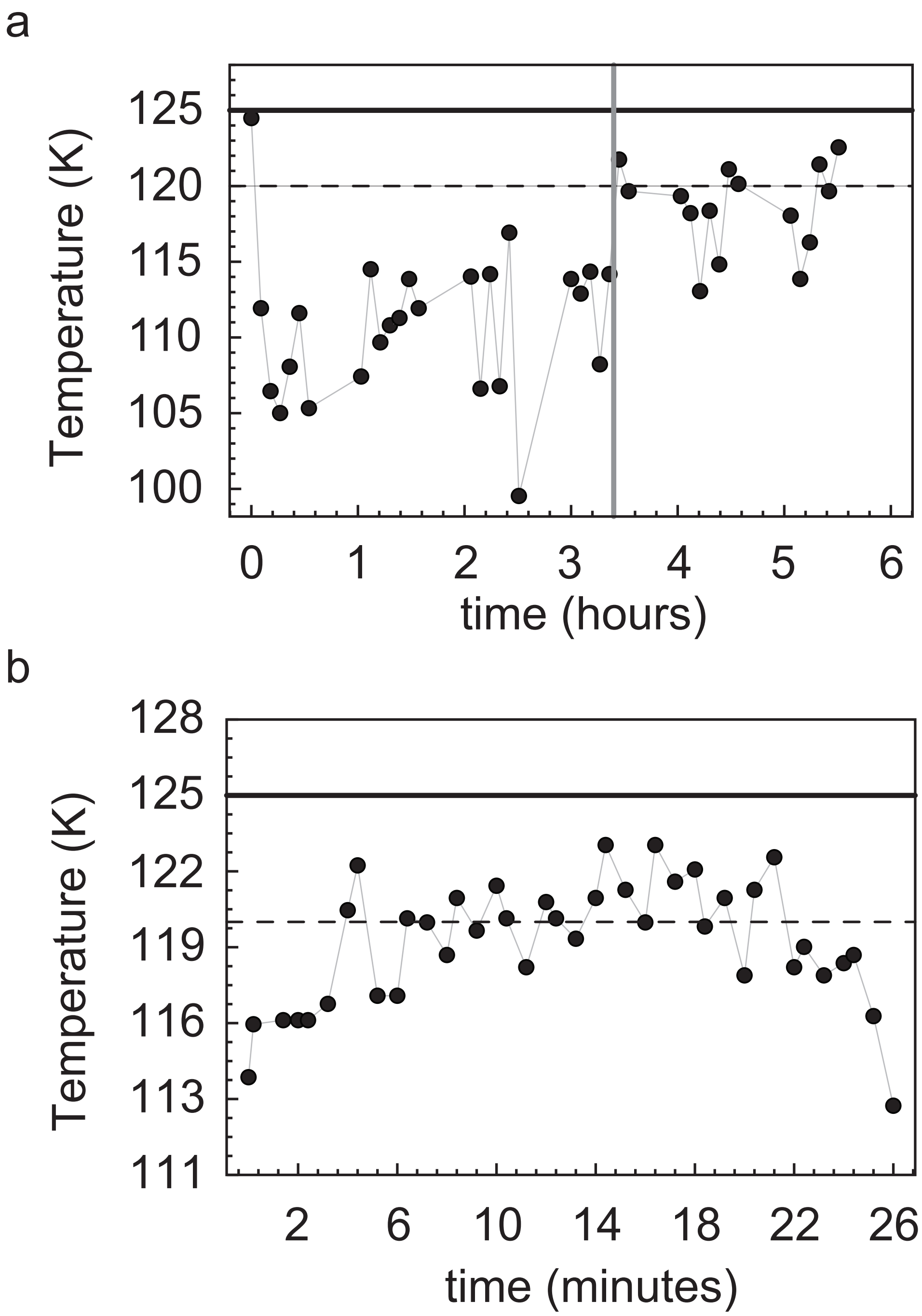

Fig. 4.7: a) Long term temperature stability; b) temperature stability during the refilling of the exchange dewar. Points refers to the warmest part of the rotor.

ever it stays below 125 K (the threshold for keeping bathorhodpsin stably in the sample) for as long as six hours at least. During the refilling of the exchange dewar a severe increasing of temperature was observed. This was kept under control by an appropriate (slow enough) refilling protocol as can be seen in Fig. 4.7b. Those measurements have indicated that a slow enough refilling of the exchange dewar has to be carried out every four hours. A typical NMR session of this kind runs for half a month, night and day.

4.2.2 *The Illumination Issue*

A clean preparation of bathorhodopsin by illumination of a rhodopsin sample kept at low temperature is complicated by at least two factors: i) the complex photochemistry of the rhodopsin photocycle, and ii) the limited penetration of light into the sample, due to the strong photon absorption by rhodopsin and bathorhodopsin at the surface. As shown in Fig. 4.8, for example, the distorted all-*trans* chromophore of bathorhodopsin may itself be photoisomerized, leading to either the starting 11-*cis* state (i.e. rhodopsin) or the 9-*cis* side product (i.e. isorhodopsin) [7].

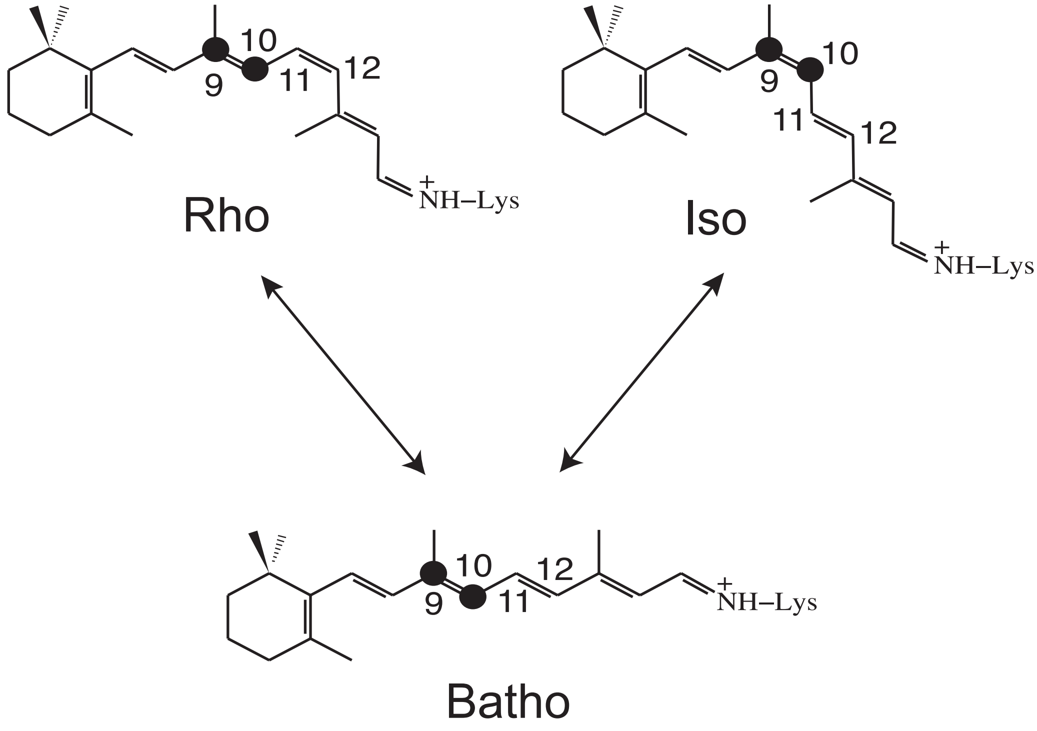

Fig. 4.8: The three rhodopsin isomers involved at temperatures below 125 K. The 9,10-$^{13}C_2$ labels are indicated by filled circles.

The three species have different optical absorption spectra, as shown in Fig. 1.11. The absorption maximum of the ground state rhodopsin occurs at 506 nm, while bathorhodopsin has a red-shifted absorption maximum occurring at 543 nm; isorhodopsin has a blue-shifted absorption maximum occurring at 494 nm [50]. Furthermore, absorption of light by isorhodopsin may, in turn, lead to regeneration of bathorhodopsin itself. The absorption spectra and wavelength-dependent quantum yields of the three molecules, i.e. rhodopsin, bathorhodopsin and isorhodopsin, have been thoroughly documented [49, 50, 7].

Simulations of Light Penetration and Photoisomerization

Two techniques have been used in parallel to study the light penetration and photoisomerization in optically-dense rhodopsin samples (and to optimize the conditions for the study of the functionally-relevant bathorhodopsin photostate). Firstly, a finite-element numerical simulations was performed in order to predict the accumulation of the isorhodopsin and bathorhodopsin photoisomers in cold illuminated samples, as a function of time, space, rhodopsin concentration, illumination intensity, and light wavelength distribution. Secondly, results from those simulations were validated by double-quantum ^{13}C solid-state NMR on a retinylidene-rhodopsin sample ^{13}C-doubly-labelled at positions C9 and C10 of the retinylidene prosthetic group. Note that solid-state NMR can follow the photoisomerization process in thick samples since each photoisomer has a set of characteristic ^{13}C chemical shifts, and the samples are almost completely transparent to radiowaves. The balance of photoisomers is therefore probed in the interior of the sample, rather than at the surface, in contrast to optical studies. The simulation technique is here discussed as a part of this methodology chapter. Results from simulations compared with NMR evidence are then discussed later in the experimental result part. These findings have been published in Paper 5 to which I extensively refer.

Consider a sample of lipids loaded with rhodopsin, with the initial rhodopsin concentration denoted $c_R{}^0$. Photons with a distribution of wavelengths impinge on the surface, which is assumed to be flat. The photons penetrate the sample and induce photoisomerization between the three forms: rhodopsin, bathorhodopsin and isorhodopsin. If the temperature is low enough, and all side reactions are ignored, the concentrations of the three photoisomers vary as a function of time and depth below the surface, such that the total concentration of rhodopsin isomers is constant, i.e.

$$c_R(z,t) + c_B(z,t) + c_I(z,t) = c_R^0 \tag{4.2}$$

The simulations may predict the dependence of the three concentrations on depth

z and time t, and thereby gain insight into the optimal conditions for preparation of bathorhodopsin. Denote the incident photon flux density (number of photons per unit time and unit area, at a given wavelength λ) by ${I_\lambda}^0$. Illumination with a mixture of wavelengths is taken into account by defining an incident photon flux vector as follows:

$$I^0 = \begin{pmatrix} I^0_{\lambda_1} \\ I^0_{\lambda_2} \\ . \\ . \\ . \end{pmatrix} \tag{4.3}$$

Consider a small volume element δV=$A\delta z$, with surface area A, located at depth z below the illuminated surface (defined to be at z=0), and with a thickness δz (assumed to be small enough that there is negligible change in light intensity while traversing the slice). Denote the concentrations of rhodopsin, bathorhodopsin and isorhodopsin in this volume element at a given time t by a 3-vector:

$$c(z,t) = \begin{pmatrix} c_R(z,t) \\ c_B(z,t) \\ c_I(z,t) \end{pmatrix} \tag{4.4}$$

The absorption coefficients of the three relevant species are given in the literature over a range of wavelengths [7]. These coefficients may be collated by defining an extinction coefficient matrix:

$$\varepsilon = \begin{pmatrix} \varepsilon_R(\lambda_1) & \varepsilon_R(\lambda_2) & ... \\ \varepsilon_B(\lambda_1) & \varepsilon_B(\lambda_2) & ... \\ \varepsilon_I(\lambda_1) & \varepsilon_I(\lambda_2) & ... \end{pmatrix} \tag{4.5}$$

The rows of the matrix define the properties of individual photoisomers, while the columns of the matrix indicate the photon wavelengths. The simulations described here use use the following matrix:

$$\varepsilon = \begin{pmatrix} 14.2 & 40.9 & 43.7 & 6.1 & 1.0 \\ 12.4 & 30.0 & 47.8 & 46.4 & 30.0 \\ 17.9 & 46.9 & 36.2 & 0.6 & 0.1 \end{pmatrix} \cdot 10^{-3} M^{-1} cm^{-1} \tag{4.6}$$

where the columns refer to light wavelengths of 420 nm, 479 nm, 520 nm, 565 nm and 620 nm respectively, and the rows correspond to rhodopsin, bathorhodopsin and isorhodopsin. These parameters are taken directly from Ref. [7], except for the 420 nm data, which was estimated from published absorption curves [50]. Note that bathorhodopsin has the strongest absorption at long wavelengths, while isorhodopsin has the strongest absorption at short wavelengths (see Fig. 1.11). Denote the flux density for photons of wavelength impinging on the surface of the volume element δV at time t by $I_\lambda(z,t)$. These photons may either be transmitted through the slice, or absorbed by one of the photoisomers. The photon flux illuminating a slice at depth z and time t at a set of different wavelengths is given by the column vector $I(z,t)$ as follows:

$$I(z,t) = \begin{pmatrix} I_{\lambda_1} \\ I_{\lambda_2} \\ . \\ . \\ . \end{pmatrix} \tag{4.7}$$

First consider the transmission of light from one slice to the next. From the Beer-Lambert law, the numbers of photons at each wavelength λ absorbed by all photoisomers at depth z per unit time are given by the elements of the following vector:

$$I^{abs}(z,t) = c(z,t)^T \cdot \varepsilon \cdot I(z,t) \lambda z \cdot ln(10) \tag{4.8}$$

where the factor $ln(10)$ is required by the conventional definition of the absorption coefficient, and the superscript T indicates a transpose. If one assumes that all photons are either absorbed or transmitted (neglecting reflection and scattering), the wavelength-dependent photon flux impinging on the next slice is given by :

$$I(z+\delta z,t) = I(z,t) - I^{abs}(z,t) \tag{4.9}$$

At each point in time, the photon flux inside the sample may be calculated by applying Eqn. 4.8 and Eqn. 4.9 to successively deeper sample layers, providing that the spatially-dependent isomer concentrations $c(z,t)$ are known. Now consider an individual rhodopsin molecule located in the volume element δV at time t. The probability of this molecule absorbing a photon of any wavelength during the time interval δt is given by

$$p_R^{abs}(z,t) = ln10 \cdot \sum_\lambda \varepsilon_R(\lambda) I_\lambda(z,t)\delta t \tag{4.10}$$

Hence the concentration of rhodopsin molecules absorbing photons in the volume element δV during the time interval δt is given by :

$$c_R^{abs}(z,t) = p_R^{abs}(z,t)c_R(z,t) = ln(10) \cdot \sum_\lambda \varepsilon_R(\lambda) c_R(z,t) I_\lambda(z,t)\delta t \tag{4.11}$$

This calculation may be repeated for the two other photoisomers leading to the elements of the vector c^{abc} *(z,t)*, which represents the concentration of molecules of each photoisomer absorbing light in the volume element δV during the time interval δt:

$$c^{abs}(z,t) = ln(10) \cdot \sum_\lambda \begin{pmatrix} \varepsilon_R(\lambda)c_R(z,t) \\ \varepsilon_R(\lambda)c_R(z,t) \\ \varepsilon_R(\lambda)c_R(z,t) \end{pmatrix} I_\lambda(z,t)\delta t \tag{4.12}$$

When a photon is absorbed, it may either lead to a photoisomerization process, or regeneration of the initial state. The probabilities of these processes are summarized by a *quantum yield matrix*, denoted Φ, which is defined as follows:

$$\Phi = \begin{pmatrix} \Phi_{RR} & \Phi_{RB} & \Phi_{RI} \\ \Phi_{BR} & \Phi_{BB} & \Phi_{BI} \\ \Phi_{IR} & \Phi_{IB} & \Phi_{II} \end{pmatrix} \tag{4.13}$$

where for example the element Φ_{BR} indicates the probability that a photo-excited rhodopsin molecule generates a bathorhodopsin molecule (the subscripts should be read from right to left). Diagonal elements such as Φ_{RR} indicate the probability that a rhodopsin molecule, having absorbed a photon, simply returns to its initial state. All columns sum to unity, corresponding to the assumption that absorption of a photon always leads to either no isomerization at all, or to generation of one of the two specified photoisomers, with no side-reactions. The quantum yields are documented in the literature [7, 49] and are wavelength-dependent. In practice, we used the following matrix:

$$\Phi = \begin{pmatrix} 0.33 & 0.33 & 0 \\ 0.67 & 0.60 & 0.16 \\ 0 & 0.07 & 0.84 \end{pmatrix} \tag{4.14}$$

This is adapted from the published data in Ref. [7, 49], ignoring the wavelength-dependence of the quantum yields, for the sake of simplicity. Note that both rhodopsin and isorhodopsin may be isomerized directly to bathorhodopsin, but not to each other. In addition, note that rhodopsin is isomerized to bathorhodopsin with approximately twice the efficiency of isorhodopsin. The changes in the three photoisomer concentrations at depth z during a small time interval δt are therefore given by the following vector:

$$\delta c(z,t) = \Phi \cdot c^{abs}(z,t)\delta t \tag{4.15}$$

Eqn. 4.12 and Eqn. 4.15 relate the change in the isomer concentrations to the penetration of light, while Eqn. 4.8 and Eqn. 4.9 relate the penetration of light to the isomer concentrations. The changing profiles of photoisomer concentrations may therefore be predicted by numerical integration of these equations using the boundary conditions of a constant light flux density at the sample surface, and a starting state of no photoisomerization:

$$\begin{aligned} I_\lambda(0,t) &= I_\lambda^0 && \textit{(independent of t)} \\ c(z,0) &= \begin{pmatrix} c_R^0 \\ 0 \\ 0 \end{pmatrix} && \textit{(independent of z)} \end{aligned} \tag{4.16}$$

where ${c^0}_R$ is the initial rhodopsin concentration. Incident light with different spectral characteristics may be simulated by using incident photon flux densities I_λ^0 for several different wavelengths. The dynamical equations were integrated by finite-element numerical simulations using about 100 volume elements and 5000 time increments. The thickness of the volume elements and the length of the time intervals were reduced until the calculations converged to a stable result. In practice δV was around around 5 μm and δt was a few seconds. The starting concentration of rhodopsin was c_R^0=5.8 mM, corresponding to the typical concentration of our sample preparations.

Our results (discussed in details in the next chapter) show that the optimal illumination conditions for generation of bathorhodopsin are quite different in optically-thin and optically-thick samples. In the case of optically-thin samples, the yield of bathorhodopsin is relatively insensitive to the wavelength distribution of the visible light. However, in the case of samples thicker than a few tens of microns, the wavelength distribution of the incident light has a strong influence on the bathorhodopsin yield. Long-wavelength components in the light destroy bathorhodopsin and cause the accumulation of isorhodopsin, which is usually an unwanted side product. In samples with rhodopsin concentrations of around 6 mM, bathorhodopsin cannot be generated at depths greater than about 400 μm in a reasonable amount of time, however strong is the light, and whatever its wavelength. This conclusion guided the development of a new protocol for improving the yield of bathorhopsin, in which the rhodopsin is mixed with small glass beads to increase the illuminated surface area and the choice of the correct illumination equipment. These two technical aspects are discussed in the following two sections.

Rotor Packing

As discussed above, Rhodopsin has a very high molar extinction coefficient which makes hard for the light to penetrate the sample. Simulations above use the real light intensity together with real values of sample concentration in order to estimate how deep the light, filtered by three different filters, can go into the sample. Furthermore, the three involved species have been taken into account (namely rhodopsin, bathorhodopsin and isorhodopsin) in order to establish how much of each is formed and thus decide the best filter to be used.

These simulations have shown, it is anticipated, that a good amount of bathorhodopsin is available when using the band-pass filter at 420 nm. However, even in this condition, only a thin layer of about 150 μm of the rhodopsin sample can be excited and converted into bathorhodopsin over a period of about 10-12 hours. Simulation have also shown that increasing the exposure time and/or the light intensity do not much improve these results. To further improve light penetration it was thought to mix rhodopsin with glass beads in order to diffuse the light deeper into the sample. However, this complicates the rotor packing procedure since care should be taken

Tab. 4.1: Composition of the four retinylidene-rhodopdin isotopomer samples used in this work. I refers to the [9,10-$^{13}C_2$]-, II to [11,12- $^{13}C_2$]-, III to [12,13 $^{13}C_2$]- and IV to [14,15-$^{13}C_2$]-compound. Pellet indicate the mixture of (mainly) protein, lipid and water resulting from the incorporation of the isotopically-labelled-retinal into the opsin. Protein refers to the pure rhodopsin content.

Sample Label	Pellet (mg)	Glass beads (mg)	Protein (mg)
I	45	38	7
II	50	25	3
III	46	34	9
IV	47	37	

in not destroying the lipid membrane that would generate complication in the spectral pattern. Aware of that, the following procedure was used: a precooled (-80° Celsius) custom-made aluminum mortar was used to grind the frozen lipid/protein mixture before to be mixed (in a 2:1 w/w ratio) with glass beads of an average diameter, d $\leq$ 100 μm. Liquid nitrogen was used in order to keep the mixture frozen during the grinding. The mixture was then transferred into a 4 mm thin wall ZrO_2 rotor (VARIAN pencil 2) using a precooled custom-made aluminum funnel. All the manipulations involving rhodopsin were done in dim red light at $\lambda \geq$ 700 nm. Tab. 4.1 resumes the composition of the five samples packed and used in this thesis.

As a side note: a sapphire rotor was tested but found to be unsuitable for this application. Even if sapphire rotors would allow much more light to the sample, its high thermal conductivity at low temperatures makes it more difficult to reach the required sample temperature of 120 K. This is because the nitrogen gas bearings have to be kept relatively warm in order to avoid spinning instabilities, since the viscosity and density of nitrogen gas is a strong function of temperature near its boiling point. Under these conditions, the high thermal conductivity of sapphire conducts heat efficiently from the relatively warm bearing region into the sample chamber. As a result, we found that sufficiently low sample temperatures could only be attained by using a zirconia rotor. In principle, sapphire rotors could be used in conjunction with cold helium as the bearing gas, but this would require a considerable redesign and additional expense.

Optical Assembly

As a final section we report here the detail of the optical assembly used in this work. This experimental set up it is the results of the experience gained working with this subject combined to the measurements and simulations above discussed. The sample is illuminated directly inside the NMR rotor by using two light sources, each made by a 250 W quartz halogen lamp, a filter and an optical lens. The light from each lamp is passed through the interference filter to select the appropriate wavelength and suppress infrared components. It is then focused on to the polished ends of an optical fibre bundle. A total of 14 optical fibres were used. They are directed onto the outside of the sample rotor from a variety of angles (see Fig. 4.9). Three different filters were used in turn: a band pass (BP) filter centered on $\lambda = 480$ $\pm$ 5 nm; one centered on 420 $\pm$ 5 nm; and a low pass (LP) filter with $\lambda \geq$ 495nm. The illumination wavelength used ($\lambda = 420 \pm 5$) was chosen to maximize the light penetration in dense samples while minimizing the formation of isorhodopsin that would interfere with bathorhodopsin formation as well as with signal assignment

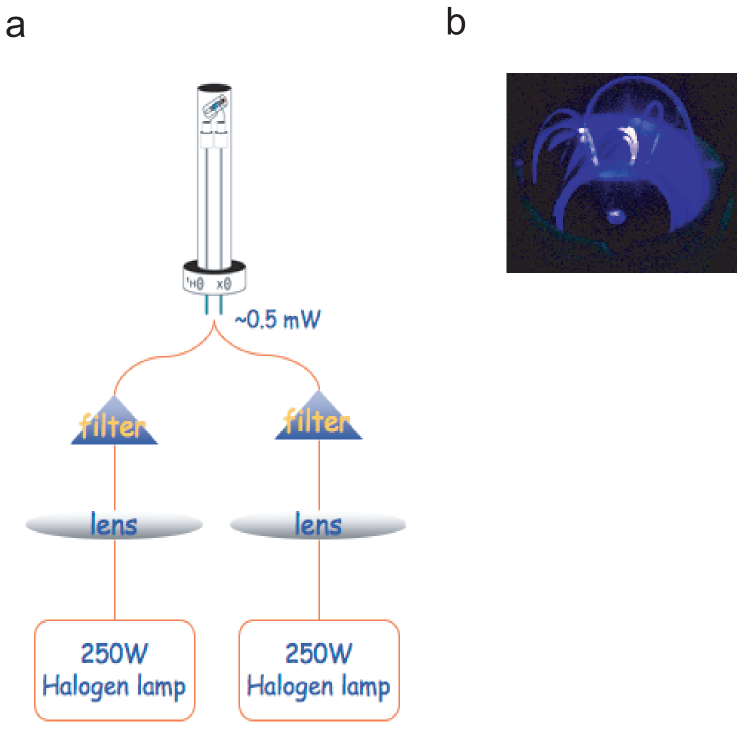

Fig. 4.9: a) A pictorial representation of the optical assembly used to illuminate (in-situ) rhodopsin samples in order to start its photocycle; b) a picture of the probe stator illuminated with the equipment in a) and using a band pass filter centered on 420 $\pm$ 5 nm.

[7]. In the case of a narrow-band interference filter, an optical power output of 30 μW was measured at the end of each fibre by using an optical power meter. The attenuation of the light by the rotor walls (0.55 mm wall thickness) was measured to be about 90%. The total light power at the sample surface out from all the 14 optical fibres was estimated to be about $P \simeq 42\,\mu$W, in the case of narrow-band filtered light. The estimated light power P at a single wavelength λ may be converted into a photon flux estimated by using the formula $I_{\lambda}^{0} = (P\lambda)/(hcA)$ where A is the illuminated area. In the present case the illuminated area, A, is roughly $\simeq 182{\cdot}10^{-6}$ m^2 (using a sample radius of 1.45 mm and length 20 mm). This leads to an estimated photon flux at the sample surface of $I_{\lambda}^{0} \simeq 0.75\,\mu$ mol m^{-2} s^{-1} for a wavelength of 420 nm.

5. RESULTS

5.1 Review of Aims

The photon absorption in rhodopsin leads to an ultrafast ($<$200 fs) and highly selective isomerization of the retinylidene conjugated chain from the initial 11-*cis* configuration to a distorted all-*trans* configuration of the rhodopsin chromophore. The resultant photostate, called bathorhodopsin, is a highly energetic species that stores about 2/3 of the photon energy [4]. Subsequently, the highly distorted chromophore relaxes and the transduced energy is used to drive conformational changes in the opsin protein. This leads to a change in the transmembrane potential and the induction of an optic nerve signal. What is the nature of the protein-chromophore interactions that store the energy needed to drive subsequent protein conformational changes? To address this question, we studied bathorhodopsin by low temperature solid-state NMR. Recent X-ray crystal structures provide more detailed structural models for rhodopsin [1] and bathorhodopsin [53]. Due to their limited resolution, these structures do not provide direct clues for the energy storage mechanism, but they do provide a very useful framework for hybrid quantum mechanical (QM/MM) [71, 14], molecular dynamics (MD) [72], and density functional theory (DFT) [58, 70] calculations. These calculations led to several models assessing the respective contributions of intramolecular strain, electrostatic interaction, and chromophore/protein van der Waals interactions to the energy storage mechanism. Solid state NMR measurements on rhodopsin photointermediates provide chemically resolved data on the chromophore from which precise information on electronic charge distribution can be derived; this may be very valuable for testing the different models suggested by computational methods. In this direction double quantum filtered dipolar recoupling solid state NMR experiments have been applied to acquire ^{13}C chemical shifts along the retinylidene chain of the chromophore and to measure distances between two ^{13}C labelled carbons. Double-quantum heteronuclear local field spectroscopy (2Q-HLF) was then used for the direct estimation of torsional angles. From the chemical shift data a tentative interpretation [106] was also done. Our results indicate that both electrostatic interactions and torsional strain are involved in the energy storage mechanism of bathorhodopsin. Distance and torsional angle measurements were performed in order to support our first tentative interpretation and to evaluate the effect of the distortion as a general mechanism for storing the light energy that is used to drive subsequent conformational changes in light-activated proteins. The rest of the chapter is organized as follow: i) chemical shifts measurements of various retinylidene-bathorhodopsin isotopomers; ii) torsional angle measurements on [11,12-$^{13}C_2$]-retinylidene-bathorhodopsin and -isorhodopsin; iii) distance measurements on [14,15-$^{13}C_2$]-retinylidene-bathorhodopsin.

5.2 Chemical Shift Measurements

5.2.1 NMR experiments setup

A picture of the retinal with the numbering of carbon sites is reported in Fig. 5.1

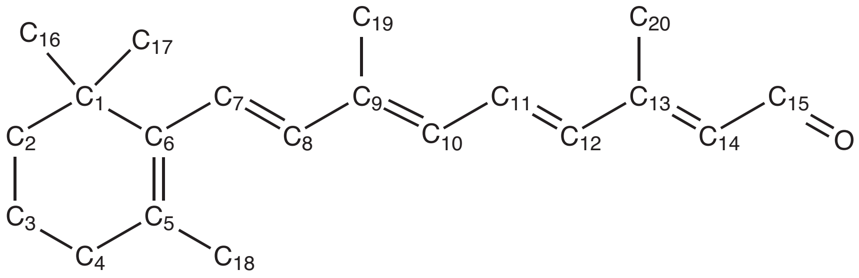

Fig. 5.1: Structure and numbering of the carbon sites of the retinal.

Observation of the ^{13}C NMR signals from the $^{13}C_2$-labelled chromophore requires suppression of the dominant signals from natural-abundance ^{13}C nuclei in the protein and lipid matrix. This was done by using the double-quantum-filter pulse sequence shown in Fig. 3.3. After cross-polarization of ^{1}H magnetization to ^{13}C, double-quantum ^{13}C coherences were excited by using a $R20_2^9$ symmetry-based recoupling sequence (see Sec. 3.2). The radiofrequency phases in the recoupling sequence are shown explicitly in Fig. 3.3. The double-quantum excitation and reconversion periods were kept equal to a value experimentally optimised in order to maximize the double-quantum efficency ($\tau_{exc} = \tau_{rec} = 400\,\mu$s). No decoupling was performed on the ^{1}H channel during the $R20_2^9$ double-quantum recoupling sequence according to Ref. [107] where it was experimentally shown that at high enough power on the ^{13}C channel no decoupling is necessary on the ^{1}H channel. ^{1}H decoupling during the acquisition of the ^{13}C free induction decay was achieved using a SPINAL-64 sequence (Small Phase INcremental ALternation with 64 steps) [108] and a ^{1}H *rf* nutation frequency of 80 kHz and a pulse length of 6.3 μs. Signal passing through double-quantum ^{13}C coherence was selected by using a 16 step phase cycle. The double-quantum-filtering efficiency (as compared to a cross-polarization experiment without double-quantum filtration) was around 35%. The selection of the $^{13}C_2$-labelled chromophore signals was usually excellent, although weak residual signals at the positions of the strong protein and lipid peaks could sometimes be observed. The NMR spectra collected result from summing together around 10^4 NMR signal transients, each separated by 5 seconds delay for thermal equilibration of the nuclear spin magnetization. Each spectrum required about 17 hours of data acquisition.

5.2.2 White Light illumination

Numerical simulations (see Sec. 4.2.2) have been performed in order to predict the amount of bathorhodopsin and isorhodopsin generated by illuminating the sample with white light. These results were validated by using double quantum ^{13}C solid state NMR of rhodopsin samples labeled with ^{13}C at position 9 and 10 (Fig. 5.1) of the retinylidene group.

Numerical Simulation

Fig. 5.2 shows numerical photoisomerization simulation results obtained by illuminating a sample containing 5.8 mM of rhodopsin exposed to white light.

In these simulations the effect of white illumination is emulated (in a simplified way) by employing photons at five different wavelengths (420 nm, 479 nm, 520 nm, 565 nm and 620 nm). For each of them the incident photon fluxes were set to I^0_λ=0.75 μmol m^{-2} s^{-1}. In Fig. 5.2 the concentrations of rhodopsin, bathorhodopsin and isorhodopsin are shown by a solid grey line, a solid black line, and a dashed line respectively. The top left panel (Fig. 5.2a) shows the initial impact of the white light: about half of the rhodopsin sample is isomerised to bathorhodopsin but only within a $\sim$40 μm surface layer. In the initial stages the light is completely absorbed by the rhodopsin nearer the surface and the lower layers are not affected.

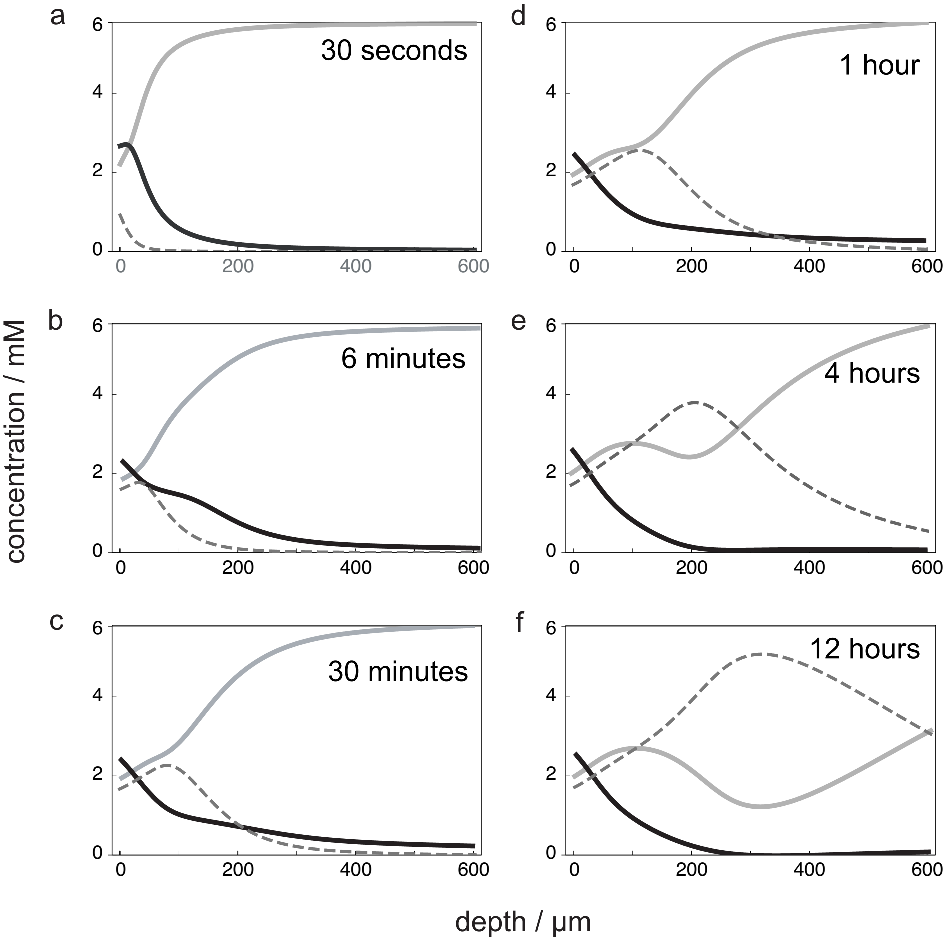

Fig. 5.2: Finite-element numerical simulations obtained by illuminating the sample with white light. The plots show the simulated concentrations of rhodopsin (solid grey line), bathorhodopsin (solid black line) and isorhodopsin (broken line) at the indicated times, as a function of depth below the surface (horizontal axis).

After a few minutes of illumination (Fig. 5.2b), the light reaches a depth of about ∼150 μm in which rhodopsin is mainly converted into bathorhodopsin. The behaviour in this part of the sample, where light is abundant, is dominated by the quantum yields: rhodopsin has a large quantum yield for conversion to bathorhodopsin and hence bathorhodopsin is favoured in this region.

As the illumination continues (Fig. 5.2c-e), the build-up of bathorhodopsin is reversed in favour of a strong accumulation of the isorhodopsin photoisomer. At long times (Fig. 5.2f), most of the interior of the sample is converted to isorhodopsin, with bathorhodopsin still confined to a ∼40 μm surface layer. This behaviour in this part of the sample is dominated by the absorption characteristics of the three photoisomers involved. As we can see from the absorption spectra (Fig. 1.11), rhodopsin, bathorhodopsin and isorhodopsin absorb strongly at medium-to-short wavelengths, so only long-wavelength red/orange light penetrates to large depths. The absorption in the red region of the spectrum is stronger for rhodopsin and bathorhodopsin than for isorhodopsin. Although bathorhodopsin has a low quantum yield for conversion to isorhodopsin, any isorhodopsin that is formed deep in the sample by photoisomerization of bathorhodopsin remains in that form since isorhodopsin is almost transparent to red light. Furthermore, the conversion of the other isomers into isorhodopsin makes the sample even more transparent to red light, so the conversion process can now proceed at greater depths than before. As a result, isorhodopsin accumulates in the sample interior.

Experimental Results

Before illuminating the sample, a double-quantum filtered spectrum of the [9,10-$^{13}C_2$]-retinylidene-rhodopsin sample was recorded at T = 120 K by spinning the sample with a frequency $\omega_r/2\pi = 7$ kHz (Fig. 5.3a).

The chemical shifts of the two peaks in the spectrum (148.9 ppm for C9 and 127.9 ppm for C10) agree with the values obtained in previous studies [10]. In Fig. 5.3b, a DQF spectrum of [9,10-13C]-retinylidene-rhodopsin acquired after 12 hours of illumination under white light is shown. The retinylidene-C10 rhodopsin peak is reduced in intensity and a strong new peak appears at 131.4 ppm. This is attributed to the retinylidene-C10 site of isorhodopsin, in agreement with previous isorhodopsin data [109]. In addition, the low-field peak becomes slightly broader after illumination. This is consistent with the retinylidene-C9 peak of isorhodopsin being at 148.2 ppm. [109]. About half of the sample is isomerized into isorhodopsin. In Tab. 5.1 are reported the isotropic C9 and C10 ^{13}C chemical shift of rhodopsin and isorhodopsin as measured in our study together with the isomerization shifts ($\Delta\delta_{isom} = \delta_{iso}$-$\delta_{rho}$, i.e. the change in chemical shifts after isomerization from rhodopsin to isorhodopsin).

The generation of a large isorhodopsin fraction by white light illumination is in agreement with the simulations of light penetration and photoisomerization, described above.

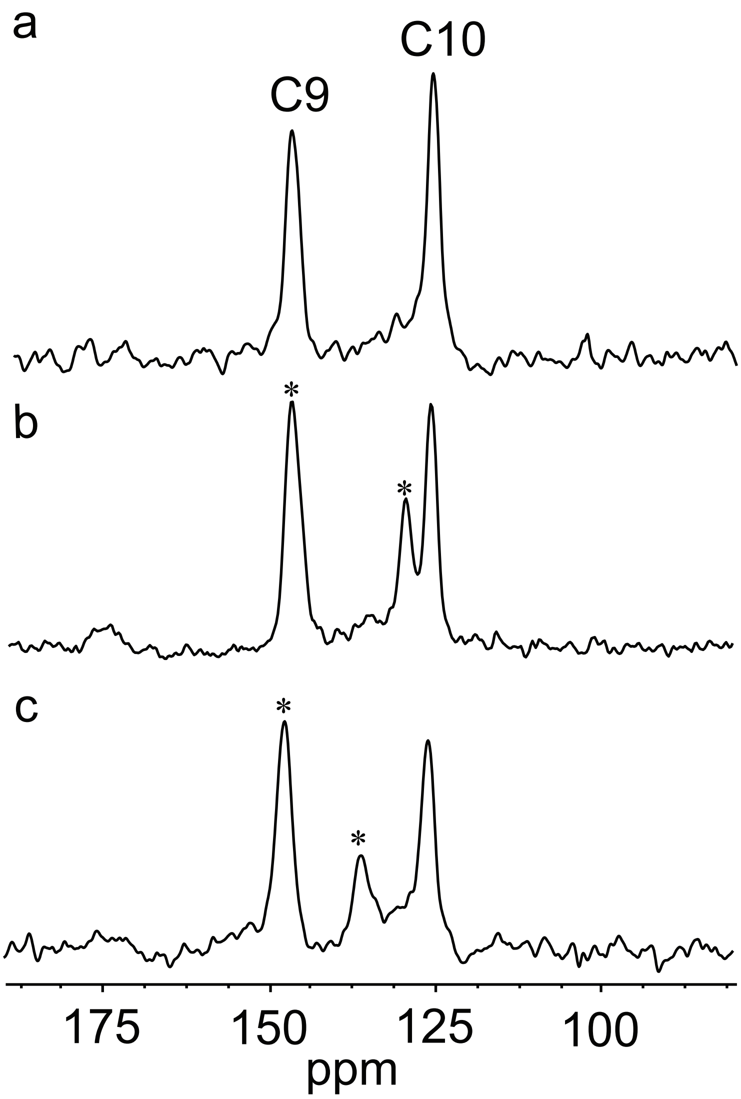

Fig. 5.3: Double-quantum filtered ^{13}C NMR spectra of [9,10-^{13}C]-retinylidene-rhodopsin: a) before the illumination (12 k scans); b) after 12 hours of illumination under white light (8 k scans); c) after 12 hours of illumination with 420 ± 5 nm light on an homogenous mixture of rhodopsin and glass beads. All spectra were acquired at a temperature below 120K with magic-angle spinning at 7.00 ± 0.05 kHz. All chemical shifts are referenced indirectly to TMS using the rhodopsin shift data in Ref. [10]. The positions of the new signals are indicated by asterisks.

5.2.3 Violet Light - Monochromatic Illumination at 420 nm

The use of a monochromatic 420 nm light is now discussed through simulations and experimental results collected on the four rhodopsin isotopomers.

Tab. 5.1: Isotropic ^{13}C chemical shifts of rhodopsin δ_{rho} and isorhodopsin δ_{iso} as found in this work. The last column shows the isomerization shift, $\Delta\delta = \delta_{iso} - \delta_{rho}$. All chemical shifts are referenced indirectly to TMS using the rhodopsin shift data in Ref. [10].

^{13}C site	δ_{rho}/ppm	δ_{iso}/ppm	$\Delta\delta$/ppm
C9	148.9	148.2	-0.7
C10	127.9	131.4	3.5

Numerical Simulations

The numerical simulations in Fig. 5.4 show how the isomer concentration profiles are predicted to change in time when the sample is illuminated with monochromatic violet light.

The photon flux at 420 nm is assumed to be I^0_{420}=0.75 μmol m^{-2} s^{-1}, with all the other photon fluxes set to zero. The immediate impact of the illumination is to isomerize the outer rhodopsin layer to bathorhodopsin, with an efficiency of about 50%. Isorhodopsin is barely formed at all at short times, since bathorhodopsin absorbs short wavelengths inefficiently, and the quantum yield for conversion of bathorhodopsin to isorhodopsin is low. At longer times a thicker layer of the sample is isomerized, generating an outer layer of mixed bathorhodopsin and isorhodopsin in a ratio of about 10:1. However the advance of the isomerization front progressively slows down as time goes on. After about 12 hours of illumination, a layer of thickness $\sim$300 μm is isomerized. The filled symbols in Fig. 5.5 show the depth of the isomerization front as a function of time, as derived from the numerical simulation results.

The front advances rapidly in the initial phase but the advance becomes very slow once the critical depth of about $\sim$300 μm is reached. The progress of the front beyond this point is well-described by a power law of the form $z = at^{\alpha}$, where the exponent $\alpha = 0.184$ was determined by fitting the simulation results at long times (solid line in Fig. 5.5). This weak exponent indicates that it is impractical to thicken the isomerization layer by extending the illumination time. For example, doubling the thickness of the isomerization layer would require a 40-fold increase in the illumination time. Further simulations show that increasing the light intensity does not thicken the isomerization layer, but simply speeds up the process of attaining the $\sim$300 μm. A decrease in the concentration of the chromophores does not help either.

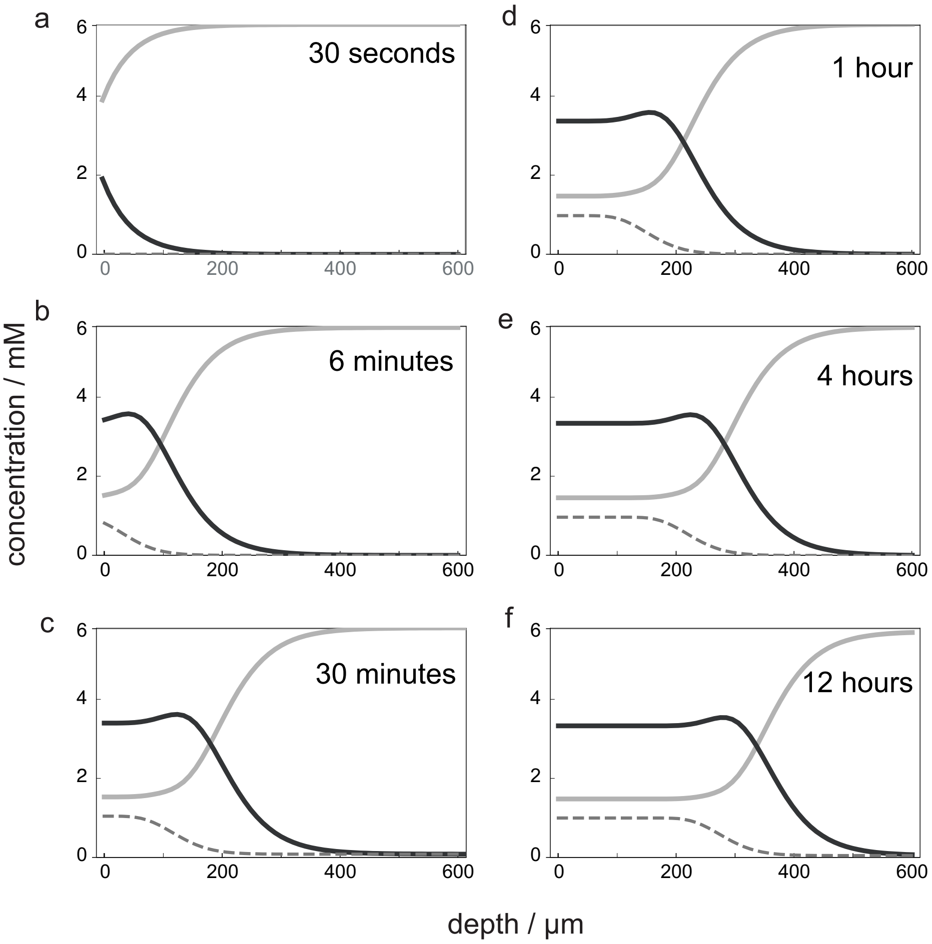

Fig. 5.4: Finite-element numerical simulations of photoisomerization in a sample containing 5.8 mM of rhodopsin, exposed to 0.75 μmol m^{-2} s^{-1} of monochromatic 420 nm light. The plots show the simulated concentrations of rhodopsin (solid grey line), bathorhodopsin (solid black line) and isorhodopsin (broken line) at the indicated times, as a function of depth below the surface (horizontal axis).

Although the isomerization layer becomes deeper in this case, the layer still contains the same number of isomerized molecules as before, since the chromophores are more dilute.

Experimental Results

Fig. 5.3c shows a DQF ^{13}C spectrum acquired after 12 hours illumination on an homogenous mixture of [9,10-^{13}C]-retynilidene-rhodopsin and glass beads (their role will be clearly explained in the next section) using a band pass filter with λ = 420 ± 5 nm. A small peak appears at 137.3 ppm (assigned to C10 of bathorhodopsin) and an even smaller peak appears at 131.4 ppm and is assigned to the C10 site of isorho-

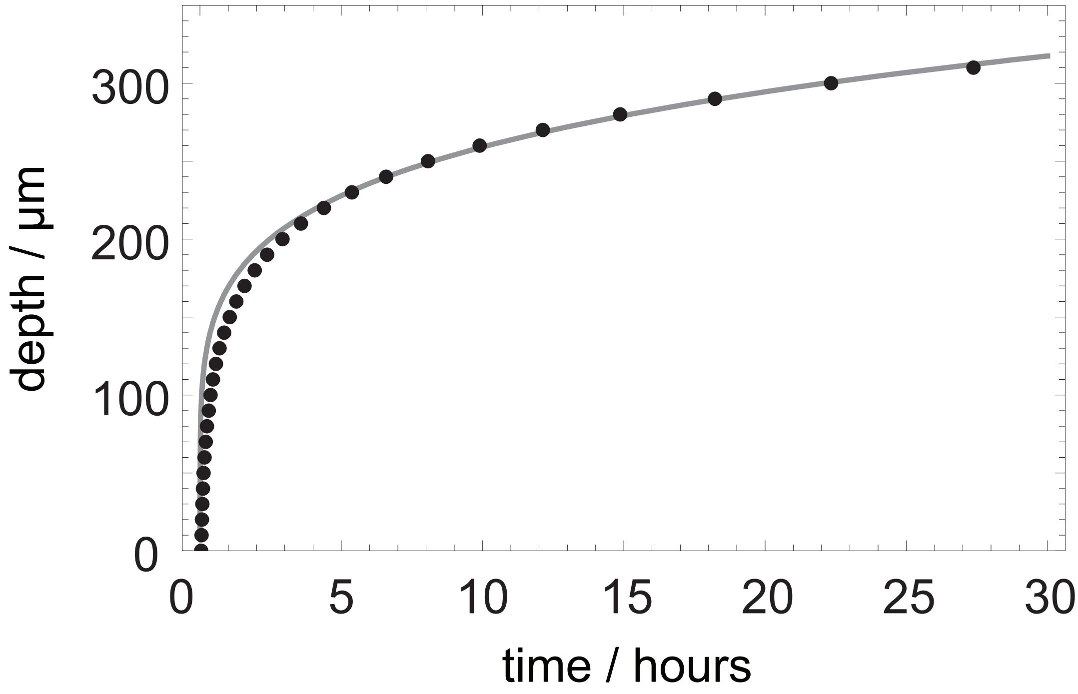

Fig. 5.5: Depth of the isomerization front as a function of time for 5.8 mM sample of rhodopsin, exposed to 0.75 μmol m^{-2} s^{-1} of monochromatic 420 nm light. The isomerization front is defined here by the position at which the concentration of bathorhodopsin falls below 2.9 mM. The filled symbols indicate the isomerization front positions, derived by numerical simulations. The solid line is a fit of the later time points to the form $z = at^{\alpha}$, where the best-fit exponent is α=0.184.

dopsin. The 137.3 ppm peak disappears, to be replaced by a broader and less distinct feature, when the sample temperature was raised above 130 K for about 30 minutes, before cooling again and acquiring the NMR data. This behaviour is consistent with its attribution to bathorhodopsin which, according to the photocycle in Fig. 1.7 is not stable at temperatures higher than 125 K . The clear decrease in intensity of the 127.9 ppm retinylidene-C10 peak in Fig. 5.3c indicates that the 137.4 ppm peak should be assigned to the retinylidene-C10 site of bathorhodopsin. The C9 peak of rhodopsin at 148.9 ppm is unchanged, which indicates that the retinylidene-C9 site of bathorhodopsin and rhodopsin have very close ^{13}C chemical shifts, that are not spectrally resolved. Spectra acquired on [9,10-^{13}C$_2$], [11,12-^{13}C$_2$], [12,13-^{13}C$_2$], [14,15-^{13}C$_2$] retinylidene rhodopsin are shown in Fig. 5.6.

In most cases, the relative intensities of the signals were enough to assign the new signals; remaining ambiguities in the assignments of the bathorhodopsin ^{13}C peaks could be resolved by comparing spectra from different isotopomers. The use

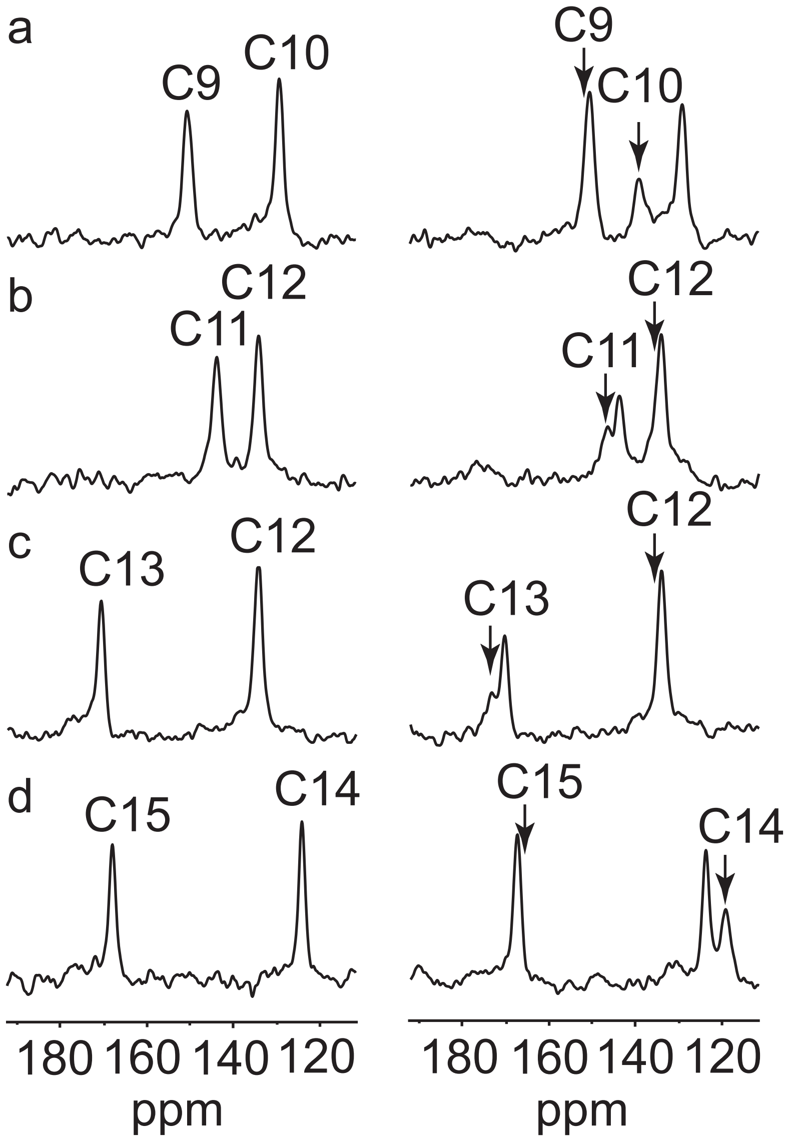

Fig. 5.6: Double-quantum-filtered ^{13}C NMR spectra of a) [9,10-$^{13}C_2$], b) [11,12-$^{13}C_2$], c) [12,13-$^{13}C_2$], d) [14,15-$^{13}C_2$] rhodopsin before (left) and after (right) 12 h of illumination with 420±5 nm light. All spectra were acquired at a temperature <120K with magic-angle spinning at 7.00±0.05 kHz. The positions of the bathorhodopsin signals are indicated by arrows.

of spectra of samples having one label in common confirmed and unambiguously assigned the generated bathorhodopsin signals. The bathorhodopsin yield was estimated to be about 35 % in all cases. Tab. 5.2 lists the isotropic ^{13}C chemical shifts of rhodopsin and bathorhodopsin as measured in our study. This part of the work has been published in Paper 2.

The 9.4 ppm isomerization shift of C10 is particularly striking. The isomer-

Tab. 5.2: Isotropic ^{13}C chemical shifts of rhodopsin δ_{rho} and bathorhodopsin δ_{batho} as found in this work. The last column shows the isomerization shift, $\Delta\delta=\delta_{batho}-\delta_{rho}$. All chemical shifts are referenced indirectly to TMS using the rhodopsin shift data in Ref. [10].

^{13}C site	δ_{rho}/ppm	δ_{batho}/ppm	$\Delta\delta$/ppm
C9	148.9	149.6	0.7
C10	127.9	137.3	9.4
C11	141.4	144.4	3.0
C12	131.8	132.8	1.0
C13	167.4	171.2	3.8
C14	122.3	117.5	-4.8
C15	165.4	164.4	-1.0

ization shifts tend to be in the deshielding direction (positive values) towards the beginning of the chain but in the shielding direction (negative values) at the end of the chain. An interpretation of the chemical shifts obtained has been done and published Paper 4 and it is here discussed in Sec. 5.2.5. A comparison between our results and previous NMR studies [12] is also discussed.

5.2.4 *Effect of Glass Beads*

After setting up illumination conditions such as exposure time, optical filters etc., the effect of glass beads has been explored on a sample of [9,10-^{13}C]-retinylidene-rhodopsin. Four isomerisation tests have been performed using four different rotor packing:

1. no glass beads inside the 4 mm thin wall rotor;
2. a mixture 2:1 of rhodopsin and glass beads centrifuged in the rotor at 8000 RPM for 5 minutes at 4 °C;
3. alternating layers of rhodopsin (kept frozen during the filling) and glass beads packed inside the rotor;
4. an homogeneous mixture of rhodopsin and glass beads according the procedure described in Sec. 4.2.2.

The chemical shifts were first measured in the dark at T = 120 K by spinning the sample with a frequency of $\omega_r/2\pi$ = 7 kHz (spectrum reported in Fig. 5.7a)

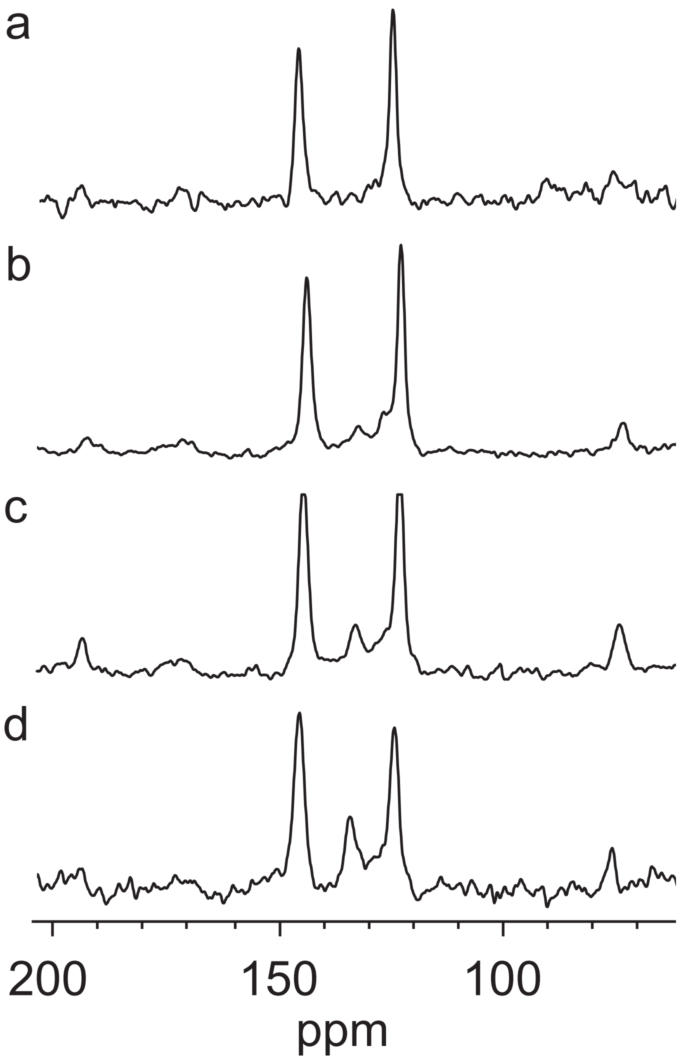

Fig. 5.7: All spectra refer to [9,10 $^{13}C_2$] retinylidene rhodopsin: a) DQ filtered spectrum before illumination (12 k scans); b) DQ filtered spectrum after 14 hours of illumination (12 k scans); c) DQ filtered spectrum of a sample made by alternating layers of rhodopsin and glass beads after 15 hours of illumination (12 k scans); d) DQ ltered spectrum of a sample made by rhodopsin and glass beads ground together at low temperature and after 12 hours of illumination (12 k scans).

In this same figure all the spectra recorded for each different rotor packing are reported for comparison. In the first isomerization test, the spectrum (Fig. 5.7b) shows evidence of the rhodopsin first photointermediate (bathorhodopsin) but the peak intensity is weak and not so much bigger than the spectral noise. In the second isomerization test (mixture of rhodopsin and glass beads centrifuged in the rotor - spectrum not shown) the signal is much lower than expected. These data suggest that centrifugation (even mild, 8000 RPM) can damage the sample when mixed with glass beads. Moreover the observed increasing of bearing and drive gas flows needed to spin the sample suggests that the rotor is not homogeneously packed. The rhodopsin/glass beads ratio may be lower at the bottom because of centrifugation. This method, thus, did not lead to any improvement. In the third attempt (layers of rhodopsin and glass beads), the DQ filtered spectrum (Fig. 5.7c) recorded after 14 hours of illumination shows peaks at the same position as found in the spectrum b) but with an increased intensity, although not as much as expected. This confirms that the glass beads can work as light “pipes” but also that a more homogeneous mixture should be done to improve significantly the amount of photointermediate to be prepared. In fact, a bigger improvement can be observed using this latter packing method: the peak at 134.7 ppm (Fig. 5.7d) is much larger than that in Fig. 5.7b and c.

The small intensity of the bathorhodopsin peak (Fig. 5.7b) is consistent with the high molar extinction coefficient of rhodopsin that, as discussed above, only allows a ∼300 μm outer layer of the sample to be reached by the light. By mixing the rhodopsin-rich particles with ∼100 μm diameter glass beads, the penetration of light into the interior of the sample was improved and hence the yield of bathorhodopsin was increased. The bead dimensions approximately match the size of the rhodopsin/lipid particles, as estimated by light microscopy. The dispersed glass beads, therefore, act as light guides, conducting the photons into the interior of the sample, and increasing the proportion of rhodopsin close to an illuminated surface.

5.2.5 Chemical Shift Comparison and Discussion

Experimentally measured chemical shifts of retinylidene-rhodopsin intermediates are reported in Tab. 5.3 to be compared to earlier values reported by Smith *et al.* [11, 12] and recent quantum calculations by Röhrig *et al.* [13] and Gascon *et al.* [14, 15].

Tab. 5.4 and Fig. 5.8 compare the isomerization shifts ($\Delta\delta = \delta_{batho}$-$\delta_{rho}$) calculated using our new data, earlier experimental data [11, 12] and quantum mechanical calculations [13, 14, 15]. Some features in the calculations of Ref. [13] do correlate well with the experimental results. For example the strong negative isomerization shift for C14 is well predicted by the calculations in [14, 15] and all calculations predict positive isomerization shifts for C10. However, the large magnitude of the

Tab. 5.3: Chemical shifts of the retinilydene chromophore of rhodopsin and bathorhodopsin from this work are compared with previous experimental data (Ref. [11, 12]) and QM calculations Ref. [13, 14, 15].

^{13}C	δ_{rho} /ppm (this work)	δ_{batho} /ppm (this work)	δ_{rho} /ppm [11]	δ_{batho} /ppm [12]	δ_{rho} /ppm [13]	δ_{batho} /ppm [13]	δ_{rho} /ppm [14]	δ_{batho} /ppm [15]
C9	148.9	149.6	148.5	-	141.6	143.2	149.1	150.8
C10	127.9	137.3	127.9	132.0	127.3	133.7	126.1	130.8
C11	141.4	144.4	141.6	140.0	132.9	131.7	138.6	137.9
C12	131.8	132.8	132.1	137.7	130.7	132.9	124.9	126.1
C13	167.4	171.2	168.9	168.5	155.3	156.9	162.2	158.7
C14	122.3	117.5	121.2	120.0	118.5	118.6	115.6	111.8
C15	165.4	164.4	165.4	163.4	146.8	146.5	153.5	153.9

Tab. 5.4: Experimental and theoretical isomerization shifts in bathorhodopsin ($\Delta\delta = \delta_{batho}$-$\delta_{rho}$).

	$\Delta\delta$ (ppm)			
^{13}C	This work	Smith et al. [11, 12]	Röhrig et al. [13]	Gascon et al. [14, 15]
C9	0.7	-	1.6	1.7
C10	9.4	4.2	6.4	4.7
C11	3.0	-1.6	-1.2	-0.7
C12	1.0	5.6	2.2	1.2
C13	3.8	-0.4	1.6	-3.5
C14	-4.8	-1.2	0.1	-3.8
C15	-1.0	-2.0	-0.3	0.4

isomerization shift for C10 is not predicted by calculations. The strong alternation of the isomerization shifts at positions C13 and C14 is also not well predicted.

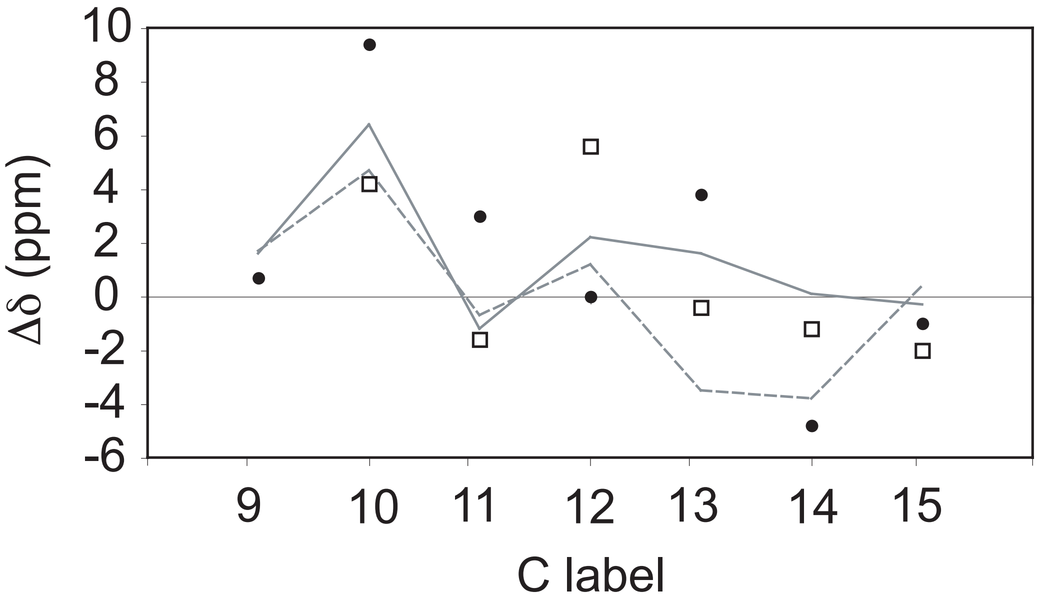

Fig. 5.8: Isomerization shifts in bathorhodopsin ($\Delta\delta = \delta_{batho}$-$\delta_{rho}$): data from this work (circles); from Ref. [11, 12] (open boxes); from Ref. [13] (solid line); and from Ref. [14, 15] (dashed line).

Strong deviation from previous NMR studies [12] are found in all the cases (Fig. 5.8). This is more evident in Fig. 5.9 where the ligation shifts, i.e. the change in chemical shifts between the free and the bound chromophore, calculated from

Ref. [12] are plotted as open boxes and compared to our data plotted as circles.

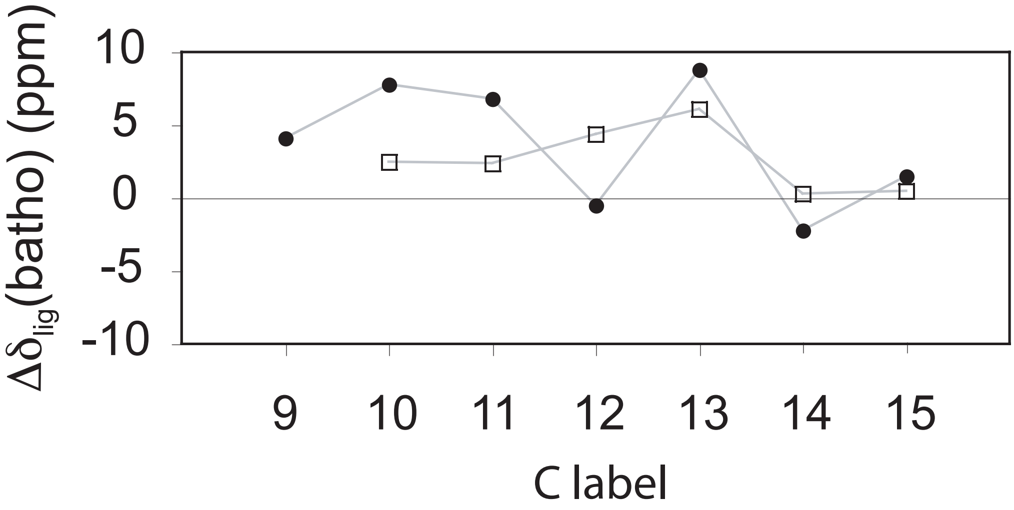

Fig. 5.9: Bathorhodopsin ligation shifts ($\Delta\delta_{lig}$ = δ_{batho}-$\delta_{all-E-PSB}$): data from this work (circles); and from Ref. [12] (open boxes).

Note that data from Ref. [12] show the largest difference (6.1 ppm) in chemical shift between bathorhodopsin and all-E-PSB model compound (i.e. the ligation shift) is found for C13. Small differences are also observed at positions C10, C11, and C12. The effects are almost equal in magnitude to those previously observed in rhodopsin suggesting that the electronic interactions between the protein and the chromophore were comparable between rhodopsin and bathorhodopsin. This is in contrast with our results which show much larger perturbation for all the ^{13}C chemical shifts (Fig. 5.9, circles).

This has been used to derive a tentative interpretation (Paper 4) which is based on the following evidence:

- *Comparison with PSB salts.* A first evidence comes from the comparison (see Tab. 5.5) of the isotropic chemical shift of rhodopsin and bathorhodopsin obtained in this study with retinylidene-PSB salts (RPSB). These latter have been commonly used in the literature as reference models to evaluate the influence of the protein environment on the retinylidene ligand [110, 34, 64, 109, 66, 12, 17]. In particular we employ All-E-(N-retinylidene)-propylimine chloride as a reference for the bathorhodopsin chromophore, and 11-Z-(N-retinylidene)-propylimine chloride as a reference for the rhodopsin chromophore (Fig. 5.10).

Tab. 5.5: Isotropic ^{13}C chemical shifts of rhodopsin δ_{rho} (I) and bathorhodopsin δ_{batho} as found in this work (II); changes in chemical shifts upon isomerization ($\Delta\delta_{isom}$(protein) = δ_{batho}-δ_{rho}) (III); isotropic ^{13}C chemical shifts of 11-Z-RPSB as found in [16] (IV); isotropic ^{13}C chemical shifts of All-E-RPSB as found in [16] (V); changes in chemical shifts from 11-Z to All-E ($\Delta\delta_{isom}$(solution)=δ_{All-E}-δ_{11-Z}) (VI); ligation shifts of rhodopsin $\Delta\delta_{lig}$(rho) = δ(rho)−δ(11-Z) (VII); ligation shifts of bathorhodopsin $\Delta\delta_{lig}$(batho) = δ(batho)−δ(All-E) (VIII)

	I	II	III	IV	V	VI	VII	VIII
^{13}C	δ_{rho} /ppm (This work)	δ_{batho} /ppm (This work)	$\Delta\delta_{isom}$ /ppm (Protein)	$\delta_{11-Z-RPSB}$ /ppm [16]	$\delta_{All-E-RPSB}$ /ppm [16]	$\Delta\delta_{isom}$ /ppm (Solution)	$\Delta\delta_{lig}$ /ppm (Rho)	$\Delta\delta_{lig}$ /ppm (Batho)
C9	148.9	149.6	0.7	146.6	145.5	-1.1	2.9	4.1
C10	127.9	137.3	9.4	126.4	129.5	3.1	1.5	7.8
C11	141.4	144.4	3.0	137.5	137.6	0.1	3.9	6.8
C12	131.8	132.8	1.0	129.1	133.3	4.2	2.7	-0.5
C13	167.4	171.2	3.8	162.7	162.4	-0.3	4.7	8.8
C14	122.3	117.5	-4.8	121.3	119.7	-1.6	1.0	-2.2
C15	165.4	164.4	-1.0	163.9	162.9	-1.0	1.5	1.5

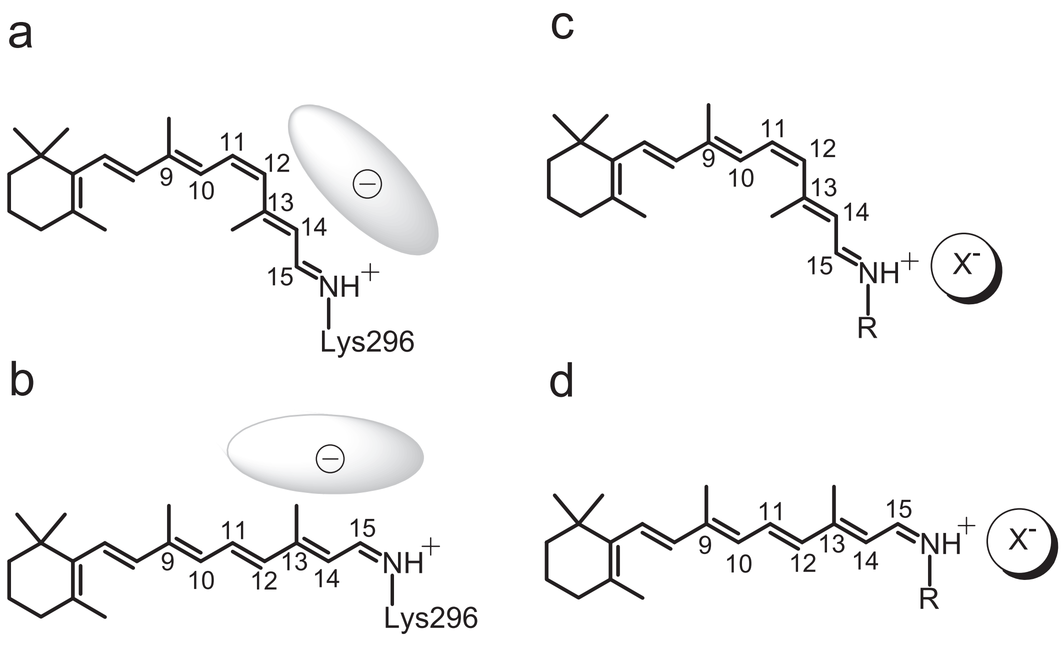

Fig. 5.10: Schematic structures of Retinylidene Protonated Schiff Base chromophores (RPSB) and their counterions in: (a) rhodopsin; (b) bathorhodopsin; (c) 11-Z-retinylidene-PSB model compounds; (d) All-E-retinylidene-PSB model compounds. R is an alkyl side chain and X^- a negatively charged counterion.

Fig. 5.11 shows a plot of the chemical shifts of rhodopsin and bathorhodopsin found in this work compared to 11-Z-RPSB chemical shifts [16] (values reported in Tab. 5.5 column IV) and All-E-RPSB [16] (values reported in Tab. 5.5 column V).

In all the cases, an alternating pattern where the odd numbered ^{13}C sites are less shielded than the even numbered one is evident. This is particularly relevant for the ^{13}C sites which are close to the positively charged nitrogen of the PSB. This pattern originates from a partial delocalization of the positive charge into the polyene chain [111, 112], the delocalized charge being stabilized on the odd numbered carbons. In turn, the partial stabilization of the positive charge on the odd numbered positions induces a small negative charge polarization on the even numbered positions via coulomb interaction [113]. Thus, the charge delocalization into the polyene chain induces downfield shifts (i.e. deshielding) of the odd numbered carbons and smaller upfield shifts (i.e. shielding) of the even numbered ^{13}C NMR signals of the retinylidene chain. Raw data in Fig. 5.11 clearly show:

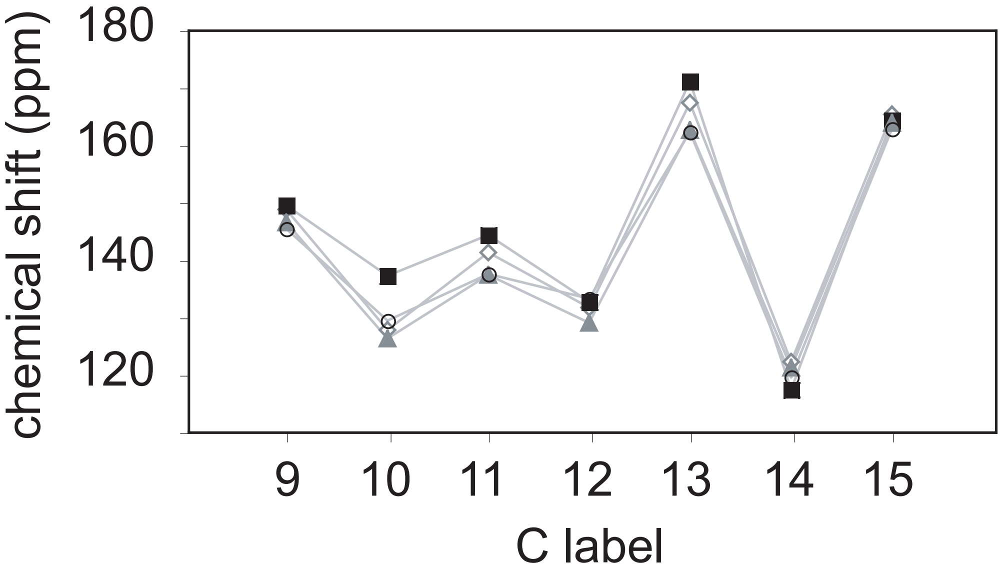

Fig. 5.11: ^{13}C chemical shifts of rhodopsin (open diamonds), bathorhodopsin (filled squares), 11-Z-RPSB (filled triangles), all-E-RPSB (open circles). The ^{13}C numbering is consistent with Fig. 5.10 with R = propyl and X^{-} = Cl^{-}. Numerical data are given in Tab. 5.5

a. a big shift in ^{13}C chemical shift of C10 (9.4 ppm) for bathorhodopsin;

b. deshielding of the odd numbered carbon chemical shift of bathorhodopsin with respect to rhodopsin.

In order to understand how the ligand properties are influenced by the interaction with the protein, an analysis of the isomerization shifts (change in ^{13}C chemical shifts upon isomerization) and ligation shifts (change in the ^{13}C chemical shifts induced in the ligand after settling in the binding pocket) is now attempted.

- *Comparison of isomerization shifts.* Isomerization shifts for retinal in $CDCl_3$ ($\Delta\delta_{isom} = \delta(all-E) - \delta(11-Z)$) are reported in Fig. 5.12a. Those occurring to retinylidene carbons when the retinal is bound to the opsin protein in the solid state at 120K ($\Delta\delta_{isom} = \delta(batho) - \delta(rho)$) are plotted in Fig. 5.12b:

  The isomerization patterns of the free and bound retinal are different. In solution (Fig. 5.12a), the isomerization has no significant effect on the odd positions, while the ^{13}C chemical shifts of the even positions close to the isomerization region are slightly shifted in the deshielding direction (downfield, 3-4 ppm). It appears that the geometrical change in configuration affects ex-

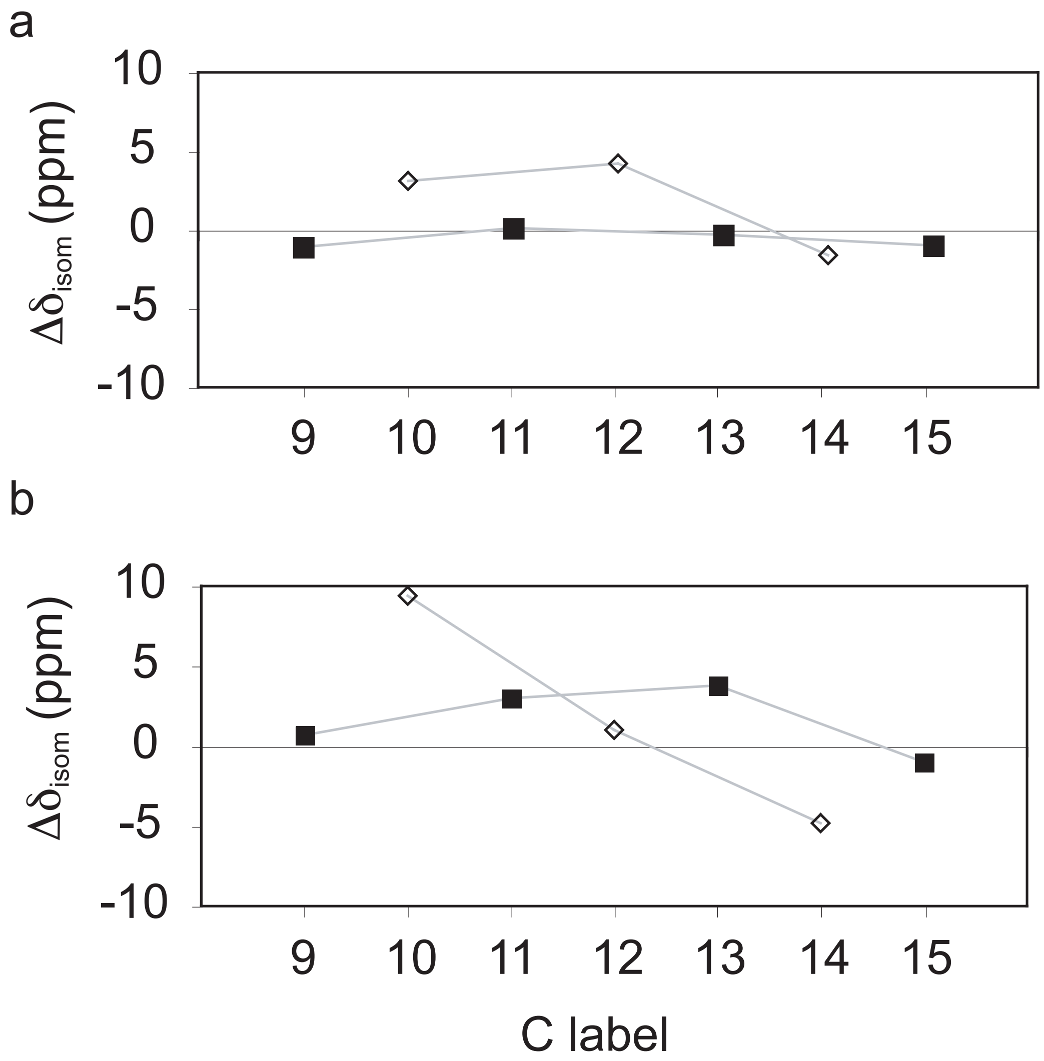

Fig. 5.12: a) ^{13}C isomerization shifts ($\Delta\delta_{isom}$ = δ(all-E)-δ(11-Z)) for protonated Schiff base model compounds in $CDCl_3$ solution. The compounds are given in Fig. 5.10c and d; b) ^{13}C isomerization shifts for the chromophore inside the protein ($\Delta\delta_{isom}$ = δ(batho)-δ(rho)). Filled squares indicate odd numbers while open diamonds indicate even numbers.

clusively the even ^{13}C sites. In the protein, (Fig. 5.12b), the picture is quite different: the isomerization influences both the even and the odd positions and, except for C15, all of them are shifted downfield, with C13 experiencing the biggest shift of 4 ppm. For the even positions: C14 is strongly shifted upfield while C10 is shifted by about 10 ppm in the deshielding direction (downfield). This indicates that the changes in ^{13}C chemical shifts after the photoisomerization from rhodopsin to bathorhodopsin cannot be explained just by configurational changes, and must also involve larger-scale changes in the conformation of the ligand and its interactions with the protein binding pocket.

- *Comparison of ligation shifts.* The values of the ligation shifts for rhodopsin ($\Delta\delta_{lig}$(rho) = δ(rho) – δ(11-Z-RPSB)) and bathorhodopsin ($\Delta\delta_{lig}$(batho) = δ(batho) – δ(all-E-RPSB)) are reported in Fig. 5.13a and b, respectively.

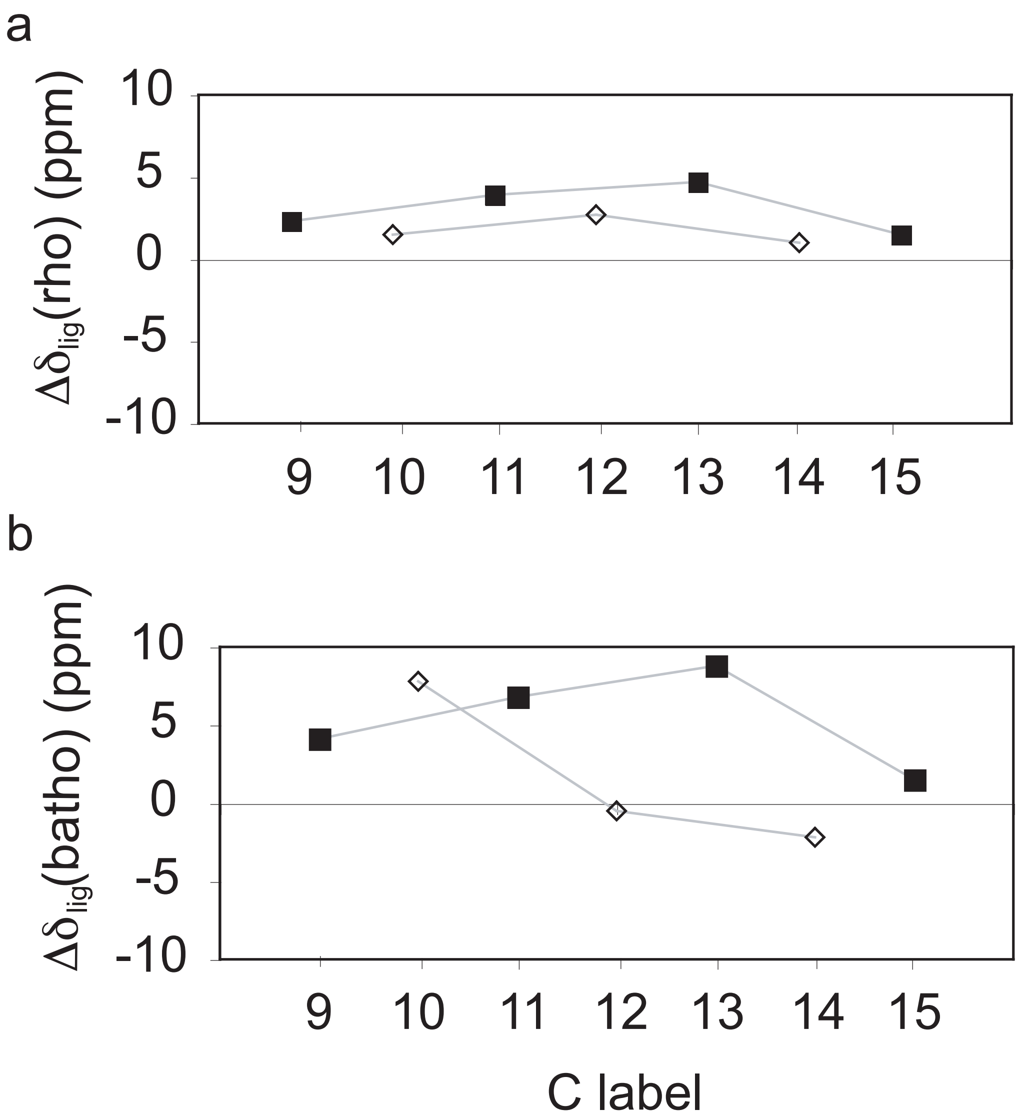

Fig. 5.13: ^{13}C ligation shifts for a) rhodopsin ($\Delta\delta_{lig}$(rho) = δ(rho)-δ(11-Z-free)) and b) bathorhodopsin ($\Delta\delta_{lig}$(batho) = δ(batho)-δ(all-E-free)). Filled squares indicate odd number while open diamonds indicate even number.

The reference 11-Z-RPSB model used in Fig. 5.13a refers to Fig. 5.10 with R = propyl and X = Cl$^-$, in $CDCl_3$ solution. The reference used in Fig. 5.13b is the corresponding all-E-RPSB.

The understanding of these number is surely linked to the possible origin of the ligation shifts. These may be due to: i) protein/ligand electrostatic interactions; and/or ii) geometrical changes of the polyene chain induced by steric interactions between the ligand and the opsin pocket. As explained earlier, the increase of positive charge delocalization on the odd numbered carbons is expected to induce small upfield ligation shifts on the even ^{13}C positions. Nevertheless, this does not apply to the ligation shifts in rhodopsin: the even ^{13}C ligation shifts are all shifted downfield (with C12 experiencing the biggest shift of about 3 ppm - Fig. 5.13). Semiempirical molecular orbital calculations [18] suggested that the anomalous downfield ligation shifts of the even carbons in rhodopsin can be reproduced by placing a carboxylate oxygen 3.0 *Å* above carbon C12, in agreement with early NMR data [114]. In later NMR distance measurements [110], ab-initio modelling [75], and QM/MM calculations [115] this idea was modified towards a more complex type counterion spread over a hydrogen bonded network running along the whole polyene chain. On the hypothesis of geometrical changes some authors [18] suggested that the anomalous downfield shifts observed in rhodopsin data (Fig. 5.13a) cannot simply be attributed to a change in the C11-C12-C13-C14 torsional angle but that a charge mechanism is also involved. This is, however, at variance with data reported in Fig. 5.12a where an even larger downfield shifts on even-numbered ^{13}C is observed in the case of 11-Z/all-E isomerization in solution where no charge mechanism is surely involved. Hence it cannot yet be ruled out that these shifts could originate from distortions in the rhodopsin polyene chain. In bathorhodopsin the ligation pattern for the even numbered ^{13}C sites changes drastically. Consistently with an increased charge delocalization C14 and C12 experience the expected small upfield ligation shifts, but this time C10 experiences a striking and unexpected 8 ppm downfield ligation shift. It seems that the perturbation that affected all the even numbered positions in rhodopsin, after isomerization focuses its effects exclusively on C10. We tentatively attributed this to a localized strong torsion of the polyene in the C10 region, but we cannot yet exclude that a modification of the complex counterion network in bathorhodopsin would produce a similar effect.

- *Other observations.* It has been shown on series of RPSB compounds that the odd numbered ^{13}C chemical shifts along the retinylidene chain are sensitive to the nature and position of the counterion. The strength of the counterion (i.e. the magnitude and degree of localization of the negative charge) modulates the penetration of the PSB positive charge into the polyene. For example, a strong negatively charged counterion stabilizes positive charge in its proximity [113]. The delocalized positive charge is stabilized on the odd numbered carbons, so for reduced PSB/counterion interactions, the positive charge is less restricted to the nitrogen of the PSB, shifting the odd numbered carbons in the deshielding direction (downfield). The odd-numbered-^{13}C chemical shift data in Fig. 5.12, therefore, suggests that the penetration of positive charge into the polyene chain is increased for bathorhodopsin relative to rhodopsin, and that this positive charge has a tendency to be located in the vicinity of C13, in both cases.

It has been found that the summed ^{13}C chemical shifts of the odd-numbered polyene carbons in retinylidene model compounds have a linear relationship with the frequency of maximum optical absorption, ν_{max}, and that the ^{13}C chemical shifts in rhodopsin adhere to the same relationship [111]. This relationship is attributed to the fact that the penetration of positive charge from the PSB into the polyene chain influences the chemical shifts of the odd-numbered ^{13}C sites, as discussed above, and simultaneously modulates the HOMO-LUMO gap [112]. The degree of positive charge penetration is influenced by the nature of the negative counterion. The relevant correlation is shown in Fig. 5.14 in which the frequency of maximum optical absorption ν_{max} is plotted against $\sum_{\delta}^{odd}$, the summed ^{13}C chemical shift for the odd-numbered carbons (C9, C11, C13 and C15) of several (11-Z)- and (all-E)-retinylidene compounds in solution.

As discussed in [111], the optical properties and ^{13}C chemical shifts of rhodopsin fit on the same straight line as the retinylidene model compounds. The position of the rhodopsin data (point K) suggests that the counterion in rhodopsin is weaker and more diffuse than for any of the PSB model compounds, leading to a higher penetration of the positive charge into the polyene chain, which gives rise, in turn, to relatively strong deshielding shifts for the odd-numbered ^{13}C sites as well as a strong bathochromic shift (red shift)

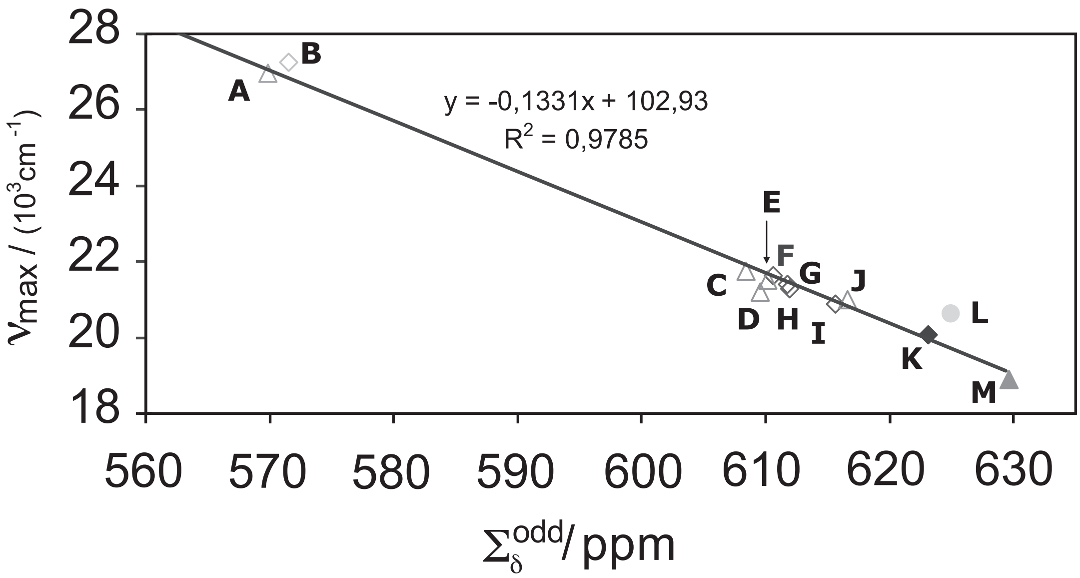

Fig. 5.14: The frequency of maximum visible absorption ν_{max} plotted against the sum of the C9, C11, C13 and C15 chemical shifts of: (A) unprotonated all-E-SB with R = propyl [16]; (B) unprotonated 11-Z-SB with R = propyl [16]; (C) all-E-PSB with R = propyl, X^- = Cl^- [16]; (D) all-E-PSB with R = tert-butyl, X^-=$ClO_4{}^-$ [11]; (E) all-E-PSB with R = tert-butyl, X^-=$ClF_3SO_3{}^-$ [17]; (F) 11-Z-PSB with R = propyl, X^-=Cl^- [16]; (G) 11-Z-PSB with R = propyl, X^- = Br^- [18]; (H) 11-Z-PSB with R = tert-butyl, X^-=$ClO_4{}^-$ [17]; (I) 11-Z-PSB with R = propyl, X^- = F_3AcO^- [16]; (J) all-E-PSB with R = butyl, X^- = $CF_3SO_3{}^-$ [17]; (K) rhodopsin; (L) isorhodopsin [19]; (M) bathorhodopsin. The line is the linear least-squares fit to points A, B, C, D, E, F, G, H, I, J, K, M.

upon ligation. As shown in Fig. 5.14, the new bathorhodopsin data (point M) follow this correlation too, but with an even more extreme bathochromic optical shift and corresponding influence on the ^{13}C chemical shifts for the odd-numbered sites. This strongly suggests that the stabilizing influence of the negative counterion on the positive charge of the protonated Schiff base, which is already relatively weak for rhodopsin, is reduced even further for bathorhodopsin. This also suggests that the bathochromic shift is due to changes (weakening) in the counterion strength. The weakening of the counterion could originate from an increased dispersion of its negative charge inside the H-bonded network running along the polyene chain (e.g. by stronger contribution of the Glu181 residue). The X-ray structure of bathorhodopsin [1, 53] suggests a small displacement (0.03Å) of the Glu113 counterion away from the positively charged Schiff base nitrogen, which may contribute to a weakening of the counterion. This would further increase the penetration of the positive charge into the polyene chain. Point L represents the 9-Z isomer, i.e. isorhodopsin. It displays an optical shift that is slightly out of line with the sum of the odd-numbered ^{13}C shifts of the other chromophores. A potential explanation has been reported [109], but a higher resolution crystal structure than currently available [19] and detailed quantum calculations are required to better explain this anomaly.

Previous NMR chemical shift studies suggested that a complex counterion network in the protein could be mainly responsible for the ligation shifts of the rhodopsin chromophore (Fig. 5.13a) [111, 116, 18]. An empirical relationship between ν_{max} and the PSB/counterion distance [116, 117, 118] was established for a series of (11-Z) and (all-E)-RPSB compounds. Accordingly, the effective centre-to-centre distance between the PSB nitrogen and the counterion can be estimated to 0.55 ± 0.01nm for bathorhodopsin and 0.44 ± 0.01nm for rhodopsin. Since these effective distances are larger than the Glu113-oxygen/PSB-nitrogen distance derived from the published crystal structures (0.39 nm for bathorhodopsin and 0.36 nm for rhodopsin) [1, 53], this contributes to converging evidence for a complex type of counterion which would be centred further away from the PSB-nitrogen in bathorhodopsin. This distance increase would cause the protein to undergo a dielectric response after photoisomerization and thus it would contribute to the energy storage inside the bathorhodopsin chromophore by a charge separation mechanism.

5.2.6 Summary of Findings

In this brief section I summarize the complicate reasoning above:

Our observations:

Oa. In bathorhodopsin the odd number ^{13}C chemical shifts are deshielded with respect to rhodopsin (Fig. 5.11);

Ob. The isomerization shifts of the free and bound retinal are different (Fig. 5.12);

Oc. Looking at chemical shifts of the even carbons in bathorhodopsin: C12 and C14 experience a small upfield ligation shift; C10, instead, experiences a big downfield ligation shift (8 ppm) (Fig. 5.13);

Od. The ^{13}C chemical shifts of bathorhodopsin adhere to the linear relationship between the sum of the odd number chemical shifts and the frequency of maximum optical absorption, ν_{max} (Fig. 5.14). Our data are. therefore, in agreement with UV/Vis observations.

Our conclusions:

Ca. The positive charge on the PSB-nitrogen is more delocalized in bathorhodopsin than in rhodopsin.

Cb. The ion-counterion interaction is weaker in bathorhodopsin than in rhodopsin. Note that Ca and Cb are correlated. The delocalization of the positive charge on the odd carbons of the polyene chain produces a deshielding of the odd carbon chemical shifts from an NMR point of view and a reduced HOMO-LUMO gap. Both of these phenomena have been observed (Oa and Od);

Cc. A change in the conformation of the chromophore and its interaction with the protein is compatible with point Ob;

Cd. The big downfield ligation shift for C10 may be due to a localized distortion of the polyene chain. However, the hypothesis of a complex counterion cannot be excluded;

The most general conclusion is that the new bathorhodopsin NMR data indicates that both electrostatic interactions and steric strain are involved in the energy storage mechanism of bathorhodopsin.

5.3 *Torsional Angle Measurements*

To further investigate the steric strain contribution evidenced by the chemical shift analysis above, the measure of torsional angles in rhodopsin and bathorhodopsin was set up and performed. Experiments were carried out on a sample of [11,12-^{13}C$_2$]-retinylidene rhodopsin in order to measure the H-^{13}C11=^{13}C12-H dihedral angle, i.e. around the double bond where the isomerization takes place. This torsional angle is supposed to be around 0° (distorted-*cis*) in rhodopsin. The isomerization produces an *all-trans* configuration for the retinal in bathorhodopsin. Moreover, isorhodopsin, the 9-*cis*-retinylidene version of rhodopsin (which could also be easily produced in our equipment by the correct wavelength selection - see Sec. 4.2.2) is expected to have a nearly *trans* configuration around the C11-C12 double bond. Therefore, in order to assess the credibility of these torsional angle measurement data on both bathorhodopsin and isorhodopsin have been acquired and analyzed.

These experiments have been done using the pulse sequence discussed in Sec. 3.4. However, since this is a modified version of the original procedure [94], a model compound was used to test the new method and estimate the confidence level.

5.3.1 Model Compound: 2,3-Diammonium-$^{13}C_2$-fumarate

The compound chosen to test the torsional angle measurements was 2,3-Diammonium-$^{13}C_2$-fumarate (DAF, see Fig. 5.15).

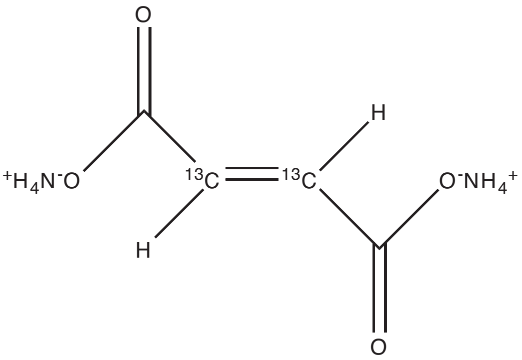

Fig. 5.15: Molecular structure of Diammonium 2,3-$^{13}C_2$-fumarate (DAF).

The choice was driven by the fact that DAF is expected to have a H-C=C-H torsional angle very close to 180° and, at the same time, to give a quite strong signal. The objectives of this test are: i) to confirm that the new method effectively works; ii) to check wether or not there are differences in the way the H-H interactions are decoupled and iii) to have a rough estimate of the confidence interval on the value of the measured torsional angle. The results of these tests can be summarized as follows:

- there are no significant differences in the use of FSLG (triangles) or PMLG (boxes) as homonuclear recoupling scheme (see Fig. 5.16a);
- both FSLG (Fig. 5.16b) and PMLG (Fig. 5.16c) compare quite well with simulations done with SIMPSON [119] by reproducing the same pulse sequence and inferring a torsional angle of 175°;

- the sequence is able to clearly distinguish ±5° in the torsional angle (see Fig. 5.16b and c). However, this is subject, as we will see later, to the quality of the acquired data that in this test case is very good.

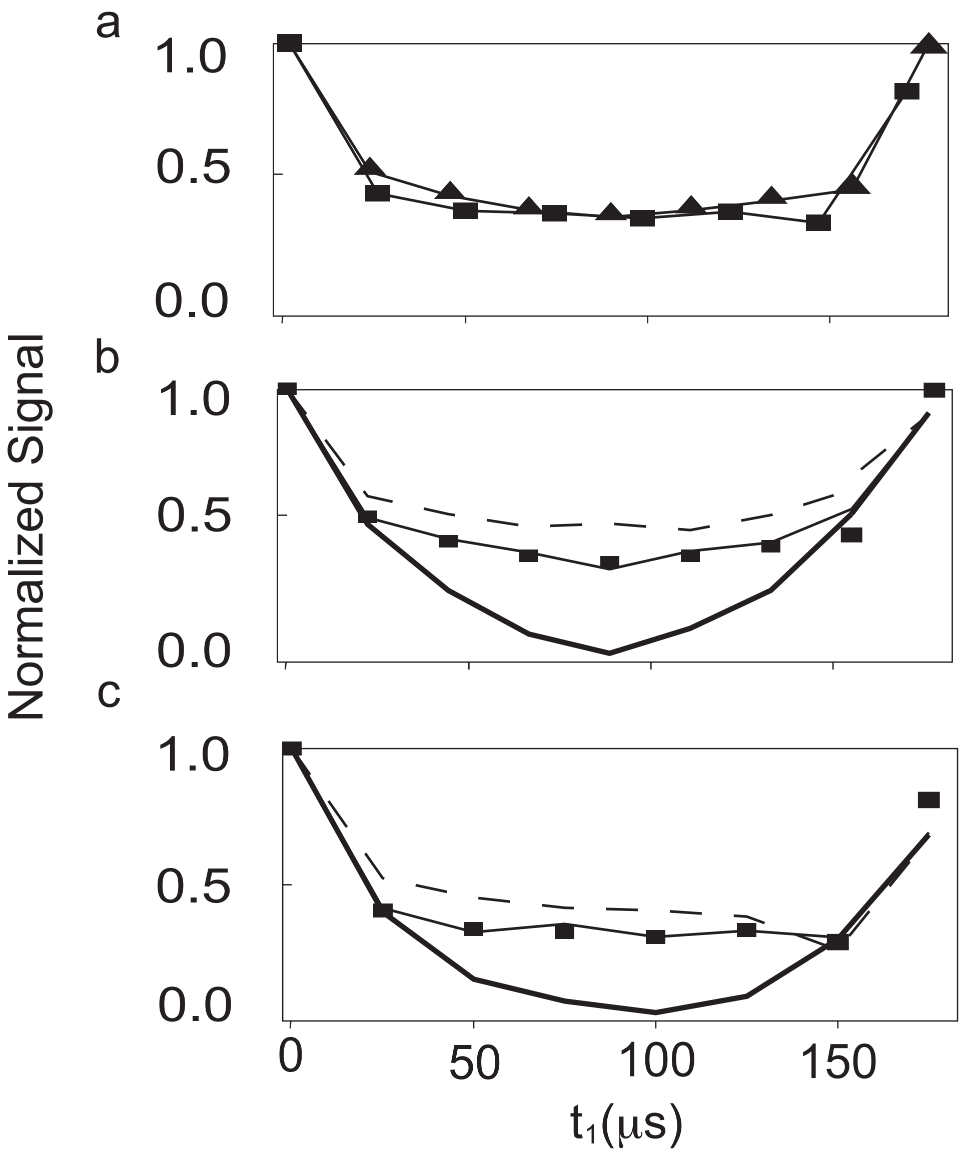

Fig. 5.16: (a) Experimental double quantum filtered signal amplitudes as a function of t_1 obtained on DAF using the pulse sequence in Fig. 3.5 with FSLG (triangles) and PMLG (boxes) as homuclear decoupling scheme. Experimental results (symbols) using PMLG (b) or FSLG (c) as homonuclear decoupling are compared with simulations (lines). Thick solid line were obtaining inferring a torsional angle of 170°; thin solid line refers to the 175° case; and dashed line refers to the 180° case.

Note that SIMPSON simulations were necessary since an analytical equation for the dependence of the signal amplitude from t_1 is not available for the pulse sequence in Fig. 3.5. These simulations uses the spin system parameters available from [94]. The signal amplitudes were calculated as the integral of ^{13}C peaks in the experimental DQF spectra. The experiments were done at a field of $B_0 = 9.4$ T and spinning the sample at $\omega_r/2\pi = 5.6$ kHz. The experimental DQ efficiency was around 40%. The proton nutation frequency during the homonuclear decoupling was 80 kHz in both cases. The mismatch between this result and a simplified description of a fully planar molecule ($\phi = 180°$) may be justified accounting for: i) additional protons on neighboring molecules; ii) rf inhomogeneity; iii) non-uniform cross-polarization.

5.3.2 *Measurements on [11,12-$^{13}C_2$]-retinilydene-rhodopsin*

With the announced aim of detecting possible torsional strain after the isomerization of rhodopsin, we investigated [11,12-$^{13}C_2$]-retinilydene-rhodopsin before and after the formation of bathorhodopsin was triggered by illumination (see Sec. 4.2.2). Despite the large number of scans acquired (limited by the possible length of the overall experimental section and by the fact that the sample is “wasted” after illumination - reconstitution is possible but tedious), the quality of spectra so acquired is quite bad. However, since the position of peaks is known from the chemical shift measurements above, a reconstruction procedure is possible. This procedure summarized as follows:

- *Simulations*

  The procedure starts with the collection of the simulated torsional angle measurements calculated at different values of the torsional angle under investigation. Simulations have been done using the software SIMPSON and the following parameters:

  - isotropic chemical shifts (δ^{iso}) taken from recorded spectra (see above);
  - anisotropic chemical shifts (δ^{aniso}) and asimmetry of the chemical shift tensor (η) assumed equal to rhodopsin (from Ref. [120]);
  - dipolar couplings (b_{jk}) assumed equal to rhodopsin (from Ref. [120]);
  - orientations: 2000 (α, β) angle pairs chosen according to the repulsion scheme REP2000 [119] and 30 equally spaced values of γ;
  - spinning speed (ω_r) and powers have been set to match the values used in the experiments;

- Euler angles for the dipolar interactions at the selected values of the torsional angle have been calculated using the routines available in mPackages [91] and assuming the regular geometry $r_{CC} = 1.34\,\AA$, $r_{CH} = 1.1\AA$, $HCC = 120^\circ$.

A series of 19 simulations have been done varying the torsional angle between 0° and 180° in steps of 10° (see Fig. 5.17). In each of them t_1 run from 0 to $\tau_r = 1/7000 = 142\mu$s.

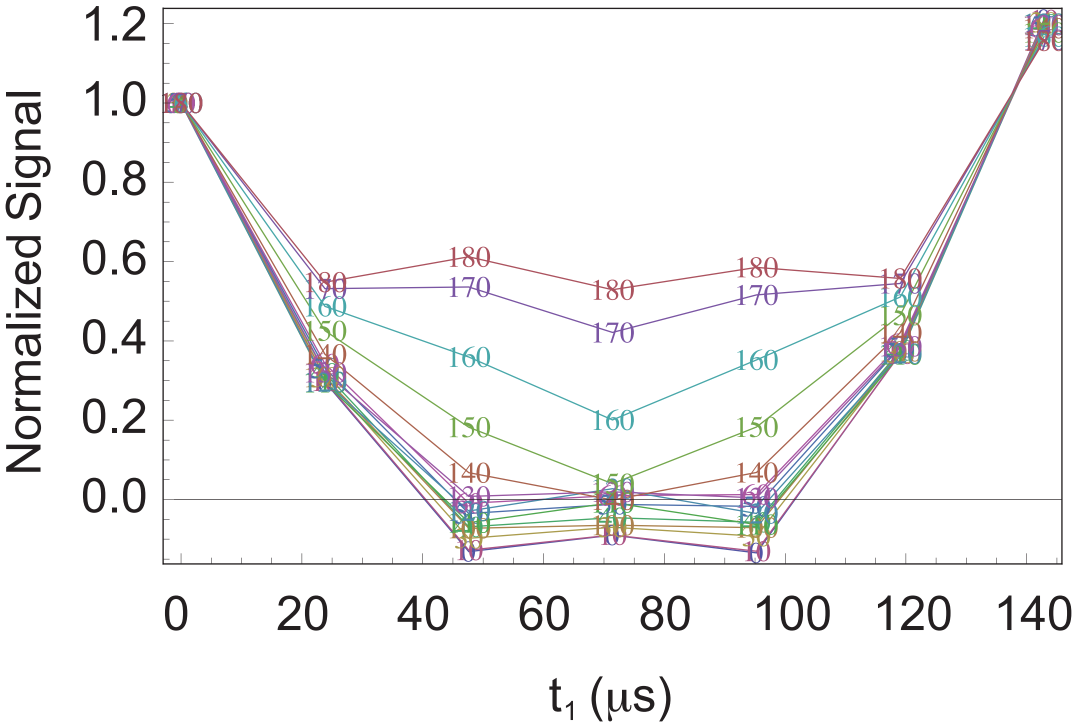

Fig. 5.17: SIMPSON simulation of the pulse sequence in Fig. 3.5 and for a sample of [11,12-$^{13}C_2$]-retinilydene-rhodopsin. The H-C11=C12-H torsional angle (ϕ) was varied between 0° and 180° in steps of 10° (the value is explicitly indicated on each curve). For each curve the time delay (t_1) run from 0 to $\tau_r = 1/7000 = 142\mu$ s and the molecular parameters used in the simulations are reported above.

This plot shows that the dependence on ϕ is weak for ϕ below $\sim 140^\circ$. Therefore, the pulse sequence performed better in probing near-*trans* geometry around double bonds, in the case of rhodopsin. It is suitable for bathorhodopsin, having a near-*trans* conformation, but cannot discriminate in the case of rhodopsin, where the retinal is known to be in a near-*cis* configuration.

- *Experiments*

The experiments on the bathorhodopsin isomer start with illumination, at 420 nm and 120 K for 12 hours, of a sample of [11,12-$^{13}C_2$]-retinilydene-rhodopsin. To check the presence of bathorhodopsin and estimate its concentration, a double-quantum filtered NMR spectrum was also acquired (Fig. 5.18).

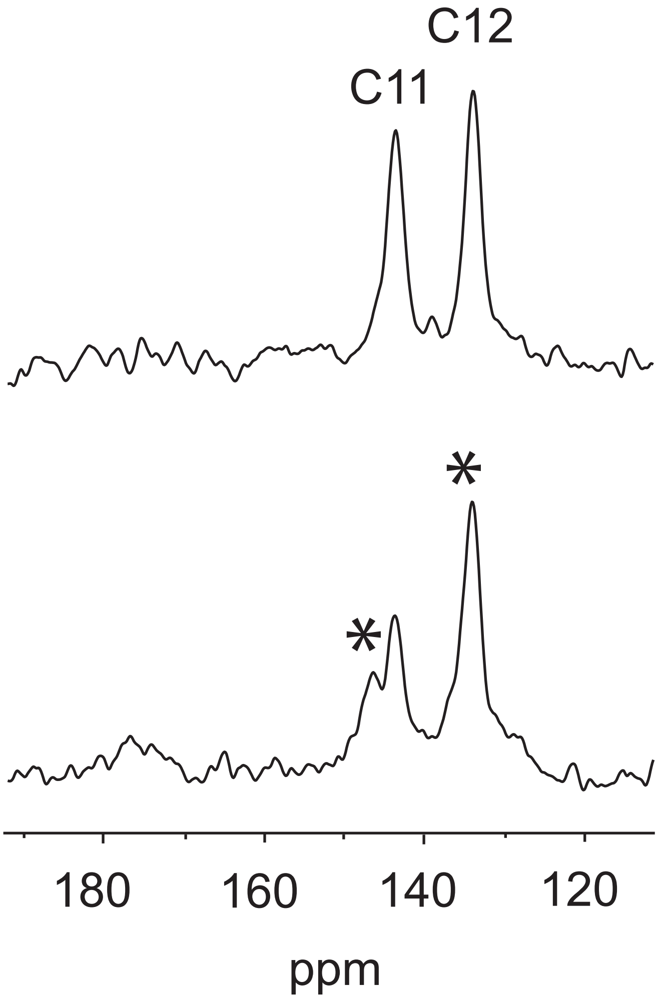

Fig. 5.18: Double quantum spectrum of [11,12-$^{13}C_2$]-retinilydene-rhodopsin after illumination at 420 nm for 12 hours and at 120 K confirming the presence of the bathorhodopsin isomer (peaks indicated by asterisks).

It shows a peak at 144.4 ppm which is attributed to C11 of bathorhodopsin confirming the production of this photointermediate with an yield of about 35%. The sequence described to measure torsional angles was then applied to the illuminated sample containing the mixture of rhodopsin and bathorhodopsin. Seven points have been collected by equal increments of t_1 (time delay) from 0 to $\tau_r = 2\pi/\omega_r$ ($\omega_r/2\pi$ =7000 Hz). Each point is the sum of 5632 transients acquired with a repetition time of 5 s. The recoupling sequence $R20_2^9$ was optimized to maximize the double quantum efficiency.

- *Data handling*

  To cope with the bad quality of the recorded spectra, the data were handled according to the following method:

  1. A signal masking function is produced;
  2. Integrals of the overlapping peaks are resolved;
  3. Experimental noise is estimated;
  4. Simulations are fitted to experimental points.
  5. 68% confidence interval is estimated using a χ^2 analysis

  Step by step:

  1. Since the peak position is well known from the DQF experiment, a noise-free spectrum can be obtained by multiplying each spectrum by four Lorentians centered at the peak positions and whose width match the experimental ones. The masking function ($S^{nf}(\omega)$) is given by:

     $$\begin{aligned} S^{nf}(\omega) &= \sum_{i=1}^{4} S_i^{nf}(\omega) \\ S_i^{nf}(\omega) &= S^{exp}(\omega) L(\sigma_i, \omega_i^0) \end{aligned} \tag{5.1}$$

     where $S^{exp}(\omega)$ is the experimental spectrum and $L(\sigma_i, \omega_i^0)$ is a Lorentian function centered at the frequency ω_i^0 whose width is σ_i.

  2. Peaks overlap in pairs and, therefore, the correct peak area (A_i) has to be determined using a standard deconvolution procedure. $S^{exp}(\omega)$ is written as a sum of Lorentians weighted by the coefficients c_i and centered at the frequency of the two peaks (i.e. ω_1^0 and ω_2^0). Their widths (σ_1 and σ_2) were chosen to match the experimental value.

     $$S^{exp}(\omega) = c_1 L(\sigma_1, \omega_1^0) + c_2 L(\sigma_2, \omega_2^0) \tag{5.2}$$

     Indicating with I_i the integral of one peak in the masking function,

     $$I_i = \int_{-\infty}^{+\infty} S_i^{nf}(\omega) \tag{5.3}$$

the area of each peak is known if c_1 and c_2 are known. They cab be calculating by solving:

$$\begin{pmatrix} c_1 \\ c_2 \end{pmatrix} = X^{-1} \begin{pmatrix} I_1 \\ I_2 \end{pmatrix} \tag{5.4}$$

with

$$X = \begin{pmatrix} L_{ii} & L_{ij} \\ L_{ji} & L_{jj} \end{pmatrix} \tag{5.5}$$

and

$$L_{ij} = \int_{-\infty}^{+\infty} L(\sigma_i, \omega_i^0) L(\sigma_j, \omega_j^0) \tag{5.6}$$

3. Experimental error bars (EB) on peak areas were derived from spectral noise. The RMS of the areas of a sum of 50 Lorentians centered in a region where there is only noise ($\omega_i^{\prime 0}$) and with a width (σ) which is the average of the four peaks' width used, was used for the purpose.

$$EB = \sqrt{\frac{1}{N} \sum_{i=1}^{N} \left(\int_{-\infty}^{+\infty} S^{exp}(\omega) L(\sigma, \omega_i^{\prime 0}) \right)^2} \tag{5.7}$$

4. SIMPSON simulations were fitted to experimental points. Since it is more difficult to perform good-quality homonuclear decoupling compared to heteronuclear decoupling, damping of coherences is probably stronger during PMLG. In order to allow for this damping of the signal during the t_1 in which PMLG is applied an exponential decay was added:

$$I_i^{sim*}(\omega) = k_i e^{-\lambda_i t_1} I_i^{sim} \tag{5.8}$$

   where k_i is a scaling factor, λ_i the damping time constant and I_i^{sim} represents a given point in the SIMPSON simulated curve (signal amplitude versus t_1).

   The experimental signal areas (A_i) calculated as in points 1 and 2, with error bars obtained as in point 3, were compared with the damped SIMPSON simulations (I_i^{sim*}) obtained varying the torsional angle from 0° to 180° in steps of 10°.

5. According to statistical analysis, about the 68% confidence on a given

fitted value is contained in the interval between χ^2 and χ^2+1, where the χ^2 is defined as:

$$\chi^2 = \sum_{i=1}^{n} \frac{1}{\sigma_i^2} \left[I_i^{exp} - I_i^{sim*} \right]^2 \tag{5.9}$$

where n is the number of measured data points, σ_i the noise variance for each point, I_i^{exp} the integral of the experimental spectrum at the i-th value of t_1 and I_i^{sim*} the corresponding simulated value. Plots of χ^2 versus the torsional angle ϕ have been done to spot the values of ϕ within this confidence interval.

- *Results*

  Fig. 5.19 shows the experimental integrated amplitudes as a function of the evolution interval t_1 (filled circles) and the best-fit simulations (lines) for values of torsional angle from 0° to 180° in the case of bathorhodopsin.

  The experimental points are well fitted for values of ϕ between 0° to 140° as it is clearly indicated in the χ^2 plot versus ϕ reported in Fig. 5.20.

  Even if the result is not unique, the data are consistent with a deviation from the planarity of at least 40° around the C11=C12 double bond.

  The same procedure may be applied to rhodopsin by integrating peaks corresponding to this isomer. These results are plotted in Fig. 5.21.

  The experimental points are well fitted for all values of the angles as it is evident in the χ^2 plot versus ϕ reported in Fig. 5.22.

  This is consistent with the fact that the sequence is not able to give a unique solution for near-*cis* geometries due to the small dependence of the sequence from the torsional angle at these geometries and to the considerable experimental error bars obtainable in these kind of compounds.

Measurements on [11,12-$^{13}C_2$]-retinilydene-isorhodopsin

The same torsional angle ϕ was measured for the isorhodopsin isomer. The production of isorhodopsin has been achieved by illuminating a sample of [11,12-^{13}C$_2$]-retinilydene-rhodopsin at 560 nm for 12 hours at 120 K. A Double-quantum filtered NMR spectrum shows the success in producing isorhodopsin by showing two extra peaks attributed to isorhodopsin-C11 and isorhodopsin-C12 (see Fig. 5.23).

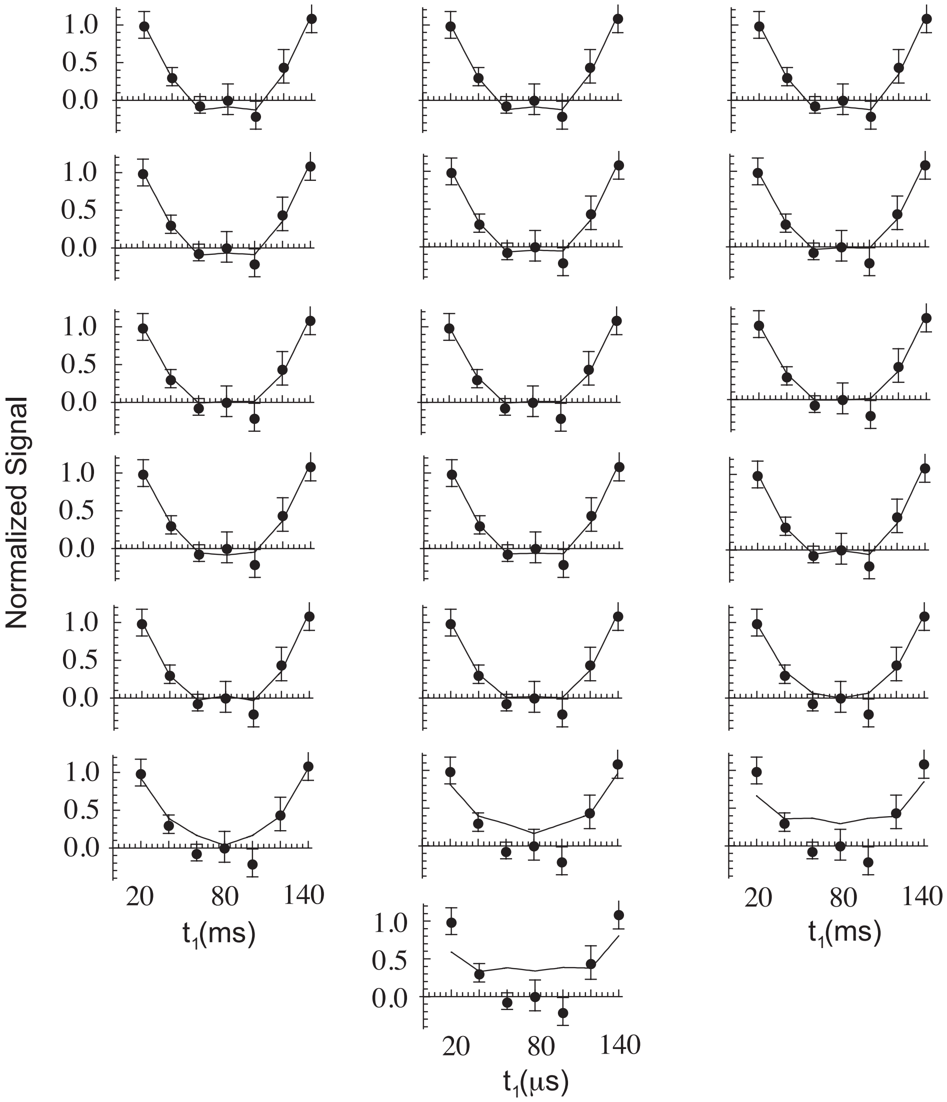

Fig. 5.19: Experimental normalized signal intensities (circles) and error bars as obtained for [11,12-$^{13}C_2$]-retinilydene-bathorhodopsin compared with SIMSON simulations (lines). The same experimental points are reported in each plot and compared to simulations at various values of the H-C11=C12-H torsional angle, ϕ. Plot refers to values of ϕ from 0° to 180° in steps of 10° from left to right and top to bottom.

The H-C11=C12-H torsional angle has been measured as above. This time, eight points have been collected by equal increments of t_1 from 0 to τ_r (spinning at 7 kHz). Each point is the sum of 8 k transients taken with a repetition time of 5 s.

The same data handling procedure as before was used here and the fitting between simulations and experimental data are reported inFig. 5.24.

The best fit corresponds to a value of $\phi = 180°$ with $\phi = 170°$ also possible within a probability of about 68% as comes from the χ^2 analysis in Fig. 5.25.

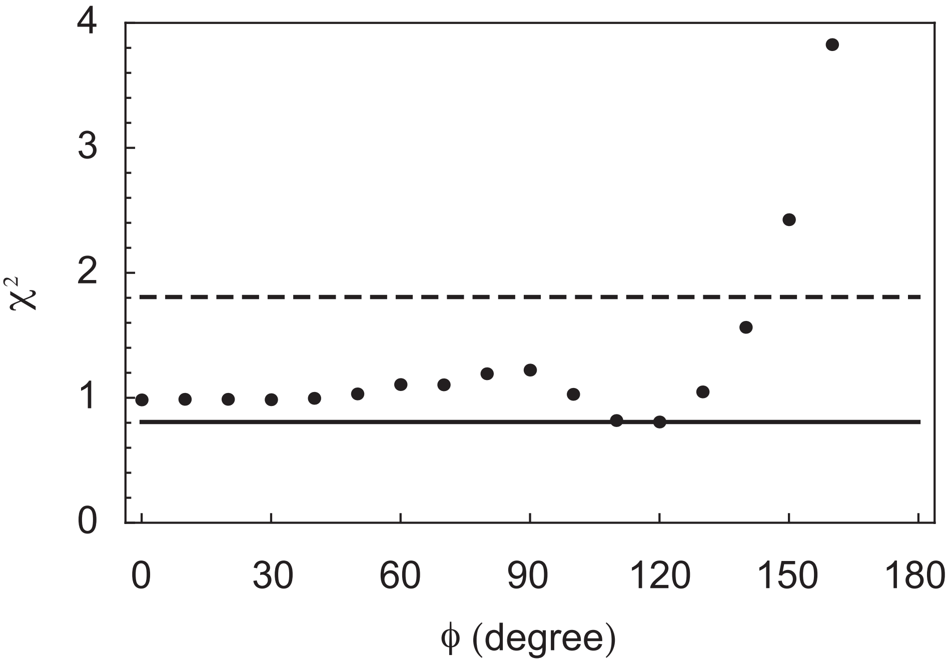

Fig. 5.20: χ^2 value plotted versus the torsional angle ϕ. The solid line indicate the minimum of χ^2 while the dotted line refers to the value given by $\chi^2 + 1$. The ϕ values whose χ^2 lies between the two horizontal lines are probable within the 68%. The data have been calculated using experimental and simulated signal intensities of bathorhodopsin-C11 peak.

This confirms that the retinal chromophore is in a *trans* configuration around the C11=C12 double bond in the isorhodopsin isomer.

5.3.3 Summary of Findings

The solid state NMR method called double-quantum heteronuclear local field spectroscopy (2Q-HLF) has been applied for the direct estimation of torsional angle in H-^{13}C-^{13}C-H molecular fragments of rhodopsin, bathorhodopsin and isorhodopsin. The reason of this study is to probe whether or not steric strain is a mechanism for energy storage in bathorhodopsin. The conclusions that can be drawn from our experiments of the H-C11=C12-H torsional angle can be so resumed:

- A deviation from the planarity of at least 40° about the C11=C12 double bond is consistent with NMR data for bathorhodopsin. These data, in agreement with previous Raman observations [57, 58], indicate that a not yet quantified percentage of steric strain is a probable mechanism in the photon energy storage, a leading aim of this thesis;

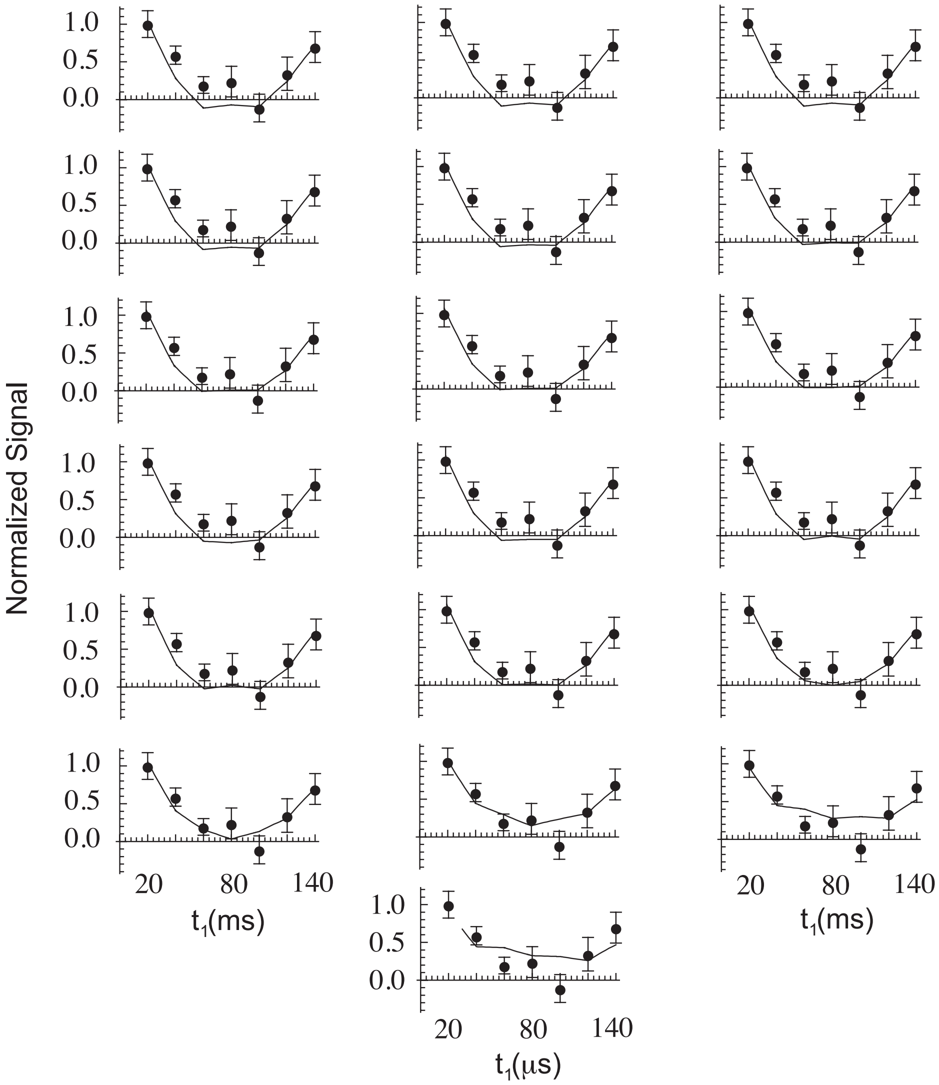

Fig. 5.21: Experimental normalized signal intensities (circles) and error bars as obtained for [11,12-$^{13}C_2$]-retinilydene-rhodopsin compared with SIMSON simulations (lines). The same experimental points are reported in each plot and compared to simulations at various values of the H-C11=C12-H torsional angle, ϕ. Plot refers to values of ϕ from 0° to 180° in steps of 10° from left to right and top to bottom.

- The same H-C11=C12-H torsional angle was estimated to be between 170° and 180° for the isorhodopsin isomer, confirming the planarity in this region or the retinylidene chain.

From a more methodological point of view:

- The pulse sequence here used is not suitable for probing samples that are in *cis* or near-*cis* configuration (like in the case of rhodopsin);

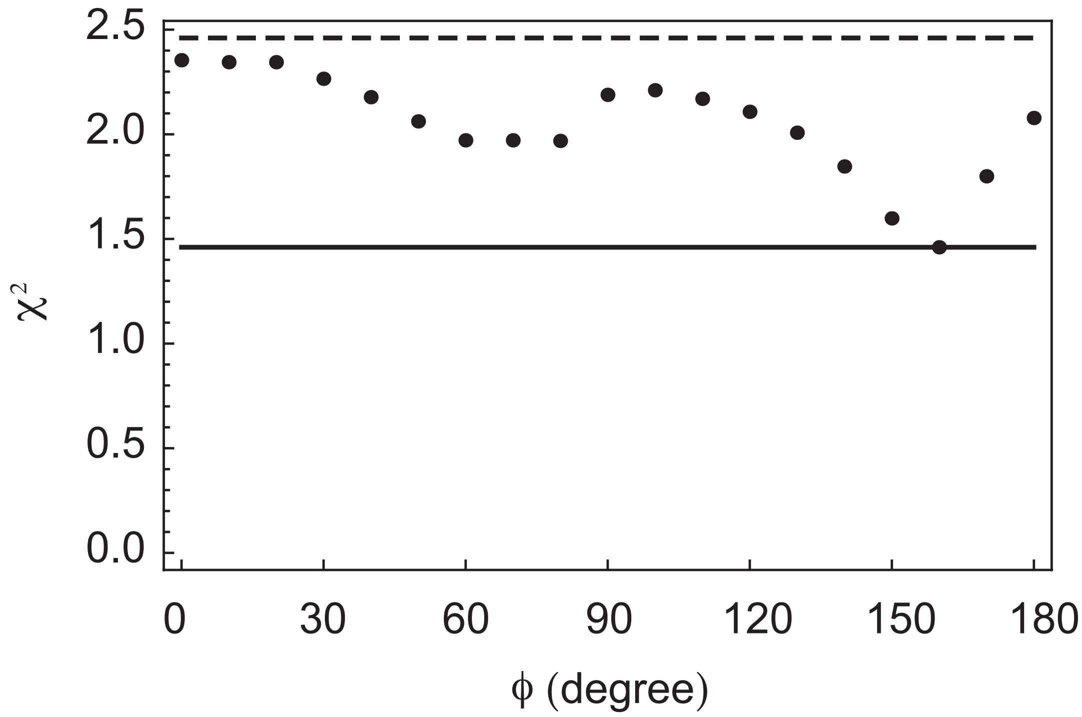

Fig. 5.22: χ^2 value plotted versus the torsional angle ϕ. The solid line indicate the minimum of χ^2 while the dotted line refers to the value given by χ^2+1. The ϕ values whose χ^2 lies between the two horizontal lines are probable within the 68%. The data have been calculated using experimental and simulated signal intensities of rhodopsin-C11 peak.

- In favorable cases, such as DAF , an accuracy of ±5° for near-*trans* conformations is easily achievable.

5.4 ^{13}C-^{13}C Distance Measurements

Distance measurements on a sample of [14,15-$^{13}C_2$]-retinylidene-rhodopsin and its bathorhodopsin isomer were also performed in order to check differences and to explore other local mechanisms that may contribute to the energy storage mechanism. Once again the credibility and accuracy of data was first assessed on a model compound. These data have been published in Paper 1.

5.4.1 Model Compound

A sample of [9-10,$^{13}C_2$]-all-E-retinal was used in order to set up the distance measurements. The technique used is a double quantum filtered dipolar recoupling experiment of Sec. 3.3, the same used for chemical shift measurements. In this case,

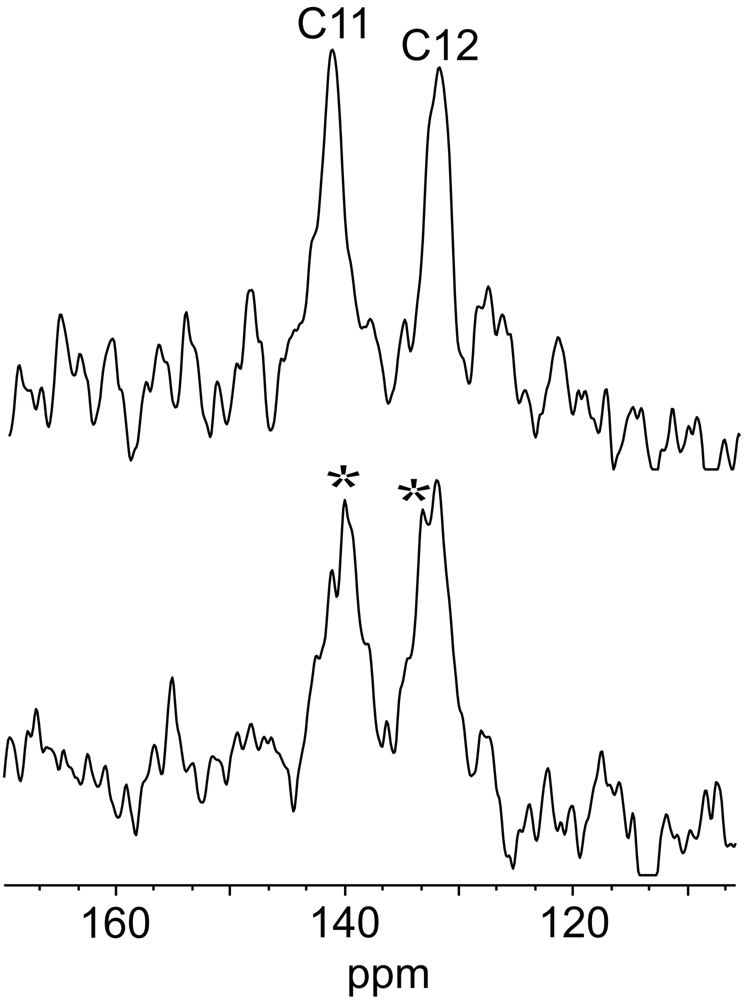

Fig. 5.23: Double quantum spectrum of [11,12-$^{13}C_2$]-retinilydene-isorhodopsin after illumination at 560 nm for 12 hours at 120 K confirming the presence of the isorhodopsin isomer (peaks indicated by asterisks)

however, the evolution time (τ_{exc}) and/or the reconversion time (τ_{rec}) were varied. The *build-up* curve (signal area versus τ_{exc} and/or τ_{rec}) is a function of the C-C distance between the two ^{13}C labeled carbons as explained in Sec. 3.3. The experiment was set up in the following way: the symmetry chosen for the recoupling period was $R20_2^9$ with the R element being $[90_{81}270_{261}]$. Magic angle spinning condition has been applied with a spinning speed ω_r = 10 kHz. All the experiments have been performed at room temperature on a 4 mm solid state probe in a magnetic field of 9.4 T using a Varian Infinity+ spectrometer. The nutation frequency $\omega_{nut}/2\pi$ for the decoupling scheme (SPINAL [108]) was set to 0 during the recoupling sequence and to 80 kHz during the signal acquisition (see Fig. 3.3). The nutation frequency

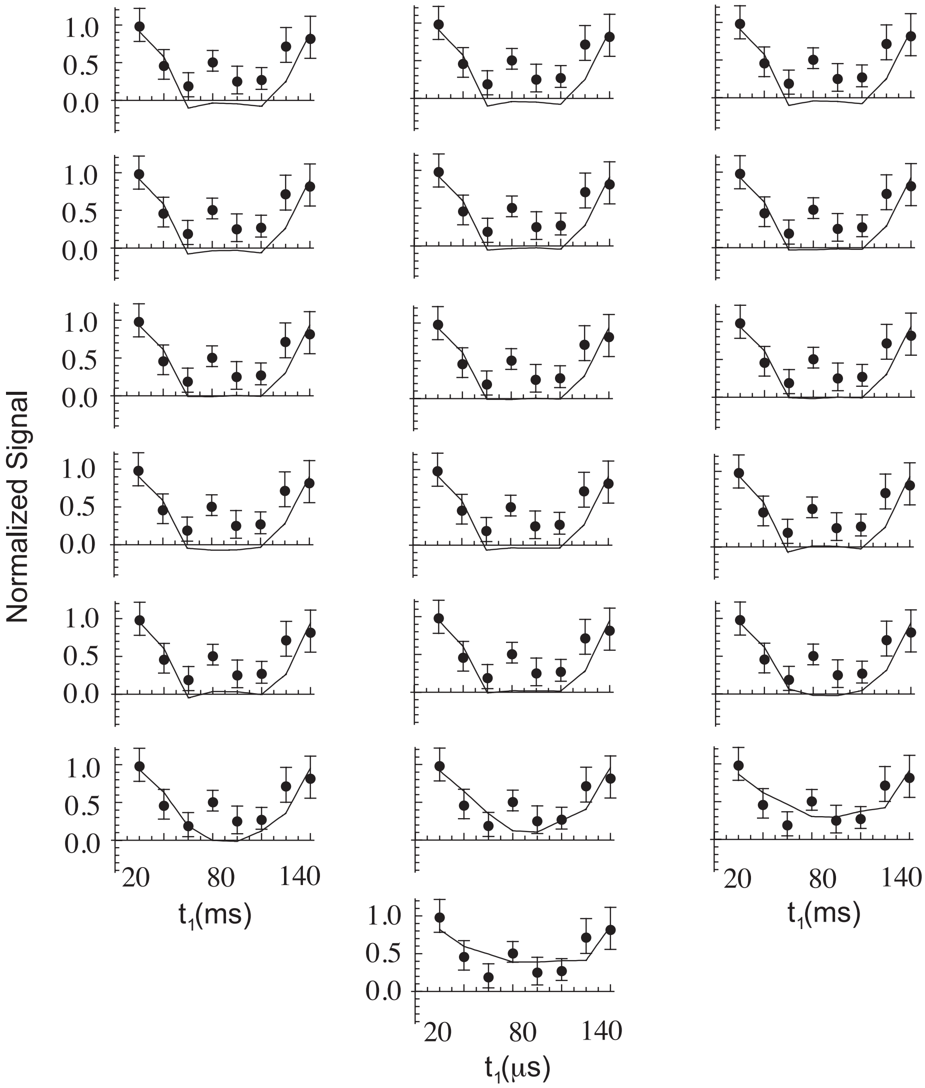

Fig. 5.24: Experimental normalized signal intensities (circles) and error bars as obtained for [11,12-$^{13}C_2$]-retinilydene-isorhodopsin compared with SIMSON simulations (lines). The same experimental points are reported in each plot and compared to simulations at various values of the H-C11=C12-H torsional angle, ϕ. Plot refers to values of ϕ from 0° to 180° in steps of 10° from left to right and top to bottom.

on the ^{13}C channel during the recoupling sequence was set to $\omega^{S}_{nut}/2\pi$ = (N/n)*ω_r = (20/2)*10 kHz = 100 kHz. This value explains the absence of decoupling during the recoupling scheme as found in [107]. The delay between transients was 5 s and 40 points were collected using both the symmetric and the asymmetric procedure in two separate experiments. In the latter case τ_{rec} was kept fixed at 400μs. The *build-up* curves obtained with the two procedure are reported in Fig. 5.26.

In order to estimate the C9-C10 distance, the collected data (i.e. signal intensi-

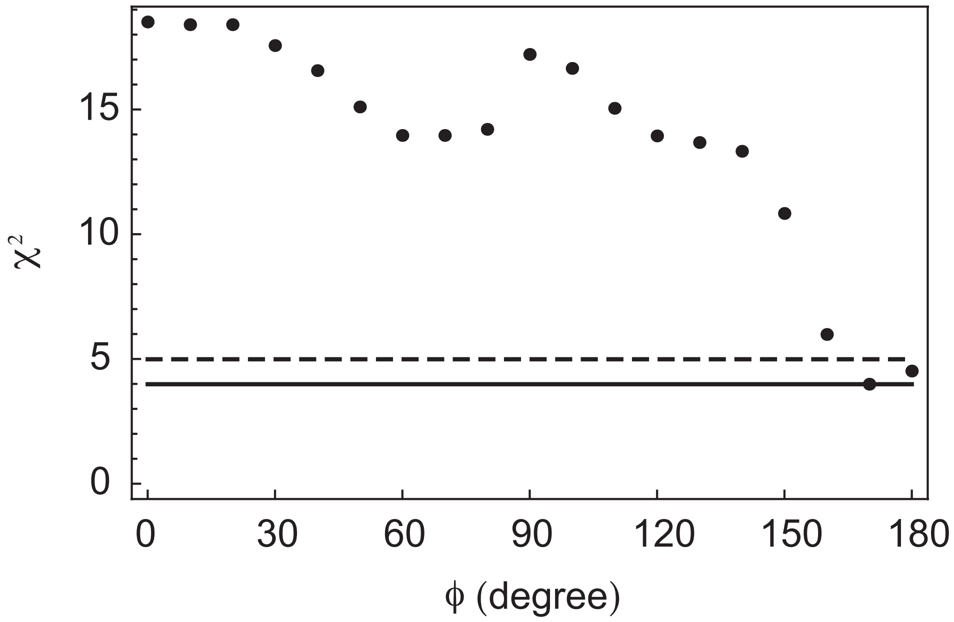

Fig. 5.25: χ^2 value plotted versus the torsional angle ϕ. The solid line indicate the minimum of χ^2 while the dotted line refers to the value given by χ^2+1. The ϕ values whose χ^2 lies between the two horizontal lines are probable within the 68%. The data have been calculated using experimental and simulated signal intensities of isodopsin-C11 peak.

ties versus $\tau_{exc}=\tau_{rec}=\tau$) were fitted to the following equation:

$$A\ s(\tau,\tau)\ exp\{-2\tau/T_{decay}\} \tag{5.10}$$

in the symmetric case and to:

$$A\ s(\tau_{exc},\tau_{rec})\ exp\{-(\tau_{exc}+\tau_{rec})/T_{decay}\} \tag{5.11}$$

in the asymmetric one. Explicit equations for $s(\tau,\tau)$ and $s(\tau_{exc},\tau_{rec})$ are given in Sec. 3.3. In both cases $|k_{2m22}|=0.174$ was used, as found in calculations (see Sec. 3.2). In the first case (the symmetric procedure) our data are compatible with a dipolar coupling $b_{jk}/2\pi=2.845$ kHz, $A=0.56$ and $T_{decay}=1.88$ ms while for the asymmetric procedure, data were fitted for $b_{jk}/2\pi=2.863$kHz, $A=0.65$ (in this latter case T_{decay} was kept fixed to the value found in the symmetric case, i.e. $T_{decay}=1.88$ms). Neglecting the J anisotropy and the averaging effect of molecular motions these dipolar couplings are compatible with a distance of 138 ± 1 pm. The X-ray crystallographic estimate for the same compound is 134.5 pm with a discrepancy of 3.5±1 pm which is typical when comparing the two techniques and

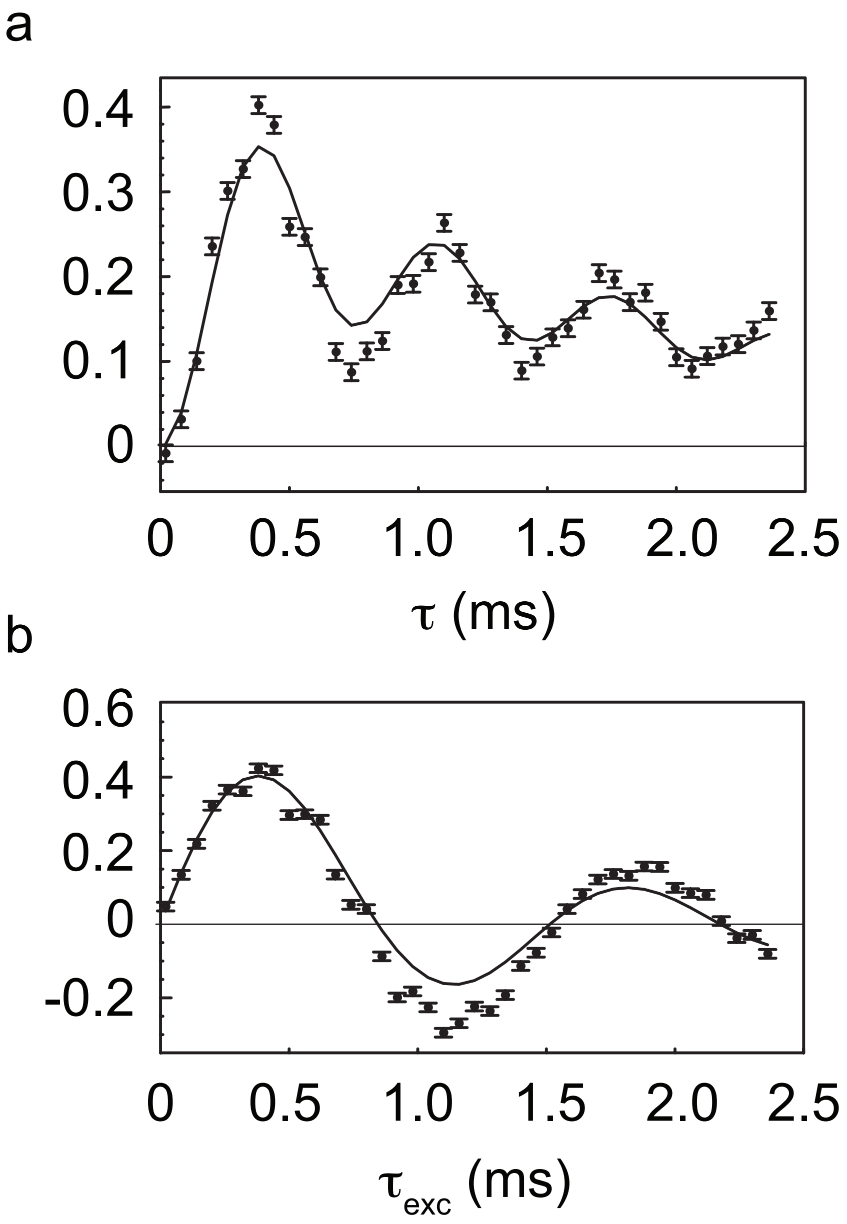

Fig. 5.26: Build-up curves for double quantum filtered dipolar recoupling experiments on [9-10,$^{13}C_2$]-all-E-retinal. Experimental points (filled circles) with experimental error margins acquired using: a) the symmetric procedure; and b) the asymmetric one. The black line is the best fit to experimental points (see text).

easily attributable to molecular motions.

5.4.2 Measurements on [14,15-$^{13}C_2$]-retinilydene-rhodopsin

The same procedure as above was used on a sample of [14,15-$^{13}C_2$]-retinilydene-rhodopsin. Before starting the illumination of the sample, a double quantum filtered spectrum of the sample was recorded at T = 120 K and spinning the sample with a frequency $\omega_r/2\pi$= 7 kHz (spectrum reported in Fig. 5.27a).

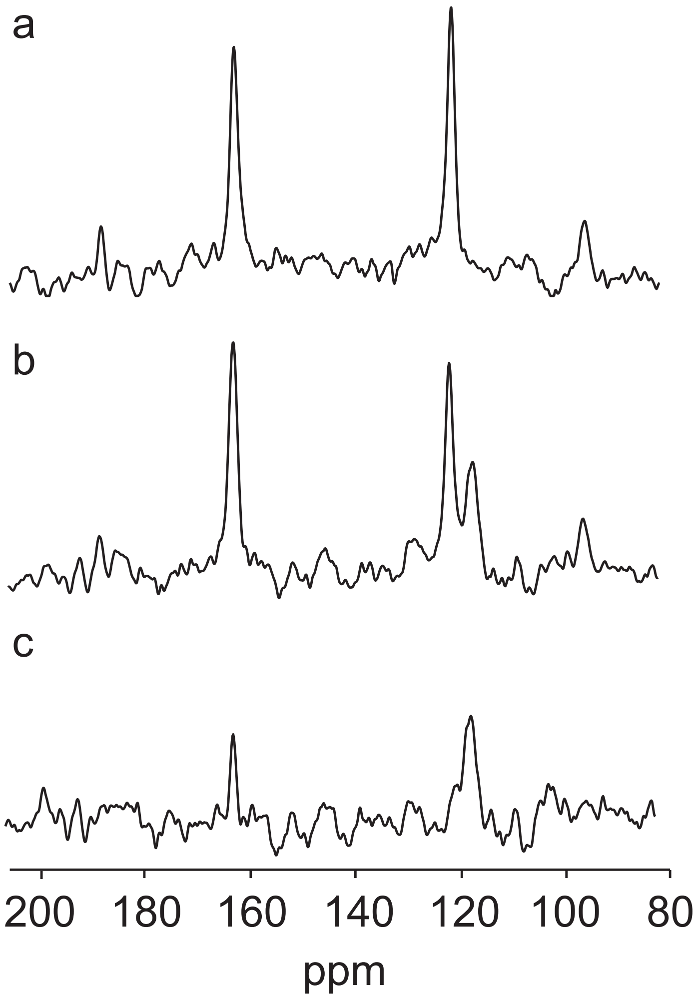

Fig. 5.27: All spectra refer to [14,15-$^{13}C_2$]-retinilydene-rhodopsin. a) Double quantum filtered spectrum before illumination (12 k scans); b) double quantum filtered spectrum after 10 hours of illumination (12 k scans); c) reconstructed bathorhodopsin spectrum obtained as by subtracting the spectrum in (b) to that in (a) but scaling the two spectra to have the same intensity for the C14-peak.

The chemical shift of the two peaks in the spectrum fully agree with the values obtained in previous studies [66]. After 10 hours of illumination a double quantum filtered spectrum has been recorded (Fig. 5.27b). A new peak can be observed on the left side of the C14 peak of rhodopsin. This peak at a chemical shift of 117.4 ppm can be easily attributed to bathorhodopsin's C14 because the rhodopsin's C14 peak decreases by the same amount. A difference between the spectrum obtained after the illumination and the spectrum of the sample before the illumination was done and it is shown in the same figure (Fig. 5.27c). This latter was reconstructed by scaling the spectrum obtained before the illumination of the sample in order to have the same intensity for the C14 peak of rhodopsin. In this reconstructed difference spectrum, it is possible to observe, quite clearly, also the C15 peak of bathorhodopsin that, falling under the width of rhodopsin's C15 peak, is not appreciable in the double quantum spectrum of Fig. 5.27a.

As before, in order to calculate internuclear distances between the two labeled carbons, the $R20_9^2$ recoupling sequence was used, the R element being $[90_{81}270_{261}]$. Magic angle spinning (MAS) condition has been applied with a spinning speed $\omega_r/2\pi$ = 7 kHz. Temperature set to 120 K in a 4 mm solid state probe at a magnetic field of 9.4 T on a Varian Infinity+ spectrometer. The nutation frequency $\omega_{nut}/2\pi$ for the decoupling scheme (SPINAL) was set to 0 during the recoupling sequence and to 80 kHz during the signal acquisition. The nutation frequency on the ^{13}C channel during the recoupling sequence was set to $\omega_{nut}^S/2\pi$ = (N/n)*ω_r = (20/2)*7 kHz = 70 kHz. The delay between transients was 5 s and 9 points were collected using the asymmetric procedure [83] where τ_{rec} was kept fixed at 26 τ_r and τ_{exc} was incremented in steps of 16 τ_r. The build-up curve obtained is reported in Fig. 5.28.

Due to the low quality of the spectra acquired (each point took 9 hour of acquisition at the temperature of 120K) a reconstruction technique, similar to that used for the torsional angle measurements (Sec. 5.3), is essential. Therefore, a simplified spectrum was built by adding four Lorentian peaks, centered, and with the same width of the four chemical shifts peaks of rhodopsin and bathorhodopsin as in the experimental spectrum of Fig. 5.27b. This spectrum was then multiplied to the experimental one to obtain a reconstructed spectrum that has the features of the experimentally recorded but no noise at all. The integration of this latter reconstructed spectrum (instead of the experimental one) gives rise to a cleaner build up curve (peak area versus recoupling time - τ_{exc} in this asymmetric case) whose points can be fitted to:

$$A\ s(\tau_{exc},\tau_{rec})\ exp\{-(\tau_{exc}+\tau_{rec})/T_{decay}\} \tag{5.12}$$

where $s(\tau_{exc},\tau_{rec})$ contains the dipolar coupling b_{jk} as parameter and where A, T_{decay} and b_{jk} were adjusted in the fitting procedure. The build-up curves obtained using this procedure for C14 and C15 are reported in Fig. 5.29 and Fig. 5.30

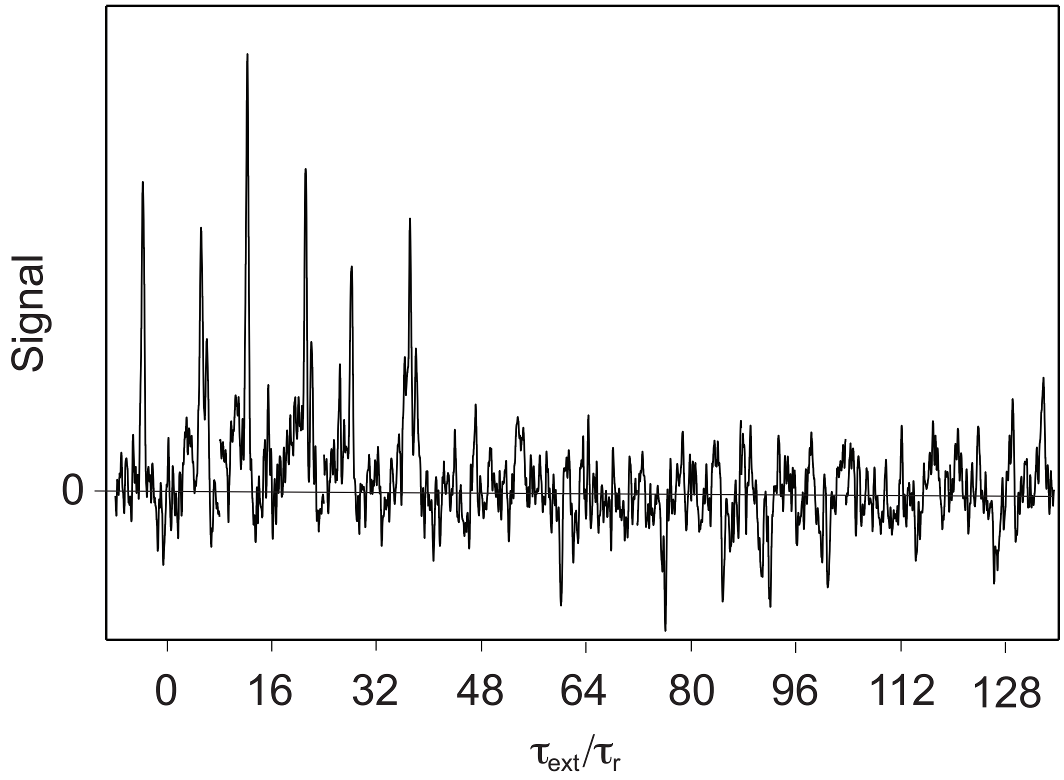

Fig. 5.28: Build-up curve for [14,15-$^{13}C_2$]-retinilydene-rhodopsin obtained acquiring 6 k scans for each value of τ_{exc} taken with τ_{rec} kept fixed at 26 τ_r and using $R20_9^2$ as the recoupling sequence with $[90_{81}270_{261}]$ as R basic element.

The dipolar couplings calculated, indicate a C14-C15 distance of 148 pm in the rhodopsin isomer and of 146 pm in the bathorhodopsin one. Within an expected error (not explicitly calculated) of about 5-10 pm it must be concluded that no net changes between rhodopsin and bathorhodopsin is measured for the two position C14 and C15.

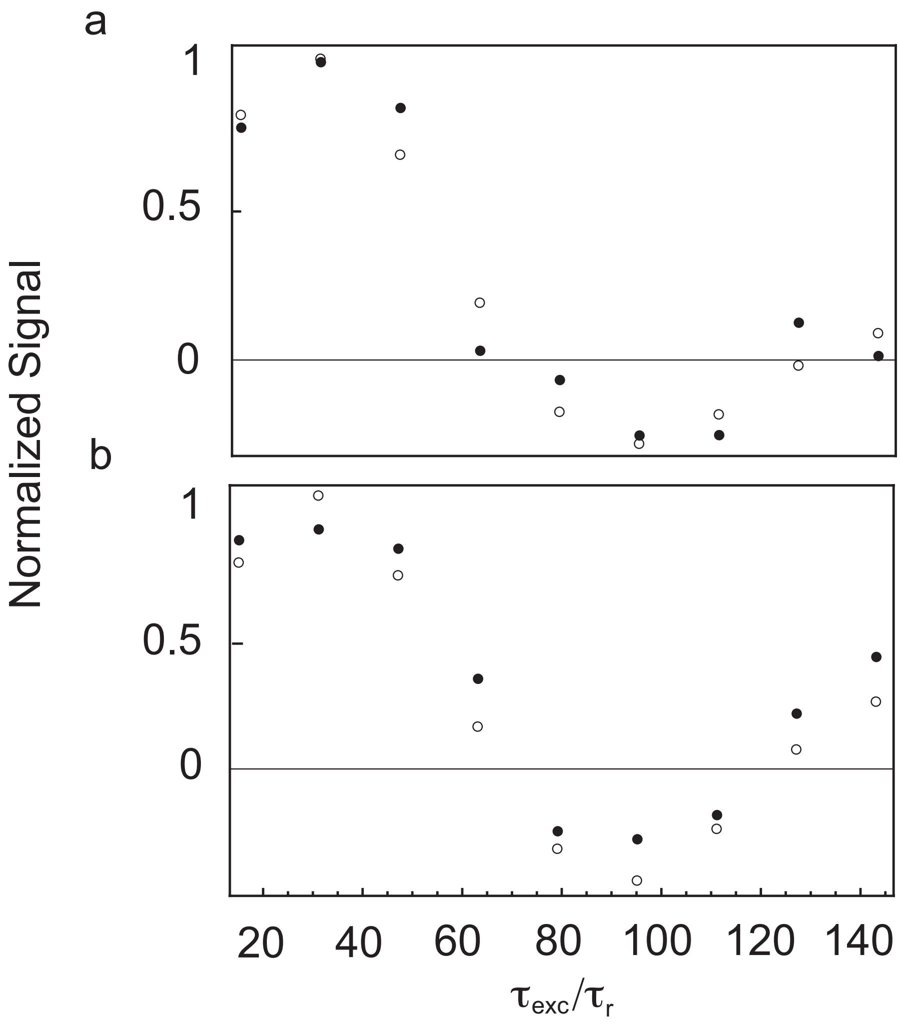

Fig. 5.29: Reconstructed build-up curves for C14 in: a) rhodospin; and b) bathorhodopsin. Filled and empty circles are experimental and best fit points, respectively.

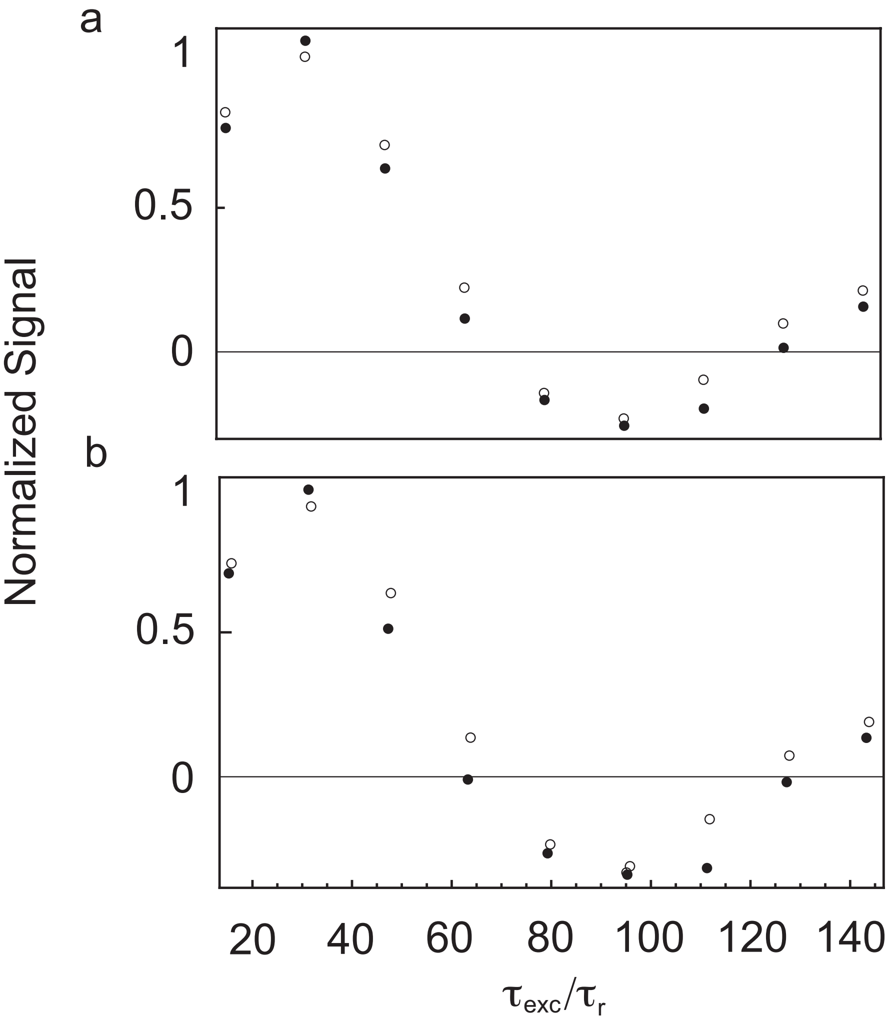

Fig. 5.30: Reconstructed build-up curves for C15 in: a) rhodospin; and b) bathorhodopsin. Filled and empty circles are experimental and best fit points, respectively.

CONCLUSION AND FINAL REMARKS

- *Review of aims*

  The subject of this Ph.D. thesis is the study of bathorhodopsin, the first photointermediate of rhodopsin protein photocycle by means of solid state NMR spectroscopy at low temperature. However, a more general aim lies in the setup of equipment, methods and procedures for the study of light-triggered photoreactions of which rhodopsin photocycle is one of the most interesting and challenging examples. This is due to the extreme working condition needed to trap its photointermediates. Moreover, despite a number of spectroscopic investigation have been carried out on this subject, the reasons why the isomerization process that starts the photointermediate cascade is one of the fastest, precise and efficient ever known and, especially, the way how the photon energy is stored in bathorhodopsin are still open questions. Therefore, the specific aim of this thesis can be narrowed to the collection of NMR data to be used in the further understanding of these mechanisms.

- *Outcomes*

  The main outcomes of this work are:

  1. a new and efficient experimental equipment for the in-situ preparation and detection of photointermediates;
  2. experimental parameters for optimal production of bathorhodopsin optimized by numerical finite-element simulations;
  3. the set of ^{13}C chemical shifts of almost all the carbons along the retinylidene chain of the rhodopsin chromophore (retinal);
  4. the application of NMR methodology for measuring torsional angle in photointermediates leading to the value of the torsional angle in the molecular fragment HCCH involved in the isomerization process of bathorhodopsin;

5. the application of NMR methodology for measuring carbon-carbon distances in photointermediates leading to the value of the carbon-carbon distance in the outermost carbons of the retinylidene chain of rhodopsin and bathorhodopsin (the one near to the link with the protein);
6. a tentative interpretation of the data acquired in terms of energy storage mechanisms acting in bathorhodopsin.

- *Review of findings*

  A customized NMR probe was setup and checked. It allows the in-situ cooling and illumination of the sample with the proper wavelength as indicated by numerical simulations and selected by appropriate optical filters. The sample temperature was calibrated using the ^{207}Pb chemical shift of lead nitrate and using the narrow proton resonance of the endohedral dihydrogen-fullerene complex $H_2@C_{60}$ as an independent chemical shift reference. The sample temperature was found to be different from the temperature of the cooling gas by more than 40 K. It is unlikely that in the previous NMR attempt, with a protocol that relied on the temperature of the cooling gas as a measure of the sample temperature, would have trapped bathorhodopsin reliably.
  The penetration of the light into the sample was studied by numerical finite-element simulations. They show, and experiments have proved, that illumination with white light leads to the generation of bathorhodopsin in the outer layer of the sample but generates a large amount of the side product isorhodopsin in the sample interior. The overall yield of bathorhodopsin is, instead, improved by using monochromatic 420 nm illumination and by mixing the sample with transparent glass beads that act as light pipes to penetrate the inner layers of the sample.
  ^{13}C chemical shifts acquired on bathorhodopsin were compared with the chemical shifts of the dark state chromophore in rhodopsin, as well as with the chemical shifts of retinylidene model compounds in solution. In a previous NMR study the differences in ^{13}C chemical shifts between rhodopsin and bathorhodopsin were quite limited (less than 2 ppm). Our findings show a very different picture: the chemical shifts of the odd-numbered ^{13}C sites are deshilded in bathorhodopsin with respect to rhodopsin, while for the even number chemical shifts, C12 and C14 experience a small upfield ligation shift and C10 experiences a big downfield ligation shift (about 8 ppm). Our chem-

ical shifts, notably, adhere to the linear relationship between the sum of the odd number chemical shifts and the frequency of maximum optical absorption, ν_{max} and are, therefore, in very good agreement with optical measurements.
From the measurements of torsional angle on bathorhodopsin a deviation from the planarity of at least 40° around the double bond in which the isomerization takes place, was found. A torsional angle of about 170° has been measured in isorhodopsin confirming the planarity of this region of the retinylidene chain. In the case of rhodopsin we do not have a clear result since the pulse sequence is not sensitive for probing molecules that are in a *cis* or near *cis* configuration. These data have not yet been published.
So far, ^{13}C-^{13}C distance measurements have been done on a sample of [14,15-$^{13}C_2$]-retinylidene-rhodopsin (data not published). No significant difference was found before and after the illumination of the sample. Although there is no simple and immediate conclusion out of this unvaried distance, the data collected have itself a certain importance in the sense that it is the first NMR distance measurement of a photointermediate. More distance measurements are needed in order to explore the changes in the vicinity of C11-C12.

- *Final remarks*

  From our data there are indications that the isomerization shifts of the odd-numbered carbons may be interpreted in terms of the small displacement of the positively charged counterion from the vicinity of the positively charged protonated Schiff base linkage, while the isomerization shifts of the even-numbered carbons are heavily influenced by the strong torsional twists in the region of the C11-C12 isomerization site. This twist was proved by measuring the torsional angle around the double bond. As a general conclusion we can state that both electrostatic and steric strain are involved in energy mechanism of bathorhodopsin. Finally, the success of these experiments and the optimized performance of the customized equipment here described with the possibility of a precise control of the sample temperature and an optimized illumination protocol, constitutes a great step in the solid-state NMR study of these light-triggered processes opening the way to further investigation of rhodopsin and other similar compounds.

BIBLIOGRAPHY

[1] T. Okada, M. Sugihara, A. N. Bondar, M. Elstner, P. Entel, and V. Buss, *J. Mol. Biol.*, **342**, 571–583 (2004).

[2] T. Okada, Y. Fujiyoshi, M. Silow, J. Navarro, E. M. Landau, and Y. Shikida, *Proc. Nat. Acad. Sci. USA*, **99**, 5982–5987 (2002).

[3] G. G. Matthews, *Neurobiology Molecules, cells and systems*, 2nd editions, Black-well Science, 2001.

[4] K. Palczewski, *Annu. Rev. Biochem.*, **75**, 743–767 (2006).

[5] R. W. Rodieck, *The first step in seeing*, Sinauer Associates Inc., Sunderland, Massachussetts, 1988.

[6] B. Borhan, M. L. Souto, H. Imai, Y. Shikida, and K. Nakanishi, *Science*, **288**, 2209–2212 (2000).

[7] R. R. Birge, C. M. Einters, H. M. Knapp, and L. P. Murray, *Biophys. J.*, **53**, 367–385 (1988).

[8] M. H. Levitt In *Encyclopedia of Nuclear Magnetic Resonance: Supplementary Volume*, D. M. Grant and R. K. Harris, Eds.; Wiley, Chichester, 2002; pages 165–196.

[9] M. Hohwy, H. J. Jakobsen, M. Edén, M. H. Levitt, and N. C. Nielsen, *J. Chem. Phys.*, **108**, 2686 (1998).

[10] A.Creemers, S. Kiihne, P.Bovee-Geurts, W. J. de Grip, J. Lugtenburg, and H. J. M. de Groot, *Proc. Nat. Acad. Sci.*, **99**, 9101–9106 (2002).

[11] S. O. Smith, I. Palings, M. E. Miley, J. Courtin, H. J. M. de Groot, J. Lugtenburg, R. A. Mathies, and R. G. Griffin, *Biochemistry*, **29**, 8158–8164 (1990).

[12] S. O. Smith, J. Courtin, H. J. M. de Groot, R. Gebhard, and J. Lugtenburg, *Biochemistry*, **30**, 7409–7415 (1991).

[13] U. F. Röhrig and D. J. Sebastiani, *Phys. Chem. B*, **112**, 1267–1274 (2008).

[14] J. A. Gascón, E. M. Sproviero, and V. S. Batista, *J. Chem. Theory Comput.*, **1**, 674–685 (2005).

[15] J. A. Gascón, E. M. Sproviero, and V. S. Batista, *Acc. Chem. Res.*, **39**, 184–193 (2006).

[16] J. W. Shriver, G. D. Mateescu, and E. W. Abrahamson, *Biochemistry*, **18**, 4785–4792 (1979).

[17] G. R. Elia, R. F. Childs, J. F. Britten, D. S. C. Yang, and B. D. Santarsiero, *Canadian Journal of Chemistry-Revue Canadienne De Chimie*, **74**, 591–601 (1996).

[18] M. Han, B. S. DeDecker, and S. O. Smith, *Biophys. J.*, **65**, 899–906 (1993).

[19] H. Nakamichi and T. Okada, *Photochemistry and Photobiology*, **83**, 231–235 (2007).

[20] Y. Shikida and H. Imai, *Cell. Mol. Life Sci.*, **54**, 1299–1315 (1998).

[21] S. T. Menon, M. Han, and T. P. Sakmar, *Physiol. Rev.*, **81**, 1659–1688 (2001).

[22] T. Okada, O. P. Ernst, K. Palczewski, and K. P. Hofmann, *Trends Biochem. Sci.*, **26**, 318–324 (2001).

[23] K. G. Palczewski, T. Kumasaka, T. Hori, C. A. Behnke, and H. Motoshima, *Science*, **289**, 739–745 (2000).

[24] J. Ballesteros and K. Palczewski, *Curr. Opin. Drug Discov. Dev.*, **4**, 561–574 (2001).

[25] T. Mirzadegan, G. Benko, S. Filipek, and K. Palczewski, *Biochemistry*, **42**, 2759–2767 (2003).

[26] G. F. X. Schertler, C. Villa, and R. Henderson, *Nature*, **362**, 770–772 (1993).

[27] V. M. Unger, P. A. Hargrave, J. M. Baldwin, and G. F. X. Schertler, *Nature*, **389**, 203–206 (1997).

[28] J. M. Baldwin, G. F. X. Schertler, and V. M. Unger, *J. Mol. Biol.*, **272**, 144–164 (1997).

[29] P. R. Robinson, G. B. Cohen, E. A. Zhukovsky, and D. D. Oprian, *Neuron*, **9**, 719–725 (1992).

[30] D. L. Farren, C. Altenback, K. Yang, W. L. Hubbell, and H. G. Khorana, *Science*, **274**, 768–770 (1996).

[31] C. D. Strader, I. S. Sigal, M. R. Candelore, E. Rands, W. S. Hill, and R. A. Dixon, *J. Biol. Chem.*, **263**, 10267–10271 (1988).

[32] B. Honig, U. Dinur, K. Nakanishi, V. Balogh-Nair, M. A. Gawinowics, N. Arnaboldi, and M. G. Motto, *J. Am. Chem. Soc.*, **101**, 7084–7086 (1979).

[33] T. G. Ebrey, *Methods in Enzym.*, **315**, 196–207 (2000).

[34] M. A. Verhoeven, A. F. L. Creemers, P. H. M. Bovee-Geurts, W. J. de Grip, J. Lugtenburg, and H. J. M. de Groot, *Biochemistry*, **40**, 3282–3288 (2001).

[35] M. Eilers, P. J. Reeves, W. Ying, H. G. Khorana, and S. O. Smith, *Proc. Nat. Acad. Sci. USA*, **96**, 487–492 (1999).

[36] D. C. Teller, T. Okada, C. A. Behnke, K. G. Palczewski, and R. E. Stenkamp, *Biochemistry.*, **40**, 7761–72 (2001).

[37] J. H. Lou, Q. Tan, E. Karnaukhova, N. Berova, K. Nakanishi, and R. K. Crouch, *Methods in Enzym.*, **315**, 229–237 (2000).

[38] G. G. Kochendoerfer, P. J. E. Verdegem, I. V. der Hoef, J. Lugtenburg, and R. A. Mathies, *Biochemistry*, **35**, 16230–16240 (1996).

[39] V. Buss, M. Sugihara, P. Entel, and J. Hafner, *Angew. Chem. Int. Ed.*, **42**, 3245–3247 (2003).

[40] M. Sugihara, V. Buss, P. Entel, and J. Hafner, *J. Phys. Chem. B*, **108**, 3673–3680 (2004).

[41] V. R. Rao and D. D. Oprian, *Annu. Rev. Biophys. Biomol. Struct.*, **25**, 287–314 (1996).

[42] J. H. Hurley, T. G. Ebrey, B. Honig, and M. Ottolenghi, *Nature*, **270**, 540–542 (1977).

[43] L. A. Peteanu, R. W. Schoenlein, Q. Wang, R. A. Mathies, and C. V. Shank, *Proc. Nat. Acad. Sci. USA*, **90**, 11762–11766 (1993).

[44] F. Jager, K. Fahmy, T. P. Sakmar, and F. Sieberg, *Biochemistry*, **33**, 10878–10882 (1994).

[45] C. Altenback, J. Klein-Seetharaman, K. W. Cai, H. G. Khorana, and W. L. Hubbell, *Biochemistry*, **40**, 15493–15500 (2001).

[46] A. Cooper, *Nature*, **282**, 531–533 (1979).

[47] T. Yoshizawa, Y. Kito, and M. Ishigami, *Biochim. Biophys. Acta*, **43**, 329–334 (1960).

[48] R. W. Schoenlein, L. A. Peteanu, R. A. Mathies, and C. V. Shank, *Science*, **254**, 412 (1991).

[49] T. Yoshizawa and G. Wald, *Nature*, **4874**, 1279–1286 (1963).

[50] P. Yoshizawa, Y. Shikida, and S. Matuoka, *Vis. Res.*, **24**, 1455–1463 (1984).

[51] X. Feng, P. J. E. Verdegem, M. Edén, D. Sandstrom, Y. K. Lee, P. H. M. Bovee-Geurts, W. J. de Grip, J. Lugtenburg, H. J. M. de Groot, and M. H. Levitt, *J. Biomol. NMR*, **16**, 1–8 (2000).

[52] P. J. E. Verdegem, P. H. M. Bovee-Geurts, W. J. de Grip, J. Lugtenburg, and H. J. M. de Groot, *Biochemistry*, **38**, 11316–11324 (1999).

[53] H. Nakamichi and T. Okada, *Angew. Chem. Int. Ed.*, **45**, 4270–4273 (2006).

[54] I. Palings, J. A. Pardoen, E. V. der berg, C. Winkel, J. Lugtenburg, and R. A. Mathies, *Biochemistry*, **26**, 2544–2556 (1987).

[55] S. W. Lin, M. Groesbeek, I. V. der Hoef, P. J. E. Verdegem, J. Lugtenburg, and R. A. Mathies, *J. Phys. Chem B*, **35**, 2787–2806 (1998).

[56] M. Garavelli, F. Negri, and M. Olivucci, *J. Am. Chem. Soc.*, **121**, 1023–1029 (1999).

[57] P. Kukura, D. W. McCamant, S. Yoon, D. B. Wandschneider, and R. A. Mathies, *Science*, **310**, 1006–1009 (2005).

[58] E. C. Y. Yan, Z. Ganim, M. A. Kazmi, B. S. W. Chang, T. P. Sakmar, and R. A. Mathies, *Biochemistry*, **43**, 10867–10876 (2004).

[59] J. E. Kim, D. W. McCamant, L. Zhu, and R. A. Mathies, *J. Phys. Chem B*, **105**, 1240–1249 (2001).

[60] S. O. Smith, I. Palings, V. Copie, D. P. Raleigh, J. Courtin, J. A. Pardoen, J. Lugtenburg, R. A. Mathies, and R. G. Griffin, *Biochemistry*, **26**, 1606 (1987).

[61] S. O. Smith, J. Courtin, H. D. Groot, R. Gebhard, and J. Lugtenburg, *biochemistry*, **30**, 7409–7415 (1991).

[62] M. Han and S. O. Smith, *Biochemistry*, **34**, 1425–1432 (1995).

[63] X. Feng, P. J. E. Verdegem, Y. K. Lee, D. Sandstrom, M. Edén, P. H. M. Bovee-Geurts, W. J. de Grip, J. Lugtenburg, H. J. M. de Groot, and M. H. Levitt, *J. Am. Chem. Soc.*, **119**, 6853–6857 (1997).

[64] A. F. L. Creemers, C. H. W. Klaassen, P. H. M. Bovee-Geurts, R. Kelle, U. Kragl, J. Raap, W. J. de Grip, J. Lugtenburg, and H. J. M. de Groot, *Biochemistry*, **38**, 7195–7199 (1999).

[65] G. Gröbner, I. J. Burnett, C. Glaubitz, G. Choi, A. J. Mason, and A. Watts, *Nature*, **405**, 810–813 (2000).

[66] A. F. L. Creemers, S. Kiihne, P. H. M. Bovee-Geurts, W. J. de Grip, J. Lugtenburg, and H. J. M. de Groot, *Proc. Nat. Acad. Sci.*, **99**, 9101 (2002).

[67] F. Buda, H. J. M. de Groot, and A. Bifone, *Phys. Rev. Lett.*, **77**, 4474 (1996).

[68] M. Sugihara, P. Entel, H. Meyer, V. Buss, and J. Hafner, *Prog. Theor. Phys.*, **138**, 107 (2000).

[69] F. Buda, P. Giannozzi, and F. Mauri, *J. Phys. Chem B*, **104**, 9048–9053 (2000).

[70] M. Schreiber and V. Buss, *Int. J. Quant. Chem.*, **95**, 882–889 (2003).

[71] M. Schreiber, M. Sugihara, T. Okada, and V. Buss, *Angew. Chem. Int. Ed.*, **45**, 4274–4277 (2006).

[72] U. F. Rohrig, L. Guidoni, A. Laio, I. Frank, and U. Rothlisberger, *J. Am. Chem. Soc.*, **126**, 15328–15329 (2004).

[73] E. C. Y. Yan, M. A. Kazmi, Z. Ganim, J. M. Hou, D. H. Pan, B. S. W. Chang, T. P. Sakmar, and R. A. Mathies, *Proc. Nat. Acad. Sci. USA*, **100**, 9262–9267 (2003).

[74] S. Ludeke, R. Beck, E. C. Y. Yan, T. P. Sakmar, F. Sieberg, and R. Vogel, *J. Mol. Biol.*, **353**, 345–356 (2005).

[75] S. I. E. Touw, H. J. M. de Groot, and F. Buda, *J. Phys. Chem. B*, **108**, 13560–13572 (2004).

[76] K. Kholmurodov, T. Fel'dman, and M. Ostrovsky, *Russian Chemical Bulletin*, **56**, 20–27 (2007).

[77] J. Gascon and V. Batista, *Biophysical Journal*, **87**, 2931–2941 (2004).

[78] A. Bifone, H. deGroot, and F. Buda, *Journal of Physical Chemistry B*, **101**, 2954–2958 (1997).

[79] S. Nishimura, H. Kandori, M. Nakagawa, M. Tsuda, and A. Maeda, *Biochemistry*, **36**, 864–870 (1997).

[80] S. Nishimura, H. Kandori, and A. Maeda, *Photochemistry and Photobiology*, **66**, 796–801 (1997).

[81] H. Kandori and A. Maeda, *Biochemistry*, **34**, 14220–14229 (1995).

[82] U. Ganter, E. Schmid, and F. Siebert, *J. Photochem. Photobiol. B*, **2**, 417–426 (1988).

[83] M. Carravetta, M. Edén, O. G. Johannessen, H. Luthman, P. J. E. Verdegem, J. Lugtenburg, A. Sebald, and M. H. Levitt, *J. Am. Chem. Soc.*, **123**, 10628 (2001).

[84] M. Mehring, *Principles of High Resolutions NMR in solids*, Springer, Verlin, 1983.

[85] M. E. Rose, *Elementary Theory of Angular Momentum*, John Wiley and Sons, 1957.

[86] D. Varshalovich, A. Moskalev, and V. Khersonskii, *Quantum Theory of Angular Momentum*, World Scientific, 1988.

[87] A. Brinkmann and M. H. Levitt, *J. Chem. Phys.*, **115**, 357–384 (2001).

[88] U. Haeberlen and J. S. Waugh, *Phys. Rev.*, **175**, 453 (1968).

[89] W. Magnus, *Commun. Pure Appl. Math.*, **7**, 649 (1954).

[90] M. Edén and M. H. Levitt, *J. Chem. Phys.*, **111**, 1511–1519 (1999).

[91] M. H. Levitt. Mathematica routines for spin dynamics. Available at: http://www.mhl.soton.ac.uk.

[92] G. Pileio, M. Concistre', N. McLean, A. Gansmuller, R. C. D. Brown, and M. H. Levitt, *J. Magn. Phys.*, **186**, 65–74 (2007).

[93] A. Brinkmann *Dipolar Recoupling in Magic-Angle-Spinning Nuclear Magnetic Resonance* PhD thesis, Stockholm University, (2001).

[94] X. Feng, J. K. Lee, D. Sandstrom, M. Edén, H. Maisel, A. Sebald, and M. H. Levitt, *Chem.Phys.Lett.*, **257**, 314–320 (1996).

[95] E. Vinogradov, P. K. Madhu, and S. Vega, *Chem.Phys.Lett.*, **314**, 443–450 (1999).

[96] E. Vinogradov, P. K. Madhu, and S. Vega, *Chem.Phys.Lett.*, **354**, 193–202 (2002).

[97] A. Bielecki, A. C., H. J. M. de Groot, R. G. Griffin, and M. H. Levitt, *Adv. Magn. Res.*, **14**, 111–124 (1990).

[98] X. Feng *Estimating Molecular Conformations by Solid-State NMR Spectroscopy* PhD thesis, Stockholm University, Sweden, (1998).

[99] G. Neue and C. Dybowski, *Solid State Nucl. Magn. Reson.*, **3**, 333–336 (1997).

[100] M. Carravetta, A. Danquigny, S. Mamone, F. Cuda, O. G. Johannessen, I. Heinmaa, K. Panesar, R. Stern, M. C. Grossel, A. J. Horsewill, A. Samoson, M. Murata, Y. Murata, K. Komatsu, and M. H. Levitt, *Phys. Chem. Phys.*, **9**, 4879–4894 (2007).

[101] M. Groesbeek and J. Lugtenburg, *J. Photochem. Photobiol.*, **56**, 903–908 (1996).

[102] W. C. Lai, N. McLean, A. Gansmuller, M. A. Verhoeven, G. C. Antonioli, M. Carravetta, L. Duma, P. H. M. Bovee-Geurts, O. G. Johannessen, H. J. M. de Groot, J. Lugtenburg, L. Emsley, S. P. Brown, R. C. D. Brown, W. J. de Grip, and M. H. Levitt, *J. Am. Chem. Soc.*, **128**, 3878–3879 (2006).

[103] W. J. de Grip, F. J. M. Daemen, and S. L. Bonting, *Methods in Enzymol.*, **67**, 301–320 (1980).

[104] A. Bielecki and D. P. Burum, *J. Magn. Reson. A*, **116**, 215 (1995).

[105] R. K. Harris and E. D. Becker, *J. Magn. Reson.*, **156**, 323–326 (2002).

[106] A. Gansmuller, M. Concistre', N. McLean, O. G. Johannessen, I. Marin-Montesinos, P. H. M. Bovee-Geurts, P. J. E. Verdegem, J. Lugtenburg, R. C. D. Brown, W. J. de Grip, and M. H. Levitt, *Biochim. Biophys. Acta*, **1788**, 1350–1357 (2009).

[107] I. Marin-Montesinos, D. Brouwer, G. C. Antonioli, W. C. Lai, and M. H. Levitt, *J. Magn. Reson.*, **177**, 307–317 (2005).

[108] B. M. Fung, A. K. Khitrin, and K. Ermolaev, *J. Magn. Reson.*, **142**, 97–101 (2000).

[109] A. F. L. Creemers, P. H. M. Bovee-Geurts, W. J. de Grip, J. Lugtenburg, and J. M. de Groot, *Biochemistry*, **43**, 16011–16018 (2004).

[110] M. Carravetta, X. Zhao, O. G. Johannessen, W. C. Lai, M. A. Verhoeven, P. H. M. Bovee-Geurts, P. J. E. Verdegem, S. Kiihne, H. Luthman, H. J. M. de Groot, W. J. de Grip, J. Lugtenburg, and M. H. Levitt, *J. Am. Chem. Soc.*, **126**, 3948–3953 (2004).

[111] M. A. Verhoeven, A. F. L. Creemers, P. H. M. Bovee-Geurts, W. J. de Grip, J. Lugtenburg, and H. J. M. de Groot, *Biochemistry*, **40**, 3282–3288 (2001).

[112] F. Buda, H. J. M. de Groot, and A. Bifone, *Phys. Rev. Lett.*, **77**, 4474–4477 (1996).

[113] D. S. Boudreaux, R. R. Change, J. L. Bredas, and R. Silbey, *Phys. Rev. B*, **28**, 6927–6936 (1983).

[114] L. Mollevanger, A. P. M. Kentgens, J. A. Pardoen, J. M. L. Courtin, W. S. Veeman, J. Lugtenburg, and W. J. de Grip, *Eur. J. Biochem.*, **163**, 9–14 (1987).

[115] K. F. Hall, T. Vreven, M. J. Frisch, and M. J. Bearpark, *J. Mol. Biol.*, **383**, 106–121 (2008).

[116] A. F. L. Creemers, C. H. W. Klaassen, P. H. M. Bovee-Geurts, R. Kelle, U. Kragl, J. Raap, W. J. de Grip, J. Lugtenburg, and H. J. M. de Groot, *Biochemistry*, **38**, 7195–7199 (1999).

[117] J. Hu, R. G. Griffin, and J. Herzfeld, *Biochemistry*, **91**, 8880–8884 (1994).

[118] P. E. Blatz, J. H. Mohler, and H. V. Navangul, *Biochemistry*, **11**, 848–855 (1972).

[119] M. Bak, J. T. Rasmussen, and N. C. Nielsen, *J. Magn. Reson.*, **147**, 296–330 (2000).

[120] M. Carravetta *Symmetry-Based Double Quantum Recoupling in Solid State NMR* PhD thesis, Stockholm University, (2002).